

**STRUCTURAL CONTROLS ON MINERALIZATION AND
CONSTRAINTS ON FLUID EVOLUTION AT THE
SACRIFICIO Cu (Zn-Pb-Ag-Au) SKARN,
DURANGO, MEXICO**

By

KEITH MARK PATTERSON

B.A.Sc., The University of British Columbia, 1994

A THESIS SUBMITTED IN PARTIAL FULFILMENT OF
THE REQUIREMENTS FOR THE DEGREE OF

MASTER OF SCIENCE

In

THE FACULTY OF GRADUATE STUDIES

(Department of Earth and Ocean Sciences)

We accept this thesis as conforming
to the required standard

THE UNIVERSITY OF BRITISH COLUMBIA

May 2001

© Keith Mark Patterson, 2001

In presenting this thesis in partial fulfilment of the requirements for an advanced degree at the University of British Columbia, I agree that the Library shall make it freely available for reference and study. I further agree that permission for extensive copying of this thesis for scholarly purposes may be granted by the head of my department or by his or her representatives. It is understood that copying or publication of this thesis for financial gain shall not be allowed without my written permission.

Department of EARTH AND OCEAN SCIENCES

The University of British Columbia
Vancouver, Canada

Date MAY 17, 2001

Abstract

The Sacrificio deposit, located in Durango State, Mexico, is hosted by mid-Cretaceous limestone, chert, and minor shale of the Cuesta del Cura and Indidura formations. Intrusive rocks include two temporally and compositionally distinct suites, dated at 109.1 ± 0.4 Ma (mid-Cretaceous) and 40.1 ± 0.5 Ma (Middle Eocene) by U-Pb methods. The Middle Eocene granite suite is associated with the development of skarn and related sulphide mineralization that forms the Sacrificio deposit. Three episodes of pre-intrusion regional deformation (D_1 to D_3) and two episodes of syn-intrusion local deformation are recognized at the Sacrificio deposit. Skarn and skarn-related mineralization is localized by these regional and local structures and their intersections.

Alteration at the Sacrificio deposit is divided into pre-mineralization contact metamorphism, prograde skarn, and retrograde skarn. Styles of skarn-related sulphide mineralization include: (1) disseminated bornite and lesser chalcopyrite filling porosity in prograde garnet skarn; (2) fracture-controlled, silver-rich, bornite-chalcopyrite \pm sphalerite \pm galena \pm arsenopyrite cutting prograde garnet skarn and marble; and (3) semi-massive to massive sulphide bodies (mantos) containing sphalerite, galena, chalcopyrite, arsenopyrite, pyrrhotite, pyrite, and bornite associated with retrograde amphibole skarn. Rare quartz-arsenopyrite veins cut all alteration and mineralization.

Skarn and sulphide-forming fluids at the Sacrificio deposit are interpreted to be magmatic in origin from lead isotope data. Compositions of garnet ($Ad_{65-100}Gr_{0-35}$) and pyroxene ($Di_{68-94}Hd_{5-30}Jo_{1-3}$) from prograde skarn classify the

Sacrificio deposit as a copper skarn. Fluid inclusion studies indicate that mineralizing fluids were dominantly H₂O-NaCl mixtures (0.5 – 19.7 wt. % NaCl eq.) containing divalent cations (i.e., Mg²⁺, Fe²⁺, and Ca²⁺). Pressures during the development of the Sacrificio deposit were approximately 0.5 to 1.0 kbar. Temperatures recorded during skarn formation and sulphide deposition show a gradual cooling of the skarn system. Prograde skarn formed at 460° to 580° C, disseminated Cu-Ag mineralization at 291° to 504° C, and mantos at 247° to 396° C. A final pulse of hotter fluids (318° to 480° C) formed the late quartz-arsenopyrite veins.

Results of this study have allowed the construction of a detailed structural and fluid evolution model for the Sacrificio deposit. Application of these findings to other skarn deposits or prospects in Mexico, and elsewhere in the world, may lead to the discovery of important new orebodies.

Table of Contents

Abstract	ii
Table of Contents	iv
List of Tables	viii
List of Figures	ix
Acknowledgments	xi

Chapter 1

General Introduction	1
Methodology	2
<i>Geological Field Mapping</i>	2
<i>Structural Analysis</i>	2
<i>U-Pb Geochronological Studies</i>	2
<i>Lithogeochemical Studies</i>	3
<i>Fluid Inclusion Studies</i>	3
<i>Pb Isotope Studies</i>	3
<i>Garnet and Pyroxene Electron Microprobe Studies</i>	4
Presentation	4
References	5

Chapter 2

The Importance of Pre- and Syn-Intrusion Deformation	
in Controlling the Distribution of Cu (Zn-Pb-Ag-Au) Skarn	
Mineralization at Cerro el Sacrificio, Durango, Mexico	6
Abstract	7

Table of Contents (cont.)

Introduction	8
Property History	11
Methods Employed	12
Regional Geology	13
<i>Geographical Setting</i>	13
<i>Altiplano Stratigraphy</i>	14
<i>Intrusive Rocks</i>	14
<i>Tectonic Setting</i>	15
Property Geology	16
<i>Stratigraphy</i>	16
<i>Intrusive Rocks</i>	17
<i>U-Pb Geochronology</i>	19
<i>Structure</i>	22
Mineralization	23
<i>Disseminated Cu-Ag mineralization</i>	24
<i>Fracture controlled Cu-Ag±Au mineralization</i>	25
<i>Manto-style Zn-Cu-Pb-Ag-Au mineralization</i>	26
Alteration	27
Structural Evolution of the Sacrificio Skarn Deposit	29
Structural Controls on Ore Distribution at Mexican Skarn Deposits	34
<i>San Martin</i>	35
<i>Charcas</i>	36

Table of Contents (cont.)

<i>La Colorada – Chalchihuites District</i>	38
Conclusions	39
Acknowledgements	41
References	42
Figure Captions	51

Chapter 3

Evolution and Source of Mineralizing Fluids at the Sacrificio

Cu (Zn-Pb-Ag-Au) Skarn Deposit, Durango, Mexico	76
Abstract	77
Introduction	78
Regional Geological Setting	79
Local Geological Setting	81
Skarn-Related Mineralization	82
Alteration	84
Garnet and Clinopyroxene Mineral Chemistry	87
Structural Model	89
Fluid Inclusion Microthermometry	91
<i>Methodology</i>	91
<i>Fluid inclusion petrography</i>	93
<i>Microthermometric data</i>	94
<i>Microthermometry results</i>	96
Lead Isotope Study	98

Table of Contents (cont.)

<i>Analytical procedure</i>	98
<i>Results and interpretation</i>	99
Discussion	100
<i>Skarn classification</i>	100
<i>Source of metals and fluids</i>	101
<i>Physicochemical conditions of skarn formation</i>	101
Conclusions	104
Acknowledgements	105
References	107
Figure Captions	114

Chapter 4

General Conclusions	139
References	143

Appendices

Appendix A:	Location Map of Local Sacrificio Grid and Grid Coordinates	144
Appendix B:	Structural Data - Sacrificio Deposit	146
Appendix C:	Garnet Compositions - Sacrificio Deposit	164
Appendix D:	Pyroxene Compositions - Sacrificio Deposit	171
Appendix E:	Fluid Inclusion Microthermometric Data - Sacrificio Deposit	175
Appendix F:	General Geology, Structure, and Alteration Map - Sacrificio Deposit	179

List of Tables

Chapter 2

Table 1	Major Oxide Element and Rare Earth Element Abundances of Intrusive Rocks at the Sacrificio Deposit	73
Table 2	U-Pb Isotope Data	74
Table 3	Paragenesis of Alteration and Mineralization at the Sacrificio Deposit	75

Chapter 3

Table 4	Paragenesis of Alteration and Mineralization at the Sacrificio Deposit	135
Table 5	Representative Microprobe Analyses of Garnets and Pyroxenes from Prograde Skarn	136
Table 6	Microthermometric Data	137
Table 7	Pb Isotope Data	138

List of Figures

Chapter 2

Figure 1	Location Map of the Sacrificio Deposit	56
Figure 2	Morphotectonic and Plate-Tectonic Setting of Mexico	57
Figure 3	Simplified Geologic Map of the Sacrificio Deposit	58
Figure 4	Intrusive Phases of the Sacrificio and Coloradito Intrusions	59
Figure 5	Photographs of Major Intrusive Phases	60
Figure 6	Whole-rock Chemical Compositions of Intrusive Rocks	61
Figure 7	Rare-Earth-Element abundances of Intrusive Rocks	62
Figure 8	U-Pb Concordia Plots	63
Figure 9	Structural Geology of the Sacrificio Deposit	64
Figure 10	Equal-Area Stereonet Projections of Structural Data	65
Figure 11	Map of Skarn Alteration and Mineralization	66
Figure 12	Photographs of Mineralization Styles	67
Figure 13	Interpreted Sequence of Deformation Events	68
Figure 14	Relative timing of deformation, alteration, and mineralization	69
Figure 15	Photographs of Key Structural Features	70
Figure 16	Chemical Compositions of Intrusive Rocks from San Martin	71
Figure 17	Rare-Earth-Element abundances of Intrusive Rocks from San Martin	72

Chapter 3

Figure 18	Location Map of the Sacrificio Deposit	119
Figure 19	Simplified Geologic Map of the Sacrificio Deposit	120

Figure 20	Photographs of the Major Mineralization Styles	121
Figure 21	Map of Skarn Alteration and Mineralization	122
Figure 22	Photographs of Skarn Minerals at the Sacrificio Deposit	123
Figure 23	Iron vs. Aluminum in Grandite Garnets	124
Figure 24	Ternary Plots of Garnet and Pyroxene Compositions	125
Figure 25	Interpreted Sequence of Deformation Events	126
Figure 26	Relative timing of deformation, alteration, and mineralization	127
Figure 27	Fluid Inclusion Microphotographs	128
Figure 28	Fluid Inclusion Microthermometric Data	129
Figure 29	Trapping Temperatures and Pressures of Manto and Disseminated Mineralization	130
Figure 30	Trapping Temperatures and Pressures of Arsenopyrite- Quartz Veins	131
Figure 31	Lead Isotope Data	132
Figure 32	Pressure-Temperature Stability of Wollastonite	133
Figure 33	Temperatures of Formation of Sacrificio Skarn and Mineralization Styles	134

Acknowledgements

This project and my education in general have been greatly enriched by the support, encouragement, and guidance provided by the entire Department of Earth and Ocean Sciences at the University of British Columbia. The list of people who have helped in countless ways would fill most of this thesis, I will try to mention those who have made particularly significant contributions. To everyone else, and those I've forgotten to include in this list: thank-you.

First, I would like to thank my advisor, Dr. Stephen Rowins, for allowing me the opportunity to do this research and allowing me the latitude to pursue the aspects of this project which most interested me. Additionally, Drs. Greg Dipple, Lori Kennedy, James Mortensen, and Richard Tosdal, of the University of British Columbia have provided indispensable advice that contributed greatly to the ideas contained within this thesis. Dr. Peter Lewis of Lewis Geoscience provided critical structural advice, and is thanked for taking time out of his busy schedule to do so.

Janet Gabites, Elisabetta Pani, and Mati Raudsepp are sincerely thanked for their help with lead isotope analyses, S.E.M. studies, and electron microprobe analyses, respectively. Without their generous help, none of these studies would have been possible. Alex Allen is thanked for her help in wading through all things bureaucratic, without her help it is unlikely I would have managed to stay a registered student.

Field mapping forms the backbone of this thesis and many people contributed towards making my time in Mexico enjoyable and virtually hassle-

free. David Terry and Chris Rockingham of Boliden are thanked for their support, advice, and free flow of ideas both during fieldwork and throughout this project. David Aguilar of Luismin contributed indispensable logistical support, useful geologic ideas, and spur-of-the-moment Spanish lessons. Finally, Nena Senora ensured that our house ran smoothly and kept me out of trouble in Vicente Guerrero.

Funding for this project has been primarily provided by a generous industry grant from Boliden Limited. Additional funds have been received from a Thomas and Marguerite Mackay Memorial Scholarship and an SEGF student research grant.

Finally, I would like to acknowledge and thank the support and encouragement of my family, particularly my late grandfather who supported me in beginning this thesis and would have been proud to see its completion.

Chapter 1

General Introduction

The Sacrificio Cu (Zn-Pb-Ag-Au) skarn is located in southeastern Durango State, Mexico, and is being actively explored by Boliden Mexico S.A. de C.V., a wholly-owned subsidiary of Boliden Limited of Canada. It is an excellent example of a structurally-controlled, intrusion-related mineral deposit. Polyphase deformation both precedes, and is synchronous with, the emplacement of Middle Eocene, multiphase granitic intrusions and associated mineralization. The development of a structural model that both explains and predicts the location of skarn-related mineralization has aided ongoing exploration efforts at Cerro Sacrificio. This structural model is also applicable to many other skarn and carbonate replacement deposits of the Mexican Altiplano.

Extensive geological field mapping has been fundamental to all studies and interpretations in this thesis and has provided a solid foundation upon which to build further understanding of the Sacrificio deposit. A total of over three months were spent mapping rocks and structures in and around the Sacrificio deposit in order to ensure that interpretations derived from the laboratory-based studies are consistent with field data. Following the field program, structural data analysis, U-Pb geochronology, lithogeochemistry, fluid inclusion studies, Pb isotope studies, and electron microprobe studies were undertaken. The results of this thesis represent a significant advance in the understanding of polymetallic skarn and carbonate replacement deposits in Mexico and elsewhere in the world.

Methodology

Geological Field Mapping

Geological mapping of the Sacrificio deposit and the surrounding 2.5 x 3 km area was undertaken by the author with the aid and cooperation of Boliden project geologist, Dr. David Terry, and the University of British Columbia thesis advisor, Dr. Stephen Rowins. In total, over 7.5 km² were mapped at a scale of 1:2,000. Field data collected during the course of this mapping included: rock type, alteration mineralogy, style and intensity of alteration, sulphide mineralogy, style and intensity of sulphide development, structural relations, and the measurement of approximately 1,200 separate structural fabrics.

Structural Analysis

Subsequent to field work, structural orientation data were analyzed and interpreted by the author using a variety of data reduction methods. Stereonet projections of all data (using Stereonet 3.02 software) by area have provided the basis for the structural model presented in Chapter 2.

U-Pb Geochronological Studies

Four samples of intrusive rock from the Sacrificio property were dated using U-Pb techniques. The robust nature of the U-Pb isotopic system ensures that ages obtained reflect the crystallization age of the intrusion dated and are not influenced by subsequent hydrothermal or metamorphic events. All U-Pb

analyses were done in the Geochronology Laboratory at the University of British Columbia either by or under the direct supervision of Dr. James K. Mortensen.

Lithogeochemical Studies

Eighteen samples of intrusive rocks from the Sacrificio property were sampled and analyzed for major oxide element, trace element, and rare earth element concentrations. All analyses were done by Chemex Labs Ltd. of North Vancouver, British Columbia. These data allowed the author to classify intrusive suites by composition and to compare them with intrusive suites at the nearby San Martin skarn deposit.

Fluid Inclusion Studies

Microthermometric data were obtained from one hundred seventy eight fluid inclusions trapped in ten samples of hydrothermal quartz from three styles of mineralization at the Sacrificio deposit. Interpretation of these data provided constraints on physicochemical conditions (P-T-X) of mineralizing fluids. All analyses were done by the author at the University of British Columbia.

Pb Isotope Studies

A lead isotope study was undertaken by the author in order to constrain the source(s) of lead, and by inference, other metals in the Sacrificio deposit. Twenty-three samples of sulphide minerals, sedimentary host-rocks, and

intrusive rocks were analyzed for lead isotope composition. These data indicate a magmatic source for metals in the Sacrificio deposit.

Garnet and Pyroxene Electron Microprobe Studies

Compositions of garnet and pyroxene from skarn deposits may be used to classify the deposit by metal content (Einaudi et al., 1981; Meinert, 1992). Garnet and pyroxene compositions from four samples of prograde skarn at the Sacrificio deposit were determined by the author using the electron microprobe. This data allowed the Sacrificio deposit to be classified as a copper skarn.

Presentation

Results of this research are presented as two separate papers that will be submitted to *Economic Geology* and *Mineralium Deposita* for publication. The first paper, entitled "The Importance of Pre- and Syn-Intrusion Deformation in Controlling the Distribution of Cu (Zn-Pb-Ag-Au) Skarn Mineralization at Cerro el Sacrificio, Durango, Mexico" presents the results of geological field mapping, structural analysis, U-Pb geochronology, and lithogeochemistry of intrusive rocks. Included in the first paper is a structural model that explains and predicts the location of skarn-related mineralization within regional and local structures. The second paper, entitled "Evolution and Source of Mineralizing Fluids at the Sacrificio Cu (Zn-Pb-Ag-Au) Skarn Deposit, Durango, Mexico" combines fluid inclusion data, Pb-isotope data, and garnet and pyroxene compositional data to identify the source, composition, and physicochemical conditions (P-T-X) of

skarn formation and related sulphide mineralization. Together, these two papers provide a comprehensive model for the formation of the Sacrificio Cu (Zn-Pb-Ag-Au) deposit.

Due to the presentation of this thesis as two complementary research papers, a certain amount of duplication of information is unavoidable. Additionally, as the two papers will be submitted to the peer-reviewed journals, *Economic Geology* and *Mineralium Deposita*, American spelling has been used throughout chapters 2 and 3. It is hoped that any inconvenience to reviewers of this thesis is minimal and is justified by the benefits of timely publication in prestigious peer-reviewed geoscience journals.

References

- Einaudi, M.T., Meinert, L.D., and Newberry, R.J., 1981, Skarn Deposits, *in* Skinner, B.J., ed., *Economic Geology 75th Anniversary Volume: Economic Geology Publishing Company*, El Paso, Texas, p. 317-391.
- Meinert, L.D., 1992, Skarns and Skarn deposits, *Geoscience Canada*, v. 19, p. 145-162.

Chapter 2

The Importance of Pre- and Syn-intrusion Deformation in Controlling the Distribution of Cu (Zn-Pb-Ag-Au) Skarn Mineralization at Cerro el Sacrificio, Durango, Mexico

Keith M. Patterson

(Co-Authors: Stephen M. Rowins, James K. Mortensen, and David A. Terry)

Abstract

The structures generated during pre-intrusion regional, and syn-intrusion local, deformation events are recognized as important controls over the distribution of Cu-Zn-Pb-Ag-Au sulfide mineralization at the Sacrificio skarn deposit in southern Durango, Mexico. The Sacrificio deposit is situated in the Mexican Altiplano and is hosted by mid-Cretaceous limestone, chert, and minor shale of the Cuesta del Cura and Indidura formations. New U-Pb geochronological data indicate the presence of two temporally distinct felsic intrusive suites. The older mid-Cretaceous granodiorite-quartz monzonite suite is 109.1 ± 0.4 Ma whereas the younger Middle Eocene granite suite is 40.1 ± 0.5 Ma. Importantly, it is only the Middle Eocene granite suite which is associated with the formation of skarn and related styles of sulfide mineralization.

Three episodes of pre-intrusion regional deformation (D_1 to D_3) are recognized in the carbonate rocks at the Sacrificio deposit. D_1 and D_3 record strong east-northeast-directed shortening associated with the Mexican fold-and-thrust belt, whereas D_2 records a local re-orientation of shortening directions and has resulted in the formation of rare east-trending folds. Two episodes of intrusion-related deformation post-date regional deformation and are synchronous with the formation of mineralized skarn. The older, D_4 , is defined by the formation of a broad dome above the Sacrificio intrusion. The younger episode, D_5 , represents the opening of extensional fractures and formation of veins above and peripheral to the intrusion.

Alteration at the Sacrificio deposit is divided into pre-mineralization contact metamorphism, prograde skarn, and retrograde skarn. Three styles of skarn-related sulfide mineralization are recognized: (1) disseminated to semi-massive bornite and lesser chalcopyrite filling secondary porosity in prograde garnet skarn; (2) fracture-controlled, silver-rich, bornite-chalcopyrite \pm sphalerite \pm galena \pm arsenopyrite cutting prograde garnet skarn and marble; and (3) fine- to coarse-grained, semi-massive to massive, sulfide bodies or "mantos", which are associated with retrograde amphibole skarn and contain a sulfide assemblage of sphalerite, galena, chalcopyrite, arsenopyrite, pyrrhotite, pyrite, bornite and rare tetrahedrite, stibnite and stannite.

Prograde skarn is strongly localized along D₃ fold hinges and hosts disseminated Cu-Ag mineralization, especially where adjacent to D₅ fractures. These fractures are interpreted as the main conduits for magmatic fluids that produced the largest and best-developed zones of disseminated Cu-Ag mineralization. The base metal-rich (Zn-Cu-Pb) mantos replace marble and mineralized garnet skarn. It is proposed that the careful application of the Sacrificio structural model to many of the skarn and carbonate-replacement deposits of the Mexican Altiplano could result in new discoveries of precious and base metal mineralization.

Introduction

The geochemical and mineralogical characteristics of mineralized, intrusion-related skarns have been extensively investigated and are relatively

well-understood (e.g., Einaudi et al., 1981; Kwak, 1987; Megaw et al., 1988; Titley, 1993; Barton et al., 1995; Bowman, 1998; Meinert, 1998, 2000). In contrast, detailed studies on the structural evolution of mineralized skarn systems are limited despite an abundance of field evidence which indicates that structural fabrics commonly exert strong local and regional controls on the development and distribution of mineralization (e.g., Megaw, 1998b, 1999).

Skarns and related carbonate-replacement deposits are notoriously difficult exploration targets due to the typically narrow and discontinuous nature of the mineralized zones. Exploration strategies commonly focus on a suspected spatial zonation of mineralization in chemically reactive (i.e., calcareous) sedimentary rocks that host the skarn-forming pluton (e.g., Meinert, 1997). In many respects, the exploration strategy follows a porphyry-type model with copper and, in some cases, gold forming closest to the pluton followed by successive outward zones of silver and base metals (Zn, Pb) (e.g., Einaudi et al., 1981). Although moderately successful, this exploration model must be applied with care because it will fail if structures that focus the ore fluids are not recognized and accorded prime importance in the development of the exploration model.

In this contribution, the regional structures that formed during crustal shortening associated with the Late Cretaceous to mid-Tertiary Mexican fold-and-thrust belt (temporally and kinematically similar to the Laramide of the southwest U.S.) are shown to have been the initial conduits for skarn-forming fluids. These fluids emanated from a 40.1 ± 0.5 Ma granite intrusive complex

centered on Cerro el Sacrificio in southern Durango, Mexico. Local structures caused by stress generated during emplacement of this intrusive complex subsequently exerted a later and more local control over the distribution of Cu-Zn-Pb-Ag-Au mineralization. This interplay between pre-intrusion regional tectonic stress and syn-intrusion magmatic stress has resulted in the present-day configuration of the mineralized zones comprising the Sacrificio deposit. Careful field studies and detailed examination of diamond drillcore has failed to demonstrate a stratigraphic control on skarn and sulfide mineralization within the thick, sequence of interbedded Cretaceous limestone and chert that hosts the deposit. Consequently, although important for the overall development of the skarn system, host-rock composition has played a subordinate role to that of pre-existing structures in controlling the distribution of sulfide mineralization at the Sacrificio deposit.

The exploration concepts arising from this study of the Sacrificio deposit may be directly applied to many skarn and carbonate-replacement deposits throughout the Altiplano of central Mexico. Many of these deposits are associated with comparably aged mid-Tertiary granitoids and have formed in similar metasedimentary rock sequences possessing well-developed Mexican fold-and-thrust belt deformation fabrics. Moreover, many skarn and carbonate-replacement deposits in the Altiplano have local deformation fabrics superimposed over regional ones, with the former likely due to the emplacement of mineralizing mid-Tertiary granitoids. Application of the structural model developed at the Sacrificio deposit could identify significant zones of

mineralization in portions of skarn and carbonate-replacement systems previously deemed unmineralized.

Property History

The Sacrificio deposit is located 80 km southeast of Durango, in a well-recognized northwest-trending belt of mining districts including San Martín, Fresnillo, La Colorada, Zacatecas, and Francisco I. Madero (Fig. 1). This belt occurs along the western edge of the Mexican Altiplano (Fig. 2). The Sacrificio deposit is centered on Cerro el Sacrificio which has seen a long history of small-scale mining, evidenced by the many small workings and waste-dumps scattered around the mountain. The most recent mining activity focussed on copper-rich skarn mineralization at Mina Embotelladora located on the northern flank of Cerro el Sacrificio (Fig. 3). Production data are not available, but a geological reserve of 40,000 t of ore grading 50 g/t Ag, 0.5% Cu, 0.05% Pb, and 0.05% Zn was calculated by Albinson and Sanchez (1977). In this paper, the term deposit is used to describe skarn-related sulfide mineralization at Cerro el Sacrificio because of the approximately 15 years of production activity at Mina Embotelladora.

Exploration of the Sacrificio property by Luismin S.A. de C.V. began in 1977 and continued intermittently to 1997. Work during this period consisted of geological mapping, geochemical and geophysical surveys, and several reverse circulation and diamond drilling programs (32 holes totaling 7,540 m). These programs targeted skarn mineralization exposed primarily around the base of

Cerro el Sacrificio. The most significant mineralization discovered during the Luismin work was encountered in diamond drillhole (DDH) LB96-04. This hole intersected 24.3 meters of disseminated and vein/veinlet sulfide mineralization averaging 0.3 g/t Au, 120 g/t Ag, and 1.72% Cu in garnet skarn immediately north of Mina Embotelladora.

In 1997, Boliden Limited entered a joint-venture agreement with Luismin to further explore the Sacrificio property. A geological re-evaluation of the property in 1998 led to a diamond drilling program which targeted the hinge zone of a large anticlinal structure (the "Central Anticline") on the northern flank of Cerro el Sacrificio (Rowins, 1998). This program identified several well-developed zones of copper, zinc, lead, and silver mineralization, including several carbonate-replacement horizons of massive to semi-massive sulfides termed "mantos". The best manto (in terms of grade and thickness) was intersected in DDH SAC98-3, located just west of the Central Anticline hinge zone on Pad 3 (Fig. 3). This hole had an intersection of 16.4 meters averaging 1.48% Zn, 1.34% Cu, 0.99% Pb and 174.6 g/t Ag (Terry et al., 1999). Further drilling by Boliden in 2000 identified additional manto-style mineralization on the south flank of Cerro Coloradito.

Methods Employed

Between 1998 and 2000, the authors spent approximately 145 man-days mapping the Sacrificio deposit and surrounding ~2.5 x 3 km area at a scale of 1:2,000. During this geological mapping, approximately 1,200 structural measurements were collected and plotted together with lithological units, and

styles and intensity of alteration and mineralization. Diamond drill programs by Boliden Limited in 1998 and 2000 were planned and directed by two of the authors (S.M.R. and D.A.T.), and 12 of the 15 holes cored on the property during these programs were logged by the authors. Eighteen representative samples of the different types of intrusive rocks at the Sacrificio deposit were analyzed for major oxide element, trace element, and rare earth element compositions by ICP-MS. Four samples of intrusive rock were dated by U-Pb geochronological methods at the University of British Columbia. To identify types and styles of alteration and mineralization, fifty-five polished thin sections were studied by transmitted and reflected light microscopy accompanied by complimentary scanning electron microscope and electron microprobe analysis.

Regional Geology

Geographical Setting

The Sacrificio deposit lies within the Altiplano of central Mexico (Figs. 1 and 2). The Altiplano is situated north of the Trans Mexican Volcanic Belt between the Sierra Madre Occidental and the Sierra Madre Oriental tectono-stratigraphic provinces (e.g., Sedlock et al., 1993). The Sierra Madre Occidental to the west is a region of extensive, flat-lying, felsic, Tertiary volcanic rocks whereas the Sierra Madre Oriental to the east is a region of thrust and folded Mesozoic sedimentary rocks (e.g., Campa and Coney, 1983; Sedlock et al., 1993). The Altiplano primarily consists of deformed Late Jurassic to Cretaceous marine carbonate rocks with interbedded chert and shale. This metasedimentary

rock sequence, which contains in excess of 3000 m of carbonate strata (e.g., Megaw et al., 1988), is intruded by mid-Tertiary plutons ranging from granite to diorite in composition. In addition to causing extensive hydrothermal alteration of the adjacent carbonate host-rocks, these plutons are largely responsible for the precious and base metal-rich mineral deposits of the Altiplano (e.g., Rubin and Kyle, 1988; Barton et al., 1995; Megaw, 1999).

Altiplano stratigraphy

Stratified rocks of the Altiplano are dominated by platform carbonate rocks which were deposited in the westernmost extension of the ancestral Gulf of Mexico during the Late Jurassic to Cretaceous (Longoria et al., 1999). Evaporites are locally abundant. Intercalated with the carbonate rocks and evaporites are minor shale and flysch deposits derived from a magmatic arc to the west (Sedlock et al., 1993). The composition of the pre-Jurassic basement in this region is poorly known, although inferences of Proterozoic continental crust have been made from Nd isotopic studies of xenoliths within Quaternary volcanic rocks (Ruiz et al., 1988).

Intrusive rocks

Geochemical, mineralogical, and geochronological data for intrusive rocks of the Altiplano are sparse, excluding those intrusions associated with mineral deposits (e.g., Barton et al., 1995; Damon et al., 1981; Megaw, 1999). Available geochronological data indicate that intrusions range from 30 Ma to 46.6 Ma in

age (Megaw, 1999). These ages are coeval with volcanic rocks of the "lower volcanic complex" of the Sierra Madre Occidental magmatic arc (Coney, 1978). The intrusions are commonly multiphase and cut by late felsic dykes. The compositions of both intrusions and dykes vary widely and include granite, granodiorite, quartz monzonite, and diorite (e.g., this study; Barton et al., 1995).

Tectonic setting

Rocks of the Altiplano have undergone a long history of progressive deformation including both contractional and extensional strain (Campa and Coney, 1983; Sedlock et al., 1993). The dominant northwest-trending structural fabric of the area is attributed to strong north-northeast-directed contraction associated with the Late Cretaceous to Middle Eocene (~70 to 45 Ma) Mexican fold-and-thrust belt. This deformation event is both temporally and kinematically equivalent to the "Laramide" orogeny of the southwestern United States (e.g., Sedlock et al., 1993). The Sacrificio deposit lies in the westernmost or hinterland portion of the Mexican fold-and-thrust belt, where regional folding is intense (Campa and Coney, 1983).

Deformation associated with the Mexican fold-and-thrust belt is generally thin-skinned with only minor local involvement of Precambrian crystalline basement (e.g., Sutter, 1987; Sedlock et al., 1993). In the Altiplano and Sierra Madre Oriental, folding and thrusting verges generally northeast to east-northeast, consistent with deformation throughout the North American Cordillera (e.g., Drewes, 1991). Cumulative east-northeast displacement across the belt is

on the order of 40 to 200 kms, with up to 30% shortening (Sedlock et al., 1993). The deformation front of the Mexican fold-and-thrust belt was spatially time-transgressive, with deformation younging to the east (de Cserna, 1989). Importantly, magmatism occurred simultaneously with deformation, but somewhat west of the thrust front and therefore after peak deformation (Sedlock et al., 1993). This simple relationship explains the post- to syn-deformational timing of pluton emplacement at Cerro el Sacrificio and at many other intrusion-related mineral deposits in central Mexico (e.g., Megaw, 1999).

Contraction in the fold-and-thrust belt ended by approximately 31 Ma and was followed by east-northeast-directed extension (Henry et al., 1991; James and Henry, 1991). This extension is marked by block tilting, normal faulting, and magmatism throughout the basin-and-range province of the southwestern United States and north-central Mexico. In the Altiplano, normal faulting and associated basaltic magmatism were initiated by approximately 24 Ma and continues to the present. This has resulted in the broad basin-and-range topography developed throughout the region today (Sedlock et al., 1993).

Property Geology

Stratigraphy

Sedimentary rocks exposed on and around Cerro el Sacrificio belong to the mid-Cretaceous (Albian to Cenomanian; Longoria et al., 1999) Cuesta del Cura Formation and are composed mainly of 10 to 40 cm thick beds of grey limestone interbedded with 1 to 10 cm thick beds of chert. These rocks are

conformably overlain by limestone and shale of the mid-Cretaceous (Cenomanian to Santonian) Indidura Formation. The contact between formations is gradational in nature and is defined by the presence of shale beds in the Indidura Formation. Together, the Cuesta del Cura and Indidura formations comprise a thick, monotonous, succession of marine sedimentary rocks with no discernable marker horizon(s). These rocks are moderately to strongly recrystallized, with limestone transformed to marble and chert to an assemblage of quartz, albite, and scapolite.

Intrusive rocks

Intrusive rocks on the property are divided into two suites based on age and chemical composition. The oldest suite, dated at 109.1 ± 0.4 Ma (see U-Pb geochronology section below), consists of a large northwest-trending dike (Dique Viejo) exposed on Cerro el Sacrificio and several narrower dikes cropping out immediately southeast of Cerro Coloradito (Fig. 4). Dique Viejo is a 10 to 30 m wide, feldspar-phyric dike of monzonitic composition (see below). It is cut by the Sacrificio intrusion (Fig. 4), and is essentially unaltered with the exception of minor chlorite and epidote (Figs. 5A and B). The narrow dikes exposed on Cerro Coloradito are petrographically and geochemically very similar to Dique Viejo (see below) and, consequently, are interpreted to be of the same age.

The 39.8 ± 0.1 Ma Sacrificio intrusion is exposed on the western flank of Cerro el Sacrificio and forms the core of the mountain as indicated by exploration drilling and geophysical surveys (Fig. 3). A relatively homogeneous body of

medium-grained granite that is weakly quartz- and feldspar-phyric is the dominant rock type (Figs. 5C and D). Portions of the intrusion are surrounded by a thin margin of highly felsic, possibly rhyolitic, quartz-phyric porphyry. This felsic margin is analogous in its geometry and composition to the quartz-phyric rhyolite that envelopes the Cerro del Gloria stock at the San Martin Cu-Zn-Pb-Ag skarn deposit (Rubin and Kyle, 1988). Geophysical data suggest that the subsurface extent of the Sacrificio intrusion is approximately 1500 x 2000 metres in plan view (Fig. 3).

The 40.3 ± 0.2 Ma Coloradito intrusion is exposed one kilometer northwest of the Sacrificio intrusion on the western flank of Cerro Coloradito. It appears smaller in subsurface extent than the Sacrificio intrusion based on geophysical data (Terry et al., 1999). The Coloradito intrusion is multiphase and consists of a granite core characterized by medium- to coarse-grained phenocrysts of quartz, orthoclase, and plagioclase in a fine-grained groundmass of quartz and minor feldspar (Figs. 5E and F). This core is surrounded by a thin (5 to 15 m wide) margin of fine- to medium-grained, biotite-rich granite (Figs. 5G and H). Immediately adjacent to these intrusive phases is a 15 to 100 m wide zone of intense silicification. Relict quartz phenocrysts indicate that this silicified rock was originally granitic in origin. The granite dykes cropping out on Cerro Coloradito are typically porphyritic with a variable phenocryst assemblage of quartz, orthoclase, and rare plagioclase.

Representative samples of all intrusive phases were analyzed for major oxide elements, trace elements and rare earth elements (REE). These data,

plotted in figures 6 and 7 and listed in Table 1, illustrate that there are distinct compositional differences between the older and younger intrusive suites. The Middle Eocene suite is granite in composition whereas the older Cretaceous suite ranges in composition from quartz monzonite to granodiorite.

Rare earth element abundances, normalized to the primitive mantle values of Sun and McDonough (1989), are consistent with major element compositional differences between the two suites (c.f., Fig. 6). The Cretaceous dykes are enriched in light REE, with primitive mantle-normalized REE diagrams displaying steep slopes and small negative europium anomalies, whereas the Eocene intrusions possess much flatter REE patterns and have large negative europium anomalies. It is beyond the scope of this study to address the petrogenetic and tectonic significance of these features in detail, especially given the lack of consensus on the tectonic setting of this part of Mexico in the Middle Eocene (e.g. Henry et al., 1991; Sedlock et al., 1993). As a generalization, however, the REE patterns of the Cretaceous suite are characteristic of magmas derived from deep crustal or mantle sources, whereas the REE patterns of the Eocene suite are typical of shallow crustal melts that have undergone significant fractionation of plagioclase (Rollinson, 1993).

U-Pb geochronology

Four samples of intrusive rock from the Sacrificio deposit were dated by U-Pb methods at the University of British Columbia. Zircon concentrates were prepared from 15-20 kg samples using conventional crushing, grinding, Wilfley

table, heavy liquids and magnetic separation techniques. The methodology for zircon grain selection, abrasion, dissolution, geochemical preparation and mass spectrometry is described by Mortensen et al. (1995). Most zircon fractions were air abraded (Krogh, 1982) prior to dissolution to minimize the effects of post-crystallization Pb-loss. Procedural blanks were 5 to 2 pg for Pb and 1 pg for U. Uranium-lead data are given in Table 2, and are shown on conventional U-Pb concordia plots in Figure 8. Errors attached to individual analyses were calculated using the numerical error propagation method of Roddick (1987). Decay constants used are those recommended by Steiger and Jäger (1977). Compositions for initial common Pb were taken from the model of Stacey and Kramer (1975). All errors are given at the 2σ level.

Sample KP-11 is porphyritic granite from the Coloradito intrusion (Fig. 4). The sample yielded abundant high quality zircons, mostly comprising clear, pale to medium brown, square, stubby prismatic forms. The grains displayed faint igneous growth zoning; they typically contained rare to abundant clear, bubble-shaped inclusions but no inherited cores were observed. The best quality, least magnetic, most inclusion-free grains were strongly abraded and then split into five subequal fractions for analysis. Measured U-contents are very high (8713-14149 ppm; Table 2). Four of the analyses yield concordant analyses (Fig. 8A). The interpreted crystallization age for the sample is assigned on the basis of the total range $^{206}\text{Pb}/^{238}\text{U}$ ages of fractions B and C (40.3 ± 0.2 Ma). Two of the fractions (D and E) are also concordant but give slightly younger $^{206}\text{Pb}/^{238}\text{U}$ ages, and are interpreted to have suffered minor post-crystallization Pb-loss. Fraction A

is discordant with an older $^{207}\text{Pb}/^{206}\text{Pb}$ age (57.8 Ma) and is interpreted to have contained a minor inherited component, presumably as "cryptic cores" that could not be detected visually.

Sample KP-14 is porphyritic granite from a large dike at Cerro Coloradito. Zircons from this sample are similar to those from the previous sample, except that these grains are typically less clear due to the presence of fractures and inclusions. Four fractions of the best quality zircon available were analyzed following strong abrasion. As with the previous sample, measured U-contents are very high (8013-12904 ppm; Table 2). Three of the four analyses are concordant (Fig. 8B) and the interpreted age for the sample of 40.2 ± 0.2 Ma is based on the total range $^{206}\text{Pb}/^{238}\text{U}$ ages of fractions C and D. Fraction B has suffered post-crystallization Pb-loss, and fraction A contained a minor inherited zircon component.

Sample KP-7 is medium-grained granite collected from the Sacrificio intrusion (Fig. 4). The sample yielded abundant clear, colorless, stubby to elongate, square prismatic zircons, with rare to abundant clear inclusions but no visible inherited cores. Five strongly abraded fractions were analysed (Table 2). Two fractions (B and D) yield concordant analyses, and the $^{206}\text{Pb}/^{238}\text{U}$ age of fraction B (39.8 ± 0.1 Ma) is interpreted to provide a minimum crystallization age for the sample (Fig. 8C). Fraction D is interpreted to have experienced Pb-loss, and the other three fractions (A, C and E) contain an inherited zircon component.

Sample KP-9 is porphyritic monzodiorite from Dique Viejo. Zircons from this sample are quite different in appearance from those in the previous three

samples. The grains are pale yellow, stubby to elongate, square prisms with simple to multifaceted terminations. Several grains in the coarser, non-magnetic fractions contain cloudy inherited cores. Initially five fractions of the best quality, core-free, least magnetic zircon were analyzed; these all gave Early Mesozoic to mid-Paleozoic $^{207}\text{Pb}/^{206}\text{Pb}$ ages and clearly contained a significant inherited zircon components. Subsequent fractions were selected on the basis of grain morphology to try to avoid inherited cores, including two fractions (H and I) that consisted of tips broken from grains with visible cloudy cores. Despite these efforts, all of the coarser fractions still appear to have contained inherited components. Finally two fractions of fine-grained, very elongate needles were selected (fractions J and K, Fig. 8D), and were analyzed without abrasion. The finest grained fraction (K) yields a concordant analysis with a $^{206}\text{Pb}/^{238}\text{U}$ age of 109.1 ± 0.4 Ma. As this fraction was not abraded prior to dissolution, it is likely that it has suffered at least minor post-crystallization Pb-loss; however the analysis is concordant, and it is therefore unlikely that the crystallization age of this body is significantly older than the $^{206}\text{Pb}/^{238}\text{U}$ age.

Structure

The most striking structural feature at the Sacrificio deposit are the many north-northwest trending folds (Fig. 9). These are divided into two types (D_1 and D_3) based on fold morphology, overprinting relationships, and vergence. D_1 folds are tight to isoclinal, asymmetric, inclined to rarely recumbent, and typically display west vergence. This vergence contrasts with the general east-vergence

of the Mexican fold-and-thrust belt. Folds associated with the D_3 event are large amplitude (hundreds of metres), gentle to open, upright folds which refold D_1 folds with similarly oriented fold axes (i.e. type 3 refolding; McClay, 1987).

Between the D_1 and D_3 folding events there was a minor re-orientation of shortening directions resulting in rare east-trending folds that refold D_1 folds (i.e. type 2 refolding; McClay, 1987). D_2 had limited effect on the present form of stratified rocks at the Sacrificio deposit, but it is mapped unambiguously at several locations. Similar in style to D_1 folds, the D_2 folds generally possess close to tight interlimb angles.

D_4 is defined by the plunges of D_1 and D_3 fold axes. In rocks above the northern half of the intrusion, D_1 and D_3 fold axes plunge to the north-northwest whereas above the southern half of the intrusion, these fold axes plunge to the south-southeast (Fig. 10). The resulting structure is a broad dome centered on Cerro el Sacrificio, directly above the Sacrificio intrusion.

D_5 is defined by fractures and veins that cut all other mapped structures, generally have steep dips, and strike east-northeast. Detailed interpretation of the origin of all these structural fabrics is given below in the section on structural evolution of the deposit.

Mineralization

Mineralization and related calc-silicate skarn at the Sacrificio deposit is largely confined to metasedimentary host-rocks adjacent to the Middle Eocene intrusions (exoskarn). The intrusive rocks are devoid of skarn and sulfide

minerals other than very near the intrusive margin where weak endoskarn is rarely developed.

Three different styles of sulfide mineralization are recognized at the Sacrificio deposit. These are: (1) disseminated to semi-massive bornite and lesser chalcopyrite filling secondary porosity in garnet skarn; (2) fracture-controlled bornite-chalcopyrite \pm sphalerite \pm galena \pm arsenopyrite with high silver contents, typically on the order of several hundred grams per tonne; and (3) fine- to coarse-grained semi-massive to massive sulfide bodies (mantos) which have replaced marble or garnet skarn and comprise a variable assemblage of sphalerite, galena, chalcopyrite, arsenopyrite, pyrrhotite, pyrite, and bornite (Fig. 11). Fracture-controlled and disseminated styles of mineralization are related both spatially and genetically but distinct differences in mineralogy and areal distribution require that they be classified as separate styles of mineralization. Note that where fractures are filled by minerals, they are referred to as veins in accordance with the terminology of the American Geological Institute (AGI) (Bates and Jackson, 1983).

Disseminated Cu-Ag mineralization

Disseminated Cu-Ag mineralization is synchronous with, but also slightly post-dates, the D₅ fracture-controlled mineralization. It is the most widespread style of mineralization at the Sacrificio deposit and consists of small (0.1 to 3 mm in diameter) disseminations of bornite and lesser chalcopyrite in secondary porosity within garnet and wollastonite skarn (Fig. 12A). Relatively large areas

(hundreds to thousands of square metres, e.g., Fig. 11) host uniformly disseminated sulfide minerals on surface. Significant drill intersections of this style of mineralization include 1.72% Cu and 121 g/t Ag over 24.3 metres (Terry et al., 1999).

Fracture controlled Cu-Ag±Au mineralization

The oldest mine workings at the Sacrificio deposit are located along narrow zones of intense fracture-controlled mineralization (Fig. 12B). Although these zones are generally of limited tonnage, they commonly contain very high grades of copper and silver (drill core intersections include 6.51% Cu and 554 g/t Ag over 1.5 m). Fractures generally strike between 060° and 100° and dip steeply to either the north or south. Where fractures are filled by sulfide and gangue minerals to form banded veins, mineral growth fibers are consistent with the veins having formed by extensional processes (e.g., Fig. 12C). Sulfides in the fracture-controlled style of mineralization may occur as coatings on fractures, as fillings in veins, and as disseminations proximal (i.e., within about 30 cm) to the fractures. This disseminated mineralization proximal to the fractures grades into the more widespread disseminated mineralization described above, but is differentiated from it based on the presence of sulfides other than bornite and chalcopyrite, and its greater concentrations nearest to the fractures.

Veins associated with the fractures typically are filled with quartz, calcite, and up to about 5% sulfide minerals. The sulfide mineral assemblage is dominated by chalcopyrite and/or bornite with minor sphalerite, galena, and

arsenopyrite. Veins are composed rarely of massive to semi-massive sulfide. Fractures and veins commonly occur together in zones several tens of metres wide with centimetre- to metre-scale spacing between individual fractures. Vein widths range from millimetres to tens of centimetres, with typical thicknesses on the order of 1 to 10 cm. Secondary copper minerals such as malachite, azurite, and chrysocolla commonly are developed in fracture zones through oxidative weathering of primary sulphide minerals.

Manto-style Zn-Cu-Pb-Ag-Au mineralization

The recent discovery of massive to semi-massive polymetallic mantos at the Sacrificio deposit greatly improves its economic potential and bodes well for the likelihood of delineating further mantos. The sulfide mineralogy of the mantos consists of sphalerite, galena, chalcopyrite, arsenopyrite, pyrrhotite, pyrite, bornite and rare tetrahedrite, stibnite and stannite (Fig. 12D). High abundances of silver and, locally, gold are present in several of the mantos. The most economically important drill intersection of this style of mineralization occurs in diamond drill hole SAC98-03 drilled off Pad 3 (e.g., Fig. 3). This hole intersected 16.43 m of 1.48% Zn, 1.34% Cu, 0.99% Pb, and 174.6 g/t Ag. Other significant zones of manto-style mineralization identified on surface include Rosas de Diciembre, Santo Niño, Pad 4, Verde Pit, Windmill shaft and Hueco Grande (Fig. 3).

Contact relationships between the mantos, prograde garnet-wollastonite skarn, and marble reveal that the mantos post-date the development of prograde

skarn and marble. The common gangue minerals in the mantos are characteristic of retrograde skarn assemblages and include amphibole, chlorite, and calcite. Together, these data indicate that the manto mineralization post-dates the disseminated Cu-Ag and fracture-controlled Cu-Ag \pm Au mineralization.

Alteration

Alteration is divided into three types at the Sacrificio deposit. These are (1) pre-mineralization contact metamorphism, (2) prograde skarn, and (3) retrograde skarn. As noted above, disseminated and fracture-controlled Cu-Ag \pm Au mineralization is associated with prograde skarn whereas the polymetallic mantos are associated with retrograde skarn. The contact metamorphism forms a large halo around the intrusions unlike the distribution of prograde and retrograde skarn, which is strongly controlled by proximity to well-developed structures. The general paragenetic sequence of alteration and corresponding mineralization events is given in Table 3.

The earliest and largest-scale alteration event identified at the Sacrificio deposit is the pervasive development of hornfels in limestone and chert during emplacement of the Sacrificio and Coloradito intrusions (Fig. 11). Alteration minerals formed during this contact metamorphic event include quartz, albite, scapolite, and minor chlorite-sericite. This assemblage preferentially replaces chert beds (but locally also replaces limestone) in a concentric halo up to 500 m around the intrusions. The distribution of hornfels is controlled only by proximity to the intrusions - it is unaffected by the structures that localized prograde and

retrograde skarn. This hornfels is a product of heat generated by the intrusions and likely involves meteoric waters circulating locally within the rocks (e.g., Einaudi et al., 1981).

Structurally controlled prograde skarn is the most strongly developed and widespread type of hydrothermal alteration developed on surface at the Sacrificio deposit (Fig. 11). It hosts disseminated bornite-chalcopyrite mineralization. The prograde skarn is dominantly massive to poddy andradite garnet with lesser wollastonite, clinopyroxene, and vesuvianite. The euhedral, coarse-grained (up to 2 cm in diameter) garnet crystals invariably display both optical and compositional zonation. From thin section petrography it is estimated that garnet skarn contains 10 to 15% intergranular porosity. This porosity and corresponding permeability have played a key role in localizing subsequent disseminated bornite-chalcopyrite mineralization. At the scale of outcrop, garnet, wollastonite, clinopyroxene, and vesuvianite generally occur together as prograde skarn, although at the scale of hand sample and thin section, a zonation is recognized from proximal, garnet to garnet+clinopyroxene to more distal wollastonite+vesuvianite as distance from a fracture increases.

Retrograde skarn is not particularly widespread but does occur at several locations on the Sacrificio property. It is commonly associated with manto-style mineralization and is defined by dark green, pervasive, poddy to irregular veinlets of amphibole and chlorite. Retrograde skarn exposed on surface occurs in zones tens to hundreds of square meters in size distributed peripherally to the Sacrificio and Coloradito intrusions (Fig. 11). Significant retrograde skarn is cut by several

old mine workings created to access the polymetallic mantos. These include the Santo Niño shaft and the Rosas de Diciembre adit (e.g., Fig. 3). The most geologically interesting and economically important intersection of retrograde skarn occurs in drillhole SAC98-03 where amphibole skarn clearly post-dates prograde garnet-wollastonite skarn and is associated with a high-grade polymetallic manto.

In addition to the major types of alteration described above, there are several other less abundant styles of alteration present at the Sacrificio deposit. These include (1) pervasive silicification of early phases of the Coloradito intrusion, (2) zones of quartz vein stockworks peripheral to the Sacrificio intrusion, and (3) small zones of quartz-cemented limestone breccia above the Sacrificio intrusion (Fig. 11). Intense silicification peripheral to the Coloradito intrusion is probably deuteric in origin and almost completely replaces earlier intrusive phases (whole-rock analyses of this silicified zone identify rock compositions containing up to 93.9% SiO_2 ; Table 1). The quartz vein stockworks exposed at the margins of the Sacrificio and Coloradito intrusions are generally weakly developed although there are local zones of intense development. These stockworks likely are related to the same late-stage, volatile-rich, magmatic fluid exsolution event that produced a small zone of post-skarn breccia above the Sacrificio intrusion (Fig. 11).

Structural Evolution of the Sacrificio Skarn Deposit

Five separate deformation events are recognized in rocks exposed on and around Cerro el Sacrificio. With the exception of the latest events (D_4 and D_5), which are due to pluton emplacement, all likely formed during progressive deformation associated with the Mexican fold-and-thrust belt. A sequential rendition of deformation and associated mineralization from D_1 to D_5 is schematically illustrated in Figure 13. The relevant paragenetic relationships are shown in Figure 14.

D_1 is a relatively ductile, passive, folding event that records an estimated 100 to 150% shortening in the area of Cerro el Sacrificio. D_1 folds are tight to isoclinal, rarely recumbent, and generally have amplitudes between 10 cm and 3 m. D_1 folds are strongly asymmetric and typically verge to the west (Fig. 15A). This contrasts with the general east-vergence of the Mexican fold-and-thrust belt and likely places the Sacrificio deposit in a back-thrust portion of the fold-and-thrust belt hinterland (Sutter, 1987). D_1 fold axes trend towards 330° with a maximum shortening direction of east-northeast.

D_2 is a minor event likely caused by a local realignment of regional stresses as a result of strain partitioning or extreme competency contrast. It has limited effect on the present form of the stratified rocks in the mapped area, but it is unambiguously recognized at several outcrops (e.g., Fig. 15B). The style of folding is similar to D_1 and hence D_2 is interpreted to predate the less passive and intense D_3 event. D_2 consists of type 2 refolding of D_1 folds (fold axial surfaces approximately perpendicular). D_2 fold axial surfaces presently strike

approximately 100° and dip 40° to the south, although because this orientation has been rotated by an undefined amount of younger deformation, it bears little relation to the D_2 stress orientations. It is not possible to separate the effects of D_2 from the bulk of the bedding orientation data (Fig. 10), but it is likely that D_2 is responsible for the moderate scatter of poles to bedding from the great circle girdle which defines D_1 and D_3 folding.

D_3 folding is the most important deformation event defined at Sacrificio with respect to control over mineralization. D_3 folds are large amplitude (hundreds of metres), gentle to open, upright folds (Fig. 15C) which refold D_1 folds with similarly oriented fold axes (type 3). As discussed below, D_3 fold axial surfaces, particularly in anticlines, have focussed ascending metalliferous and skarn-forming magmatic fluids leading to the present distribution of garnet skarn and disseminated Cu-Ag mineralization. The largest and most strongly mineralized D_3 fold mapped at the Sacrificio deposit is termed the Central Anticline (Fig. 3). D_3 is separated from D_1 based on distinct differences in fold style and by the consistent west-vergence of D_1 folds irrespective of their location within D_3 fold geometries. D_3 fold axes trend toward 330° and plunge gently to the north or south depending on their location within the dome produced by D_4 (Figs. 9 and 10).

D_4 is attributed to the forceful emplacement of the Sacrificio intrusion, which has resulted in the gentle doming of rocks above and around the intrusion. As noted above, D_4 is defined by the opposing plunges of D_1 and D_3 fold axes in rocks above the northern and southern halves of the intrusion, respectively (Figs.

9 and 10). Fluids released from the crystallizing Sacrificio intrusion were channeled upward along D₃ fold axial surfaces as evidenced by the localization of prograde skarn. The exact mechanism(s) by which these fluids were channeled into fold hinges is unknown, but probably involves the combined effects of contrasting permeabilities between metasedimentary beds and the presence of axial-planar fractures and/or cleavages in the hinge areas of both anticlines and synclines. Upward channelization of fluid along bedding planes into antiform hinges is a well documented process (i.e., the oil-trap analogy), as is fluid migration up axial-planar cleavages (North, 1985). Where magmatic fluids reacted with limestone, garnet skarn with significant porosity was produced and accompanying permeability was localized along D₃ fold hinges. At the Sacrificio deposit, secondary porosity is observed in both thin sections and hand samples of mineralized and unmineralized garnet skarn.

Continued exsolution of magmatic fluids from the crystallizing Sacrificio intrusion (or a subsequent intrusive phase) is proposed to have raised local pore fluid-pressure sufficiently to cause mode I (extension) hydrofractures (D₅) to form above the intrusion. D₅ fractures are dominantly steeply dipping and generally strike east-northeast (Fig. 9), an orientation possibly indicating weak east-northeast oriented regional compressional stress was still operative at this time. These newly formed fractures preferentially channeled metalliferous fluids exsolved from the intrusion. Fluids then migrated from the fractures into porous garnet skarn. This fluid channelization has resulted in significant concentrations of disseminated bornite and lesser chalcopyrite in garnet skarn proximal to the D₅

fractures (Fig. 15D). The sequence of events presented here is consistent with field evidence that shows intersections between garnet skarn and D₅ fractures characteristically host strong disseminated bornite-chalcopyrite mineralization.

The precise mechanism(s) controlling the localization of manto-style mineralization is less well understood than that of the disseminated and fracture-controlled styles, but the late development of the mantos is consistent with fluid evolution models in many mineralized skarn systems (e.g., Einaudi and Burt, 1982; Meinert, 1997). Moreover, such a temporal relationship is documented in many Mexican skarns and carbonate-replacement deposits similar to Sacrificio (e.g., Megaw, 1999). However, the mantos at Sacrificio do differ from those found in typical polymetallic skarns in one respect: they do not occur outboard of the "copper" zone (e.g., Meinert, 1997). Rather, they occur within the copper zone near the intrusive contact where they have replaced both mineralized and unmineralized prograde garnet skarn. This intrusion-proximal position of the Sacrificio mantos may indicate that a deeper intrusive phase(s) is responsible for their formation. Alternatively, the proximal position of the mantos may be a function of the cooling intrusive complex. Analogous to a porphyry copper system, earlier formed structures may channel late, retrograde, fluids back into the central portions of the ore system where replacement and base metal deposition occurs (e.g., Einaudi and Burt, 1982; Johnson and Norton, 1985).

Structural Controls on Ore Distribution in Mexican Skarn Deposits

Studies of skarn deposits in Mexico and elsewhere typically have focussed on the mineralogical and geochemical aspects of the skarn and associated intrusive rocks (e.g., Gilmer et al., 1988; Graf, 1997; Meinert, 1998; Rubin and Kyle, 1988). The effect of structure in controlling the distribution and development of skarn and associated mineralization is rarely addressed in detail. A review of the literature reveals that several major skarn-related deposits in Mexico appear to exhibit a significant degree of structural control over their development. These include San Martin/Sabinas (Ruben and Kyle, 1988), La Colorada (Moore, 1999), Charcas (Castañeda, 1991), Velardeña (Gilmer et al., 1988; Hernandez, 1991), Providencia (Sawkins, 1964), Ojuela (McLeroy et al., 1986) and Naica (Palacios et al., 1991). In this section, the geological characteristics of the best studied of these skarn deposits are reviewed and the structural controls over mineralization are investigated. Although data are insufficient for our analysis to be comprehensive, we believe it is possible to assess the general compatibility of the structural model developed for the Sacrificio deposit with the structures and patterns of mineralization present in the aforementioned deposits.

San Martin

The San Martin (and neighboring Sabinas) deposit is the largest skarn deposit in Mexico (Megaw, 1998a). Total reserves and past production are approximately 70 Mt at average grades of 3.8% Zn, 1% Cu, 0.5% Pb, and 125 g/t

Ag (Megaw, 1999). The mine site is located approximately 20 kilometers south of Cerro el Sacrificio (Fig.1).

Mineralization at San Martin is localized along the west side of the Cerro de la Gloria stock, a polyphase granitic intrusion dated at 46.2 ± 0.1 Ma by K-Ar methods (Damon et al., 1983). Compositions of the intrusive phases of the Cerro de la Gloria stock vary from granite to granodiorite, similar to those of the Middle Eocene intrusions associated with the Sacrificio deposit (Fig. 16). A single sample of intrusive rock from San Martin plots within the mid-Cretaceous field for Sacrificio but owing to the similarity of REE abundances (Fig. 17), this sample probably represents a less differentiated phase of the Eocene Cerro de la Gloria stock rather than a mid-Cretaceous granodiorite as at Sacrificio. Rare earth element abundances of the Middle Eocene mineralizing intrusions at the Sacrificio deposit are remarkably similar to those of intrusions at San Martin. This demonstrates that both intrusive centers have likely formed during the same tectonomagmatic event.

The pre-mineralization structures at San Martin are very similar to those at the Sacrificio deposit: tight, northwest-trending folds are ubiquitous within Cuesta del Cura Formation limestone and are attributed to shortening during formation of the Mexican fold-and-thrust belt. Large-scale doming is evident around the Cerro de la Gloria stock (Rubin and Kyle, 1988), however, skarn and stratified rocks above the intrusion have been eroded away unlike the Sacrificio deposit where this mineralized cap remains.

Skarn mineralization at San Martin is centered around three main east-northeast-striking veins: (1) the Ibarra, (2) the Ramal Ibarra, and (3) the San Marcial (Rubin, 1986). These veins likely represent the conduits for mineralizing fluids that produced the extensive manto mineralization peripheral to the veins (e.g., Aranda Gómez, 1978; Rubin and Kyle, 1988). Rubin and Kyle (1988) propose that the main veins at San Martin formed late in the evolution of the magmatic-hydrothermal system because they cut structures that predate the granitic intrusion and extend slightly into the intrusive rocks. Although Graf (1997) interprets the veins and fractures peripheral to the Cerro de la Gloria stock at San Martin as radial and concentric features associated with the emplacement of the stock, both the study of Rubin and Kyle (1988), and the maps of major veins and fractures in Graf (1997 – see Figure 2) show them to be preferentially oriented between 060° and 120°. Consequently, the D₅ fractures at Cerro Sacrificio are analogous to these veins at San Martin in terms of their orientation, temporal relationship to the intrusions, and role as mineralizing fluid conduits.

Charcas

The Charcas district is located in San Luis Potosi state, approximately 110 km north of San Luis Potosi city along the eastern margins of the Mexican Altiplano (Fig. 1). Base metal mineralization in the Charcas district is hosted within several veins and associated manto deposits. Past production of 35 Mt and reserves of over 12 Mt at average grades of 4.5% Zn, 0.32% Pb, 0.26% Cu,

and 67 g/t Ag (Megaw, 1999) make this district a significant past and present producer.

The 46.6 ± 1.6 Ma (dated by K-Ar methods) El Temeroso quartz latite porphyry is the main intrusive body in the Charcas district (Castañeda, 1991). It has controlled the localization of mineralization in the area by producing steeply-dipping, east-striking fractures that have been subsequently mineralized (Castañeda, 1991). The porphyry is strongly elongated in plan-view, which suggests that a differential stress field was active during emplacement (Tosdal and Richards, 2001).

Mineralization is hosted within Cretaceous argillaceous limestone of the Taraises and Cupido formations, which was strongly folded prior to mineralization during Mexican fold-and-thrust belt deformation. The dominant structural feature of the region is a large, overturned, north-trending, anticline. It is on the eastern flank of this structure where the ore bodies are located (Castañeda, 1991).

Mantos are the most important style of mineralization at Charcas in a commercial sense. Mineralogically, they are very similar to mineralized veins, to which they are “connected” at some localities (e.g., Castañeda, 1991). The mantos are interpreted to have formed where the ascending metalliferous fluids, channeled along fractures, encountered chemically receptive host rocks (Castañeda, 1991). This channelization of metalliferous fluids by intrusion-related fractures which post-date northwest trending regional structures is similar to the proposed mineralization model at Cerro el Sacrificio. D₅ fractures, like the

intrusion-related fractures at Charcas, functioned as conduits for mineralizing fluids.

La Colorada – Chalchihuites District

The La Colorada deposit is located approximately 50 km south of Cerro el Sacrificio (Fig. 1) and may represent the exposed upper level of a mineralized skarn system like that at Sacrificio and San Martin. Historically, veins striking east to northeast have comprised the main style of mineralization exploited (Albinson, 1988). However, recent exploration activity has delineated base metal-rich chimneys and mantos below the mined veins, and several deeper exploration drillholes have intersected calc-silicate skarn and associated sulfide mineralization (Moore, 1999). The deeper skarn and chimney-manto mineralization is hosted by folded Cuesta del Cura and Indidura Formation limestone. Mineralization is interpreted to be 30 to 35 Ma old from cross cutting relationships with the overlying volcanic strata (Albinson, 1988).

Structural similarities between the La Colorada and Sacrificio deposits include the orientations of mineralized veins and pre-intrusion regional folds at La Colorada (Moore, 1999). These features are analogous to the D₅ fractures and the pre-intrusion D₃ folds at Sacrificio.

Conclusions

The Sacrificio deposit is a copper exoskarn hosted by mid-Cretaceous limestone, chert, and minor shale of the Cuesta del Cura and Indidura formations. Skarn formation and sulfide mineralization are related to a Middle Eocene (40.1 ± 0.5 Ma) granite intrusive complex that underlies most of Cerro el Sacrificio. An older, mid-Cretaceous (109.1 ± 0.4 Ma) granodiorite-quartz monzonite intrusive suite is also present, but field relations indicate that it is unrelated to skarn or mineralization.

Sulfide mineralization at the Sacrificio deposit is classified, from youngest to oldest, as (1) disseminated Cu-Ag, (2) fracture-controlled Cu-Ag \pm Au and, (3) manto-style Zn-Cu-Pb-Ag-Au. The disseminated mineralization is intimately associated with prograde garnet skarn, whereas the polymetallic mantos are associated with the development of late, retrograde, amphibole skarn.

Detailed field studies demonstrate the importance of structural fabrics in localizing skarn and related Cu (Zn-Pb-Ag-Au) sulfide mineralization at the Sacrificio deposit. This differs from many other skarn deposits where lithological controls are as at least as important in controlling the distribution of mineralization (e.g., Santa Eulalia, Hewitt, 1968; Cantung, Dick and Hodgson, 1982; Bingham and Ely, Einaudi, 1982). Three episodes of pre-intrusion regional deformation are recognized at the Sacrificio deposit. D_1 and D_3 record strong east-northeast shortening associated with the Mexican fold-and-thrust belt whereas D_2 shows a minor re-orientation of shortening directions to produce rare east-trending folds. Two episodes of intrusion-related deformation post-date

regional deformation and are synchronous with the mineralization event. D_4 is the formation of a broad dome above the Sacrificio intrusion and D_5 is the opening of extensional fractures and veins above and peripheral to this intrusion.

Distribution of garnet skarn along D_3 fold axial traces indicates that skarn-forming fluids were preferentially channeled along axial surfaces of large amplitude D_3 folds. Later mineralizing fluids were focussed dominantly by D_5 fractures (but some migration along D_3 is possible as well) with bornite \pm chalcopyrite precipitating where fluids infiltrated porous garnet skarn. Thus, intersections between late-stage, intrusion-related, fractures and permeable lithologies (i.e., garnet skarn along D_3) are the most favorable sites for localization of Cu-Ag \pm Au mineralization on Cerro el Sacrificio. The exact mechanism(s) controlling the location of mantos in the Sacrificio skarn system is poorly understood at this time. Their association with retrograde skarn that replaces both mineralized and unmineralized prograde skarn is consistent, however, with the channeling of late retrograde fluids back into the central portions of the ore system using earlier formed D_3 and D_5 structures.

A review of mid-Tertiary skarn and carbonate-replacement deposits occurring in the Mexican Altiplano reveals that skarn and skarn-related mineralization generally does not exhibit simple concentric zonation patterns. Rather, deposits such as San Martín, La Colorada, and Charcas all exhibit major, syn-intrusive, approximately east-striking veins and/or fractures which, by analogy with the Sacrificio skarn system, are interpreted to have channeled the mineralizing fluids and localized the ore bodies. Thus, there appears to be ample

evidence that the structural model developed for the Sacrificio deposit could be successfully applied to other skarn deposits or, more importantly, to deposits and prospects which are only partly explored or exposed.

Acknowledgements

This contribution forms part of the senior author's M.Sc. research at the University of British Columbia. Funding has been generously provided by Boliden Limited, NSERC grant 22R80466 to Rowins, a Thomas and Marguerite MacKay memorial scholarship to Patterson, and an SEGF student research grant to Patterson. Logistical and geological support has been provided by Boliden Limited and Luismin S.A. de C.V. In particular, we would like to thank Chris Rockingham of Boliden and David Aguilar, Ricardo Florés, and Florentino Munoz of Luismin for their aid in the development of the ideas presented here. Informal reviews, editing, and discussions with Greg Dipple, Lori Kennedy, Peter Lewis, Stephen Piercey, and Richard Tosdal have greatly improved interpretation of the data and clarity of the presentation.

References

- Albinson, T.F., 1988, Geologic reconstruction of the paleosurface in the Somberete, Colorada, and Fresnillo districts, Zacatecas State, Mexico: ECONOMIC GEOLOGY, v. 83, p.1647-1667.
- Albinson, T.F. and Sanchez, E., 1977, Geologic evaluation of the Sacrificio Prospect, Puanas Municipality, Durango: Minas San Luis, S.A. geologic report, 51 p.
- Aranda Gómez, J.J., 1978, Metamorphism, mineral zoning, and paragenesis in the San Martin mine, Zacatecas, Mexico: Unpublished M.Sc. thesis, Colorado School of Mines, 90 p.
- Barton, M.D., Staude, J-M.G., Zurcher, L., and Megaw, P.K.M., 1995, Porphyry copper and other intrusion-related mineralization in Mexico, *in* Pierce, F.W. and Bolm, J.G., eds., Porphyry copper deposits of the American Cordillera: Arizona Geological Society Digest, v. 20, p. 487-524.
- Bates, R.L., and Jackson, J.A., 1983, Dictionary of Geological Terms, 3rd Edition: American Geological Institute, Doubleday Anchor, New York, 571 p.
- Bowman, J.R., 1998, Basic aspects and applications of phase equilibria in the analysis of metasomatic Ca-Mg-Al-Fe-Si skarns, *in* Lentz, D.R. ed., Mineralized intrusion-related skarn systems: Mineralogical Association of Canada Short course series, v. 26, p. 1-50.
- Campa, M.F., and Coney, P.J., 1983, Tectono-stratigraphic terranes and mineral resource distributions in Mexico: Canadian Journal of Earth Sciences, v. 20, p. 1040-1051.

- Castañeda, A.F., 1991, Economic geology of the Charcas mining district, San Luis Potosi, *in* Salas, G.P., ed., Economic Geology, Mexico: Geological Society of America, Boulder, Colorado, DNAG P-3, p. 279-286.
- Coney, P.J., 1978, Mesozoic-Cenozoic Cordilleran plate tectonics: Geological Society of America Memoir 152, p. 33-50.
- Damon, P.E., Shafiqullah, M., and Clark, K.F., 1981, Age trends of igneous activity in relation to metallogenesis in the southern cordillera: Geological Society of Arizona Digest, v. 14, p. 137-154.
- Damon, P.E., Shafiqullah, M., and Clark, K.F., 1983, Geochronology of the porphyry copper deposits and related mineralization of Mexico: Canadian Journal of Earth Sciences, v. 20, p. 1052-1071.
- de Cserna, Z., 1989, An outline of the Geology of Mexico, *in* Bally, A. W., and Palmer, A. R., eds., The Geology of North America – An overview: Boulder, Colorado, Geological Society of America, The Geology of North America, v. A.
- Dick, L.A., and Hodgson, C.J., 1982, The Mactung W-Cu (-Zn) contact metasomatic and related deposits of the northeastern Canadian Cordillera: Economic Geology, v. 77, p. 845-867.
- Drewes, H., 1991, Description and Development of the Cordilleran Orogenic Belt in the Southwestern United States and Northern Mexico: U.S. Geological Survey Professional Paper 1512, 87 p.

- Einaudi, M.T., 1982, Skarns associated with porphyry copper plutons.1.
Description of deposits, southwestern U.S., *In* S.R. Titley, ed., Advances
in the geology of the porphyry copper deposits, southwestern United
States: Tucson, University of Arizona Press, p. 185-210.
- Einaudi, M.T., Meinert, L.D., and Newberry, R.J., 1981, Skarn Deposits, *in*
Skinner, B.J., ed., Economic Geology 75th Anniversary Volume: Economic
Geology Publishing Company, El Paso, Texas, p. 317-391.
- Einaudi, M.T., and Burt, D.M., 1982, Terminology, classification, and composition
of skarn deposits: ECONOMIC GEOLOGY, v. 77, p.745-754.
- Gilmer, A. L., Clark, K. F., Conde, J., Hernandez, I., Figueroa, S., and Porter,
E.W., 1988, Sierra de Santa Maria, Velardena Mining District, Durango,
Mexico: ECONOMIC GEOLOGY, v. 83, p. 1802-1855.
- Graf, A, 1997, Geology and pophyry-style mineralization of the Cerro de la Gloria
stock associated with high-T, carbonate-hosted Zn-Cu-Ag(-Pb) skarn
mineralization, San Martin District, Zacatecas, Mexico: Unpublished
M.Sc. Thesis, University of Arizona, 154 p.
- Henry, C.D., Price, J.G., and James, E.W., 1991, Mid-Cenozoic Stress Evolution
and Magmatism in the Southern Cordillera, Texas and Mexico: Transition
from Continental Arc to Intraplate Extension: Journal of Geophysical
Research, v. 96, no. B8, p. 13,545-13,560.

- Hernandez, C., 1991, Economic geology of the Velardena mining district, Durango, *in* Salas, G.P., ed., Economic Geology, Mexico: Geological Society of America, Boulder, Colorado, DNAG P-3, p. 279-286.
- Hewitt, W.P., 1968, Geology and mineralization of the Main mineral zone of the Santa Eulalia district, Chihuahua, Mexico: American Institute of Mining and Engineering Transactions, v. 240, p. 229-260.
- James, E.W. and Henry, C.D., 1991, Compositional Changes in Trans-Pecos Texas Magmatism Coincident with Cenozoic Stress Realignment: Journal of Geophysical Research, v. 96, no. B8, p. 13,561-13,575.
- Johnson, J.W., and Norton, D., 1985, Theoretical prediction of hydrothermal conditions and chemical equilibria during skarn formation in porphyry copper systems: Econ. Geol., v. 80, p.1797-1823.
- Krogh, T.E., 1982, Improved accuracy of U-Pb zircon ages by the creation of more concordant systems using an air abrasion technique: Geochimica et Cosmochimica Acta, v. 46, p. 637-649.
- Kwak, T.A.P., 1987, W-Sn skarn deposits and related metamorphic skarns and granitoids: Amsterdam, Elsevier Press, 439 p.
- LeMaitre, R.W., 1989, A classification of igneous rocks and glossary of terms: Blackwell, Oxford, 193 p.
- Lentz, D.R., 2000, Mass-balance considerations in mineralized skarn systems: implications for permeability evolution and carbonate mobility: Geocanada 2000, conference proceedings with abstracts, cd-ROM.

- Longoria, J.F., Clowes, D.M., and Monreal, R., 1999, Type Mesozoic succession of northern Mexico: Canon La Casita, *in* Bartolini, C., Wilson, J.L., and Lawton, T.F., eds., Mesozoic sedimentary and Tectonic History of North-Central Mexico: Boulder Colorado, Geological Society of America Special Paper 340, p. 287-318.
- McClay, K.R., 1987, The Mapping of Geological Structures, John Wiley and Sons, West Sussex, England, 161 p.
- McLeroy, D.F., Francisco Franquesa, R., and Saul Romero, M., 1986, Origin of the breccia pipes and mantos of the Ojuela lead-silver district, Mapimi, Durango, *in* Clark, K.F., Megaw, P.K.M., and Ruiz, J. eds., Lead-Zinc-Silver Carbonate-Hosted Deposits of Northern Mexico, Society of Economic Geologists, Guidebook for Field and Mine Excursions, 325 p.
- Megaw, P. K. M., 1998a, Polyphase skarn mineralization associated with a polyphase differentiated composite intrusion, San Martin – Sabinas District, Zacatecas, Mexico, *in* Geological Association of Canada: Mineralogical Association of Canada 1998 Abstract Volume, p. A-122.
- Megaw, P. K. M., 1998b, Carbonate-hosted Pb-Zn-Ag-Cu-Au replacement deposits: An exploration perspective. *in* Lentz, D.R., ed., Mineralized intrusion-related skarn systems: Mineralogical Association of Canada, short course volume 26, p. 337-356.

- Megaw, P.K.M., 1999, The high-temperature, Ag-Pb-Zn-(Cu) carbonate-replacement deposits of central Mexico *in* Jambor, J.L., ed., VMS and carbonate-hosted polymetallic deposits of central Mexico; Cordilleran Roundup, 1999, p. 81-84.
- Megaw, P.K.M., Ruiz, J., and Titley, S.R., 1988, High-temperature, carbonate-hosted Ag-Pb-Zn(Cu) deposits of northern Mexico: *ECONOMIC GEOLOGY*, v.83, p. 1856-1885.
- Meinert, L.D., 1997, Application of skarn zonation models to mineral exploration: *Exploration and Mining Geology*, v. 6, no. 2, p. 185-208.
- Meinert, L.D., 1998, A review of skarns that contain gold, *in* Lentz, D.R. ed., Mineralized intrusion-related skarn systems: Mineralogical Association of Canada Short course series, v. 26, p. 359-414.
- Meinert, L.D., 2000, Gold in skarns related to epizonal intrusions: *Reviews in Economic Geology*, v. 13, p. 347-371.
- Moore, R., 1999, The geology and development of the La Colorada Ag-Pb-Zn deposit, Zacatecas State, Mexico. *in* Jambor, J.L., ed., VMS and carbonate-hosted polymetallic deposits of central Mexico; Cordilleran Roundup, 1999, p. 81-84.
- Mortensen, J.K., Ghosh, D., and Ferri, F., 1995, U-Pb age constraints of intrusive rocks associated with copper-gold porphyry deposits in the Canadian Cordillera, *in* Schroeter, T.G., ed., Porphyry deposits of the northwestern Cordillera of North America: Canadian Institute of Mining and Metallurgy, Special Volume 46.

North, F.K., 1985, Petroleum Geology: Allen and Unwin Inc. Winchester, Mass.

607 p.

Palacios, H.A.M., Querol, F.S., and Lowther, G.K., 1991, Geology and genesis of the Naica mineral deposits, Chihuahua, *in* Salas, G.P., ed., Economic Geology, Mexico: Geological Society of America, Boulder, Colorado, DNAG P-3, p. 279-286.

Roddick, J.C., 1987, Generalized numerical error analysis with application to geochronology and thermodynamics: *Geochimica et Cosmochimica Acta*, v. 51, p. 2129-2135.

Rollinson, H.R., 1993, Using Geochemical Data: evaluation, presentation, Interpretation: Longman Scientific and Technical, John Wiley and Sons, 352 p.

Rowins, S.M., 1998, A review of Cu-Zn skarn and epithermal Au-Ag mineralization at Cerro Sacrificio and a proposed drilling program: Boliden Limited, Unpublished report, 10 p.

Rubin, J.N., 1986, Mineralogy and Ore Genesis at the San Martin Mine, Zacatecas, Mexico: Unpublished M.Sc. Thesis, The University of Texas at Austin, 97 p.

Rubin, J. N. and Kyle, J. R., 1988, Mineralogy and geochemistry of the San Martin skarn deposit, Zacatecas, Mexico: *ECONOMIC GEOLOGY*, v. 83, p. 1782-1801.

- Ruiz, J., Patchett, P.J., and Ortega-Gutierrez, F., 1988, Proterozoic and Phanerozoic basement terranes of Mexico from neodymium isotopic studies: Geological Society of America Bulletin, v. 100, p. 274-281.
- Sawkins, F.J., 1964, Lead-zinc ore deposition in the light of fluid inclusion studies, Providencia mine, Zacatecas, Mexico: ECONOMIC GEOLOGY, v. 59, p. 883-919.
- Sedlock, R. L., Ortega-Gutierrez, F., and Speed, R. C., 1993, Tectonostratigraphic terranes and tectonic evolution of Mexico: Geological Society of America Special Paper 278, 151 p.
- Shoji, T., 1975, Role of temperature and CO₂ pressure in the formation of skarn and its bearing on mineralization: ECONOMIC GEOLOGY, v. 70, p. 739-749.
- Stacey, J.S. and Kramer, J.D., 1975, Approximation of terrestrial lead isotope evolution by a two-stage model: Earth and Planetary Science Letters, v. 26, p. 207-221.
- Steiger, R.H. and Jäger, E., 1977, Subcommittee on geochronology: convention on the use of decay constants in geo- and cosmochemistry: Earth and Planetary Science Letters, v. 36, p. 359-362.
- Sutter, M., 1987, Structural traverse across the Sierra Madre Oriental fold-thrust belt in east-central Mexico: Geological Society of America Bulletin, v. 98, p. 249-264.

- Sun, S.S. and McDonough, W.F., 1989, Chemical and isotopic systematics of ocean basalts; implications for mantle composition and processes *In* Magmatism in the Ocean Basins, Saunders, A.D. and Norry, M.J. eds., Geological Society Special Publication 42, p. 313-345.
- Terry, D.A., Patterson, K.P., Warman, T., and Gibson, K., 1999, Report on diamond drilling, geological mapping, and geophysical surveys carried out on the Cerro Sacrificio project, Durango state, Mexico (November 1998 to July 1999): Boliden Limited, Unpublished report, 49 p.
- Titley, S.R., 1993, Characteristics of high temperature carbonate-hosted massive sulfide ores in the United States, Mexico, and Peru, *in* Kirkham, R.V., Sinclair, W.D., Thorpe, R.I., and Duke, J.M., eds., Mineral deposit modeling: Geological Association of Canada Special Paper 40, p. 585-614.
- Tosdal, R.M. and Richards, J.P., 2001, Magmatic and structural controls on the development of porphyry Cu \pm Mo \pm Au deposits, *in* Richards, J.P. and Tosdal, R.M. eds., Structural controls on ore genesis: Reviews in Economic Geology, v. 14, p. 157-181.

Figure Captions

Figure 1. Location map of the Sacrificio deposit, Durango, Mexico. Solid squares and circles represent major cities and significant mineral deposits in the district, respectively.

Figure 2. Major morphotectonic features and plate-tectonic setting of Mexico (modified after Sedlock *et al.*, 1993). Heavy lines denote plate boundaries, whereas lighter lines mark morphotectonic boundaries. The Trans Mexican Volcanic Belt is abbreviated as TMVB.

Figure 3. Simplified geological map of the Sacrificio property. Heavy dashed line is the approximate subsurface extent of the Sacrificio intrusion inferred from geophysical data (Terry *et al.*, 1999).

Figure 4. Intrusive phases of the mid-Tertiary Coloradito and Sacrificio intrusions (40.1 ± 0.5 Ma) and the mid-Cretaceous Dique Viejo (109.1 ± 0.4 Ma). Solid circles and squares represent the locations of samples collected for whole-rock geochemistry and geochronology, respectively.

Figure 5. Photographs and microphotographs of major intrusive phases from the Sacrificio deposit. A. Slabbed sample of monzonite from Dique Viejo. White phenocrysts are plagioclase and orthoclase. B. Photomicrograph of monzonite from Dique Viejo with phenocrysts of plagioclase (Pl) and orthoclase (Or). C. Slabbed sample of medium-grained biotite granite from the Sacrificio intrusion. Irregular black patches are primary biotite. D. Photomicrograph of medium-grained biotite granite from the Sacrificio intrusion (Qtz = quartz, Or = orthoclase). E. Slabbed sample of granite from the Coloradito intrusion. Grey,

subrounded phenocrysts are quartz. F. Photomicrograph of granite from the Coloradito intrusion with phenocrysts of quartz (Qtz) and plagioclase (Pl). G. Slabbed sample of biotite-rich granite from the Coloradito intrusion. H. Photomicrograph of biotite-rich granite from the Coloradito intrusion with phenocrysts of quartz (Qtz), plagioclase (Pl) and biotite (Bt).

Figure 6. Whole-rock compositions of intrusive rocks from Cerro el Sacrificio cast in terms of quartz, alkali feldspar, and plagioclase (method of classification after LeMaitre, 1989). The Middle Eocene intrusive suite clusters in the granite field, whereas the mid-Cretaceous dykes lie in the granodiorite and quartz-monzonite fields. Note that the prefix "kp" has been omitted from data labels. Sample locations are shown in Figure 4.

Figure 7. Primitive mantle-normalized rare earth element abundances of intrusive rocks from the Sacrificio deposit. Mantle normalization factors are those of Sun and McDonough (1989). A. Mid-Cretaceous intrusive rocks including Dique Viejo and several smaller dykes exposed on Cerro Coloradito. B. Middle Eocene intrusive rocks from the Sacrificio and Coloradito intrusions. Note the change in vertical scale between A and B. Complete chemical analyses of samples shown here are given in Table 1. Sample locations are shown in Figure 4.

Figure 8. Uranium-lead concordia plots of dated intrusive rocks. A. Porphyritic granite from the core of the Coloradito intrusion. B. Porphyritic granite from a large dike exposed on Cerro Coloradito. C. Medium-grained

biotite-granite from the Sacrificio intrusion. D. Porphyritic monzodiorite from Dique Viejo. All sample locations shown in Figure 4.

Figure 9. Structural geology map of Cerro el Sacrificio including selected bedding, fold axis (D_1 and D_3), and fracture measurements. Plunges of fold axes define D_4 doming of sedimentary strata over the Sacrificio intrusion. Areas A, B, and C correspond to areas represented by stereonet projections of all data in Figure 10.

Figure 10. Equal-area stereonet projections of all structural data collected at Cerro el Sacrificio. Poles to bedding are contoured with mean girdles added. Open circles represent measured D_1 and D_3 fold axes; open squares represent poles to D_5 fractures. The northerly plunge of fold axes in area B, and the southerly plunge of fold axes in area C, define the doming of sedimentary strata over the Sacrificio intrusion. The relative consistency of fracture orientations in the northern (Area B) and southern (Area C) areas compared with the pronounced doming of bedding and fold axes demonstrates that the fracturing event (D_5) post-dated the doming event.

Figure 11. Surface distribution of skarn alteration and sulfide mineralization on Cerro el Sacrificio. Garnet skarn and disseminated bornite-chalcopyrite mineralization are strongly controlled by D_3 fold axial surfaces and their intersections with major and minor D_5 fracture sets. Only the major fracture sets and fold axial traces are shown here. Note the localization of most skarn alteration and mineralization above the intrusion rather than around the margins as is typical of many skarn deposits.

Figure 12. A. Photomicrograph of garnet skarn with bornite (Bn) and chalcopyrite (Ccp) filling intermineral porosity created by the formation of garnet (Grt). This texture is typical of disseminated bornite-chalcopyrite mineralization. B. Typical east-northeast-striking mineralized vein (filled D₅ fracture) which has been extensively mined at Sunlight Shaft. Dashed line delineates the boundary between the vein and disseminated sulfide mineralization in garnet skarn. C. D₅ vein with crustified bands of coarse-grained quartz and calcite. Fibrous growth of quartz and calcite perpendicular to vein walls is indicative of pure extension (mode 1). Pen is 15 cm in length. D. Margin of typical polymetallic manto replacing marble in drillcore. Manto is composed mainly of fine-grained pyrite, arsenopyrite, sphalerite, galena, pyrrhotite and chalcopyrite (see text for further description of the mineralogy).

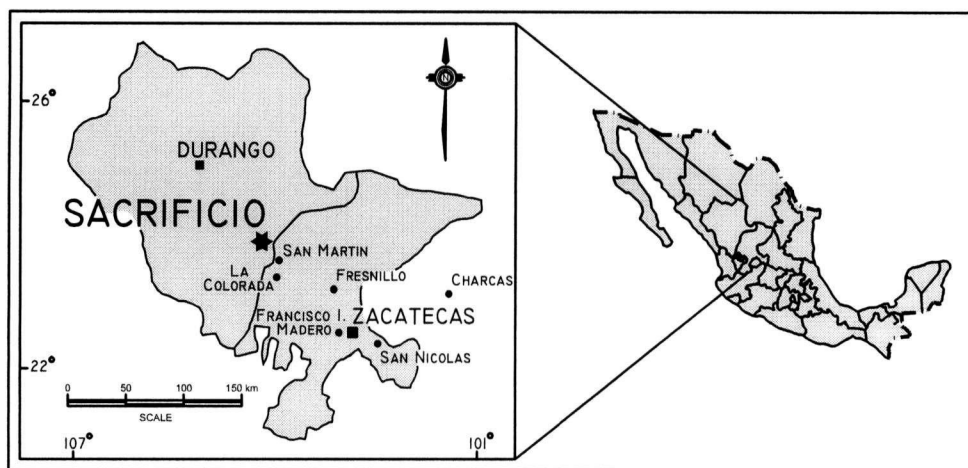
Figure 13. Interpreted sequence of deformation events affecting Cerro el Sacrificio. D₁ – Tight to isoclinal, west-verging, inclined folds. D₂ – Type 2 refolding of D₁ folds. D₃ – Large amplitude, gentle to open, upright folds trending 330° that refold D₁ and D₂ folds. D₄ – Doming of previously deformed strata over the intrusion during its emplacement, with exsolved magmatic fluids focussed along D₃ axial surfaces. D₅ – Increase in pore fluid pressure above the intrusion and opening of mode 1 fractures oriented east-northeast, parallel to maximum compressive stress. Mineralizing fluids are channeled by these fractures, with bornite and chalcopyrite filling secondary porosity in garnet skarn proximal to the D₅ fractures. Retrograde skarn and manto formation, which postdate D₅, are not included in this schematic diagram.

Figure 14. Relative timing of deformation, alteration, and mineralization events at the Sacrificio deposit. Absolute ages are derived from U-Pb dating of intrusive rocks; all other timing is relative (i.e., the time axis is not to scale).

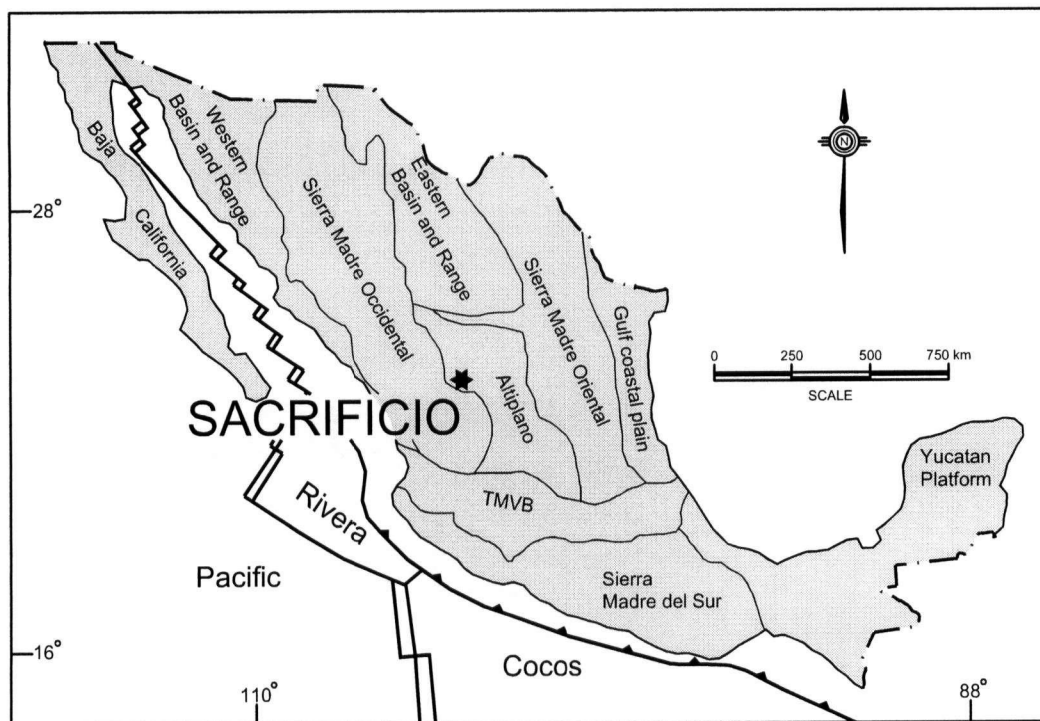
Figure 15. Photographs of key structural features mapped at Cerro el Sacrificio. Fold axial surfaces are highlighted by dashed white lines. A. Mesoscopic D_1 folds. Hammer is 30 cm in length. B. D_2 folds refolding D_1 folds. C. Broad, open D_3 fold. D. Typical, steeply-dipping D_5 fractures with associated Cu-Ag \pm Au mineralization.

Figure 16. Whole-rock compositions (classification scheme after LeMaitre, 1989) of intrusive phases from the Cerro de la Gloria Stock, San Martin mine (data from Graf, 1997). San Martin data are represented by black squares. Shaded field represents the compositional range of intrusive rocks from the Sacrificio deposit (data from Fig. 6).

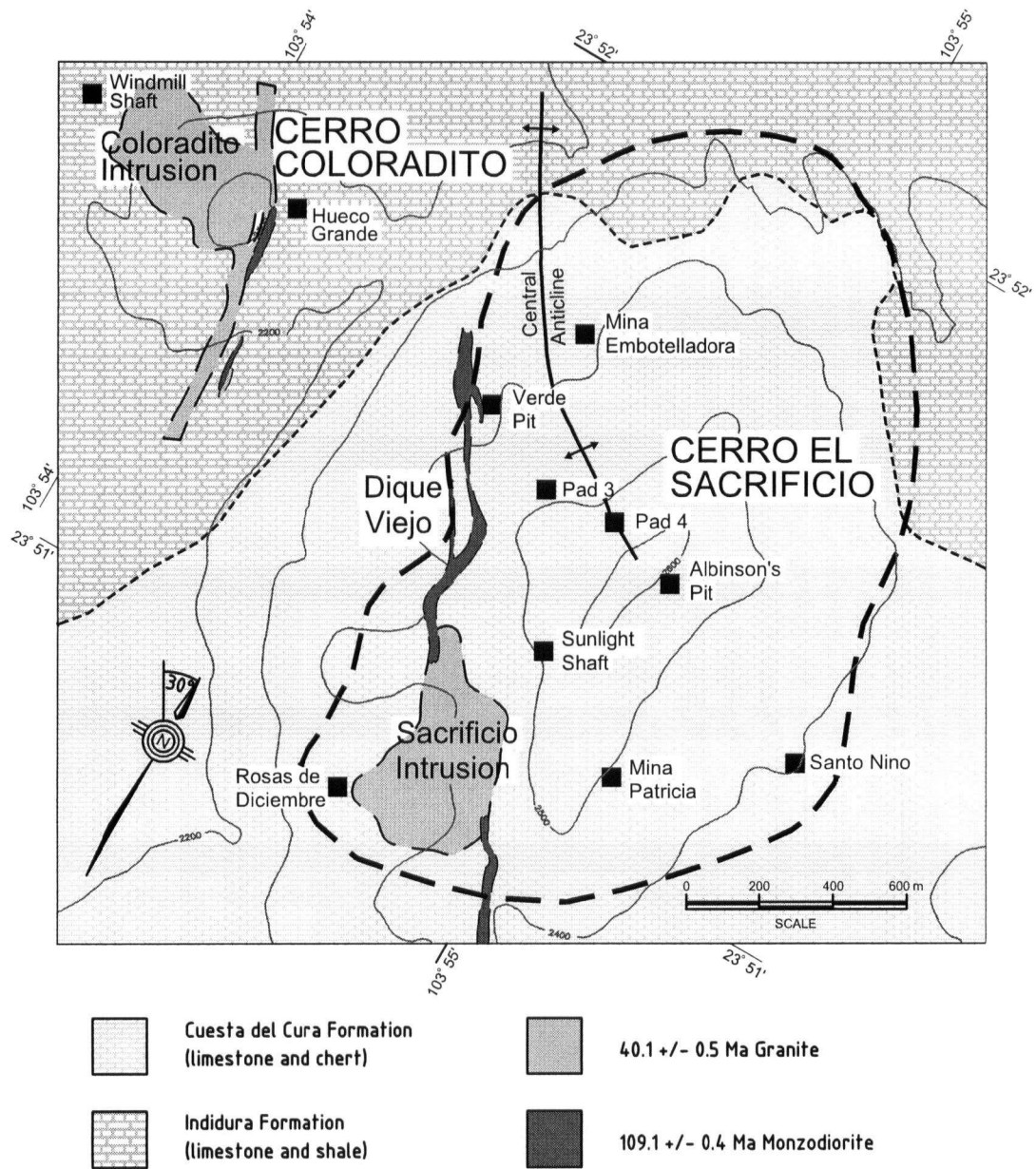
Figure 17. Primitive mantle-normalized rare earth element abundances of intrusive rocks from the Cerro de la Gloria Stock, San Martin (data from Graf, 1997). Range of rare earth element abundances for intrusive rocks from the Sacrificio deposit are represented by the shaded area (data from Fig. 7).



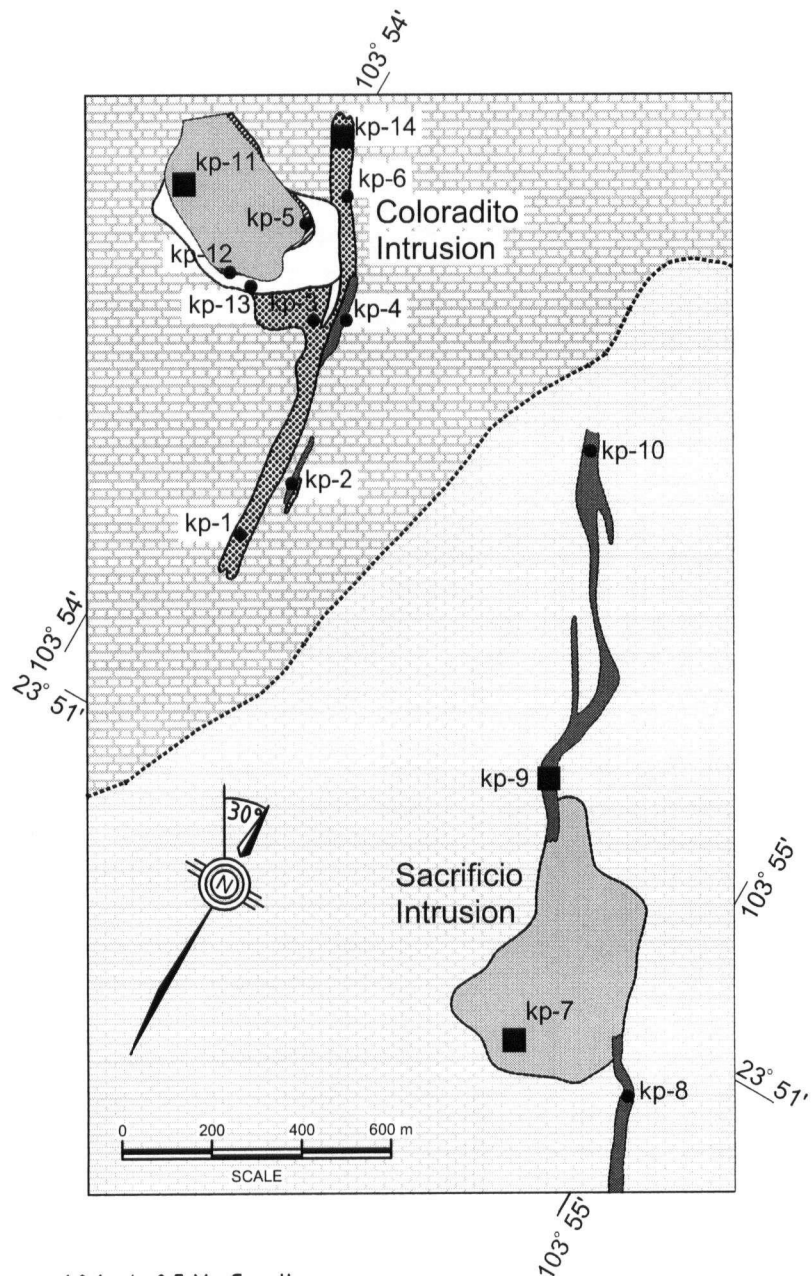
Patterson et al.: Figure 1



Patterson et al.: Figure 2



Patterson et al.: Figure 3



40.1 +/- 0.5 Ma Granite

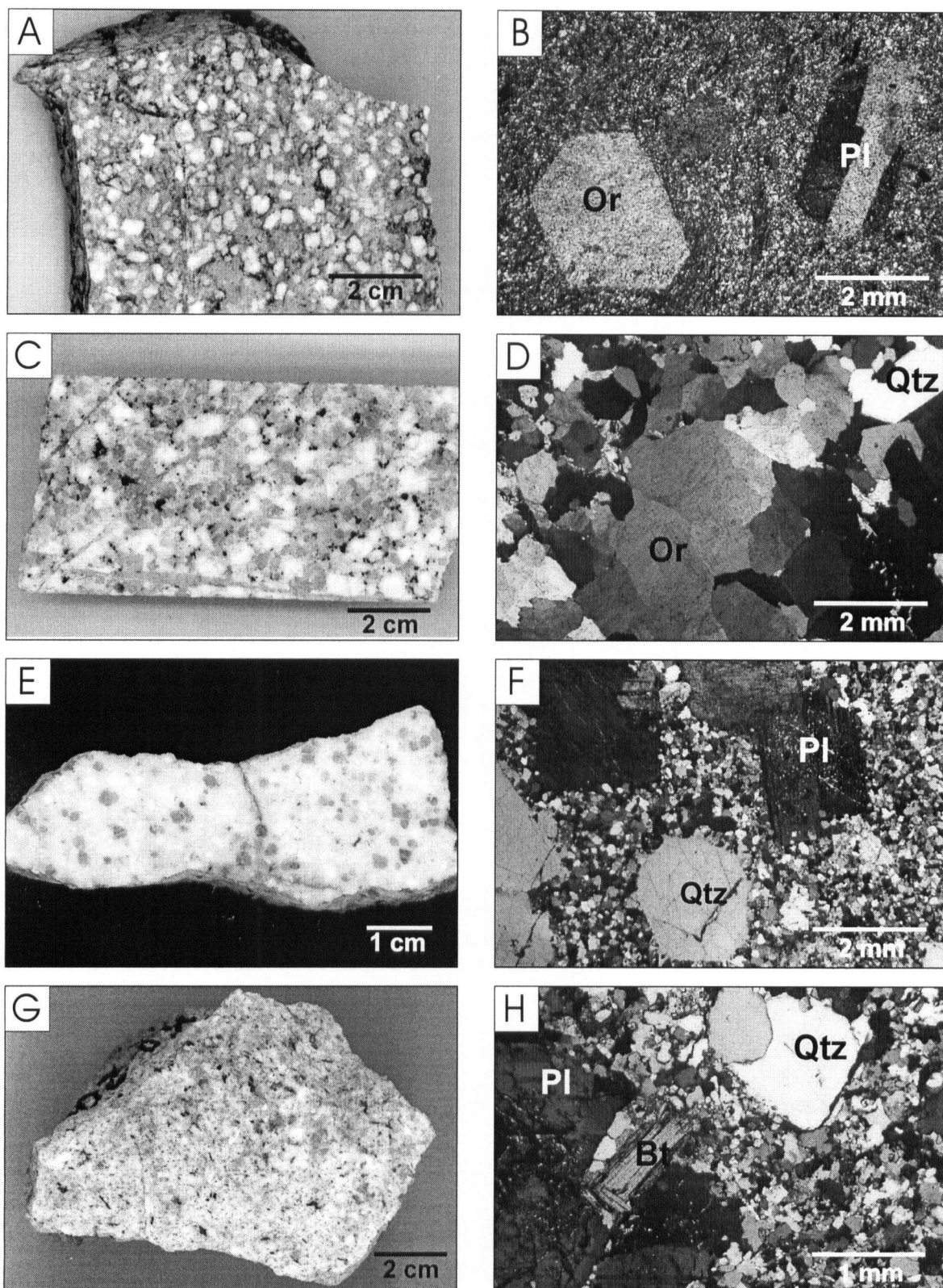
- Quartz-Feldspar-Phyric Granite
- Quartz-Feldspar-Biotite-Phyric Granite
- Quartz-Phyric Granite
- Zones of Intense Silicification

- Cuesta del Cura Formation (limestone and chert)
- Indidura Formation (limestone and shale)

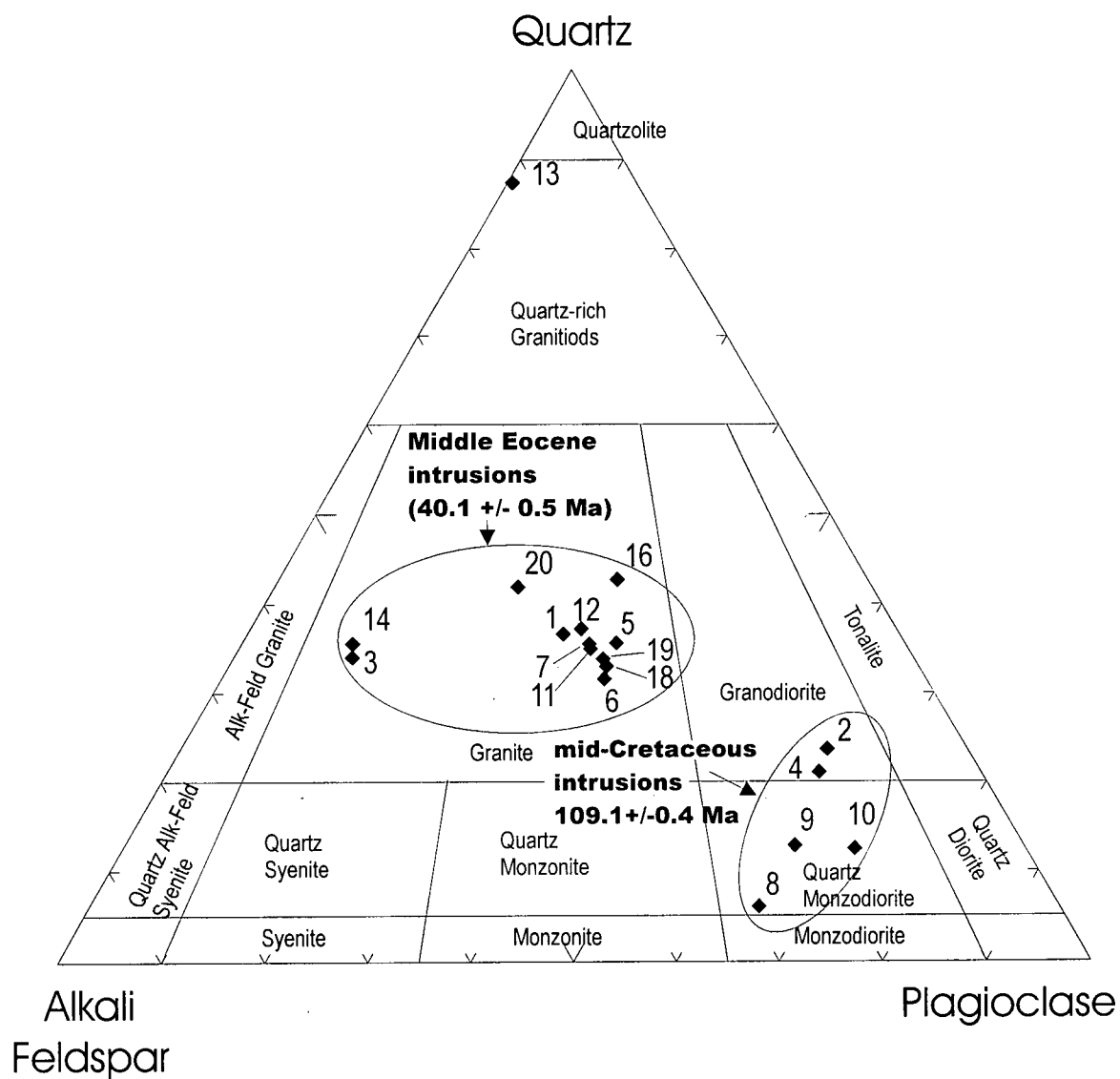
109.1 +/- 0.4 Ma Monzodiorite

- Feldspar-Phyric Monzodiorite

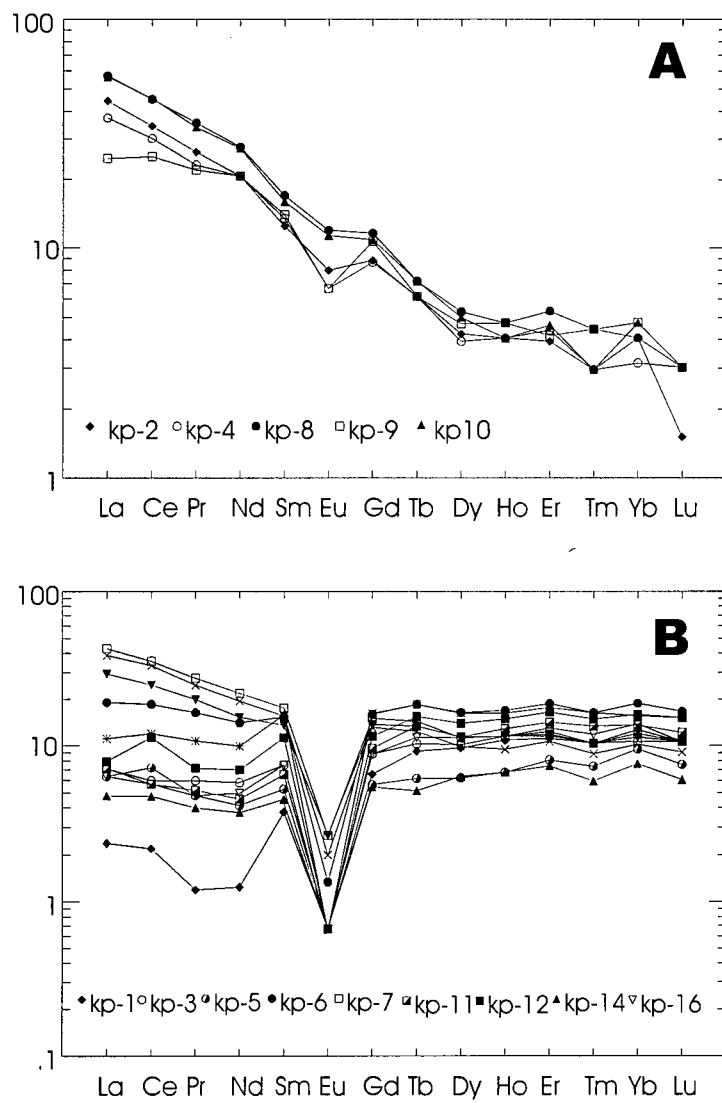
Patterson et al.: Figure 4



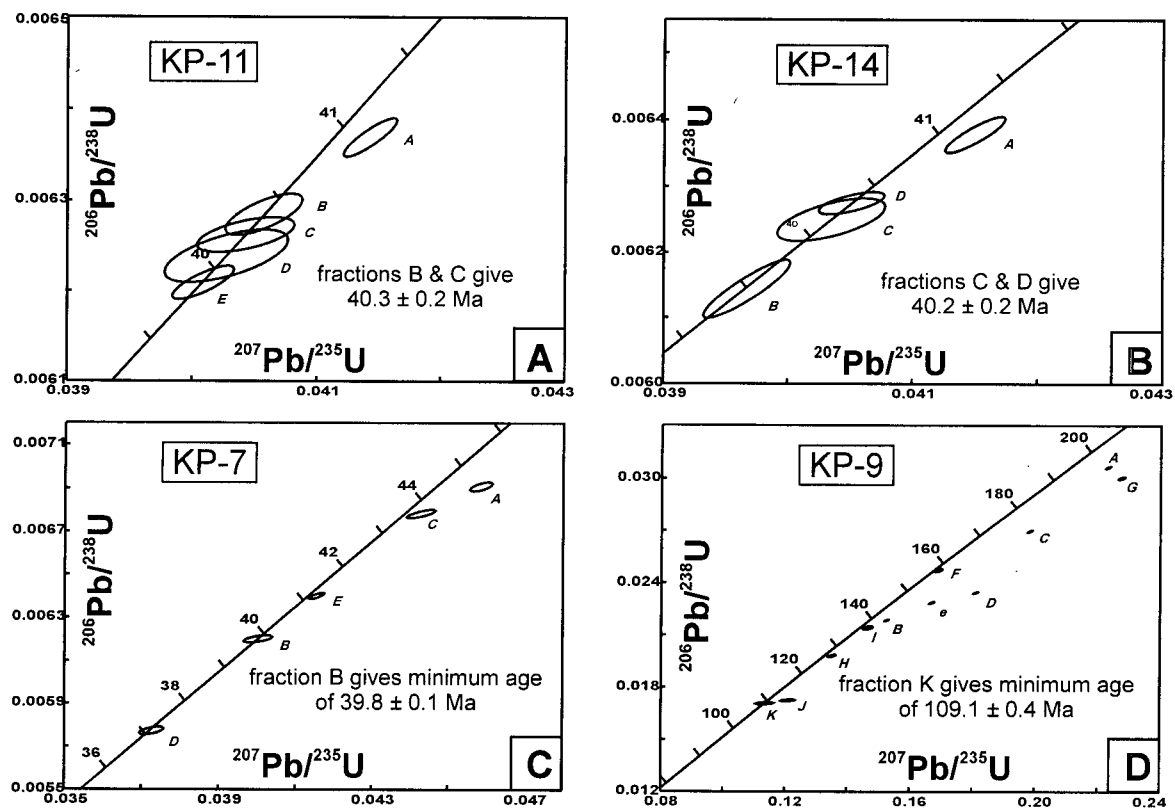
Patterson et al.: Figure 5



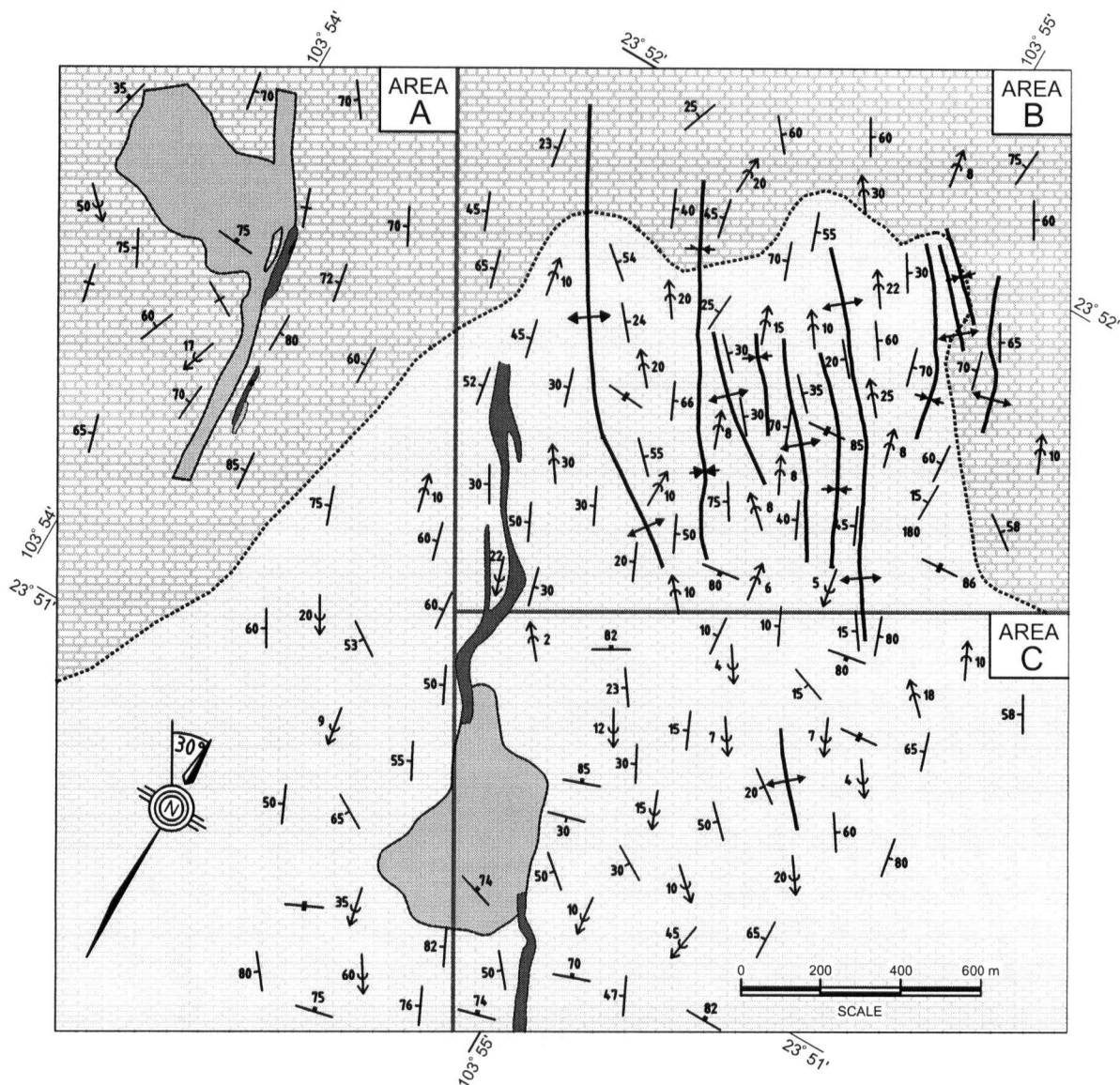
Patterson et al.: Figure 6









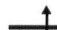

Patterson et al.: Figure 7



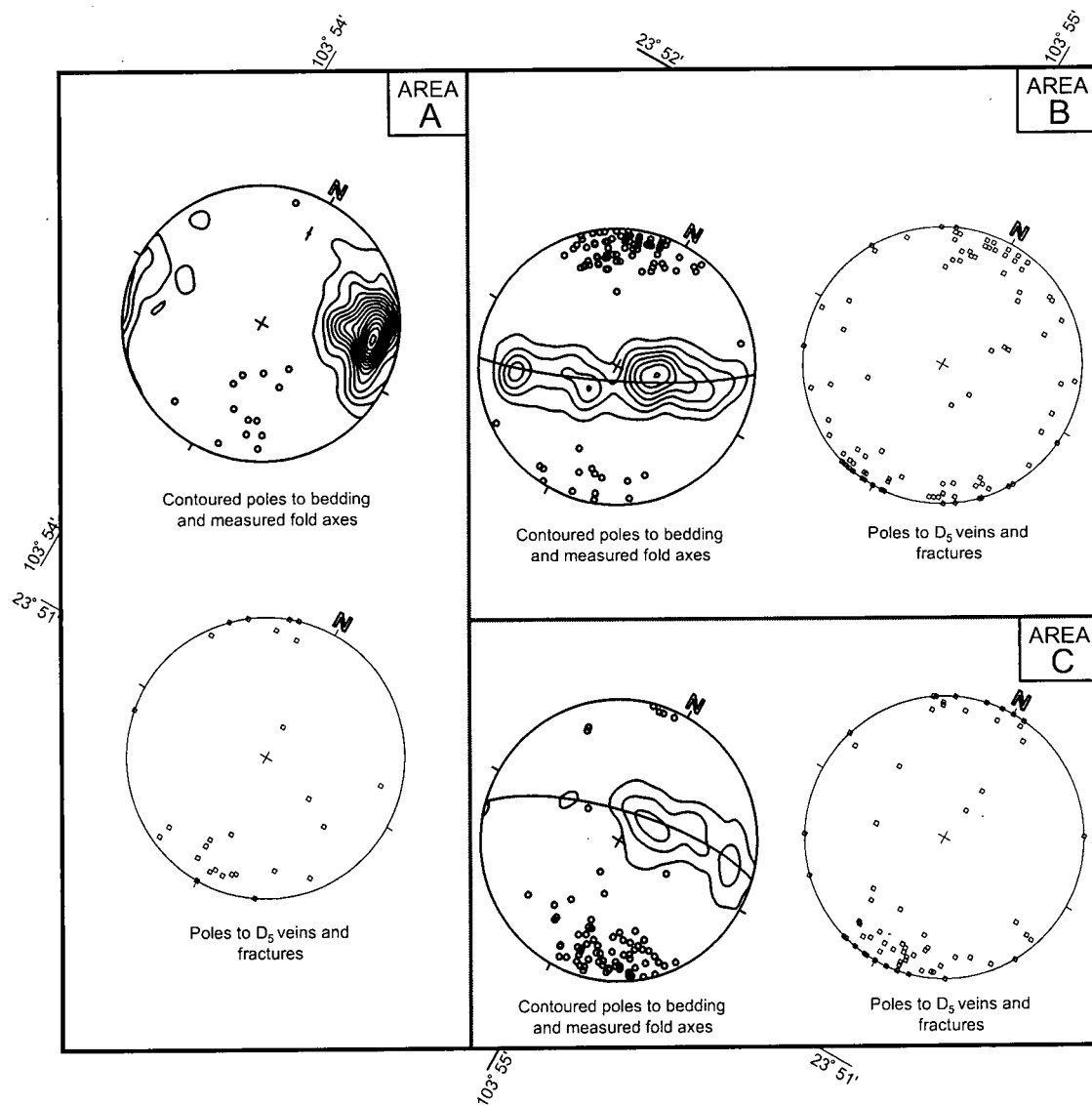
Patterson et al., Figure 8



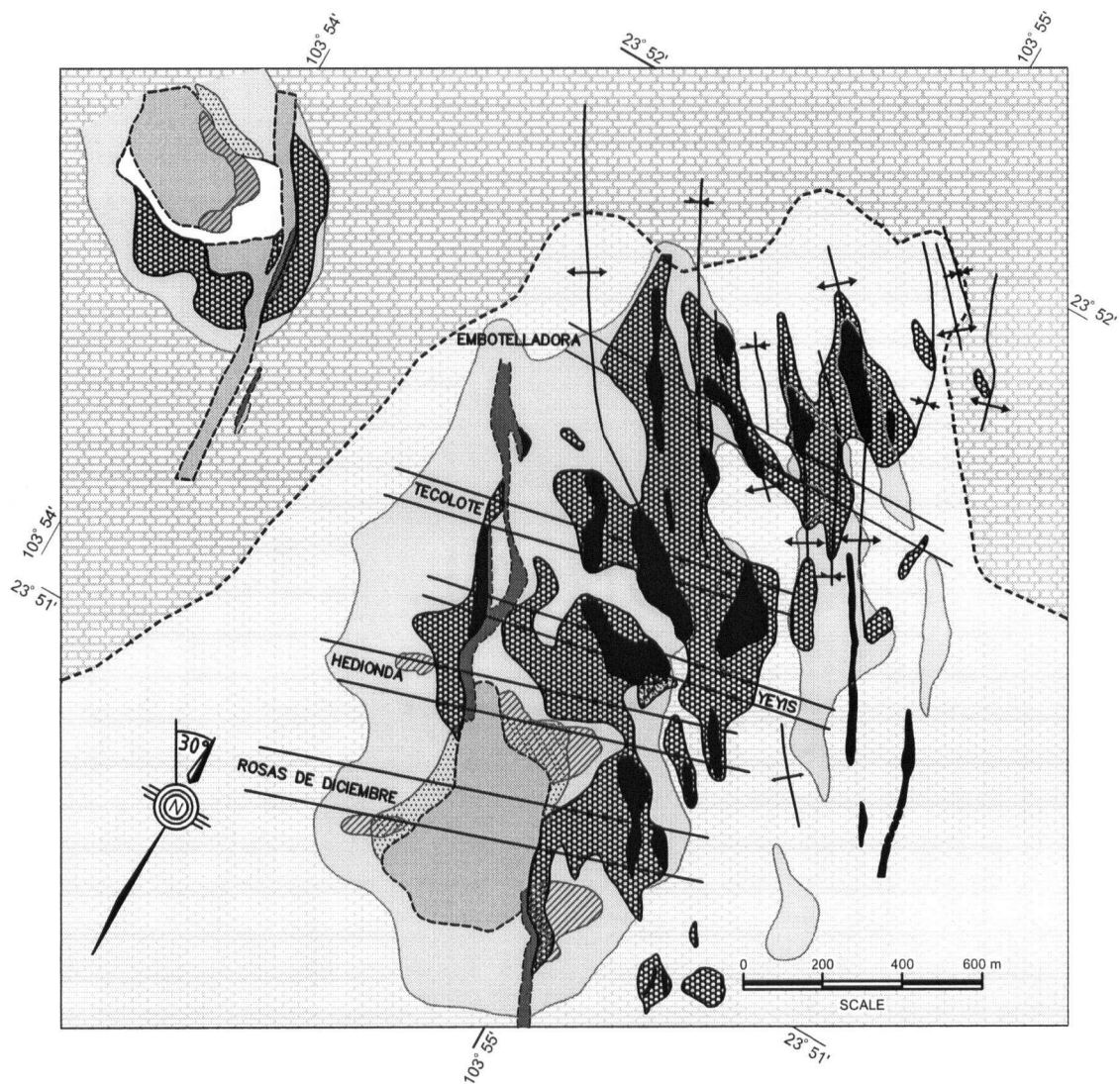
-  Cuesta del Cura Formation (limestone and chert)
-  Indidura Formation (limestone and shale)
-  40.1 +/- 0.5 Ma Granite
-  109.1 +/- 0.4 Ma Monzodiorite

-  Bedding Orientation
-  Measured Fold Axis
-  Fracture Orientation
-  Fold Axial Trace, Antiform
-  Fold Axial Trace, Synform

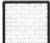





Patterson et al.: Figure 9



Patterson et al.: Figure 10



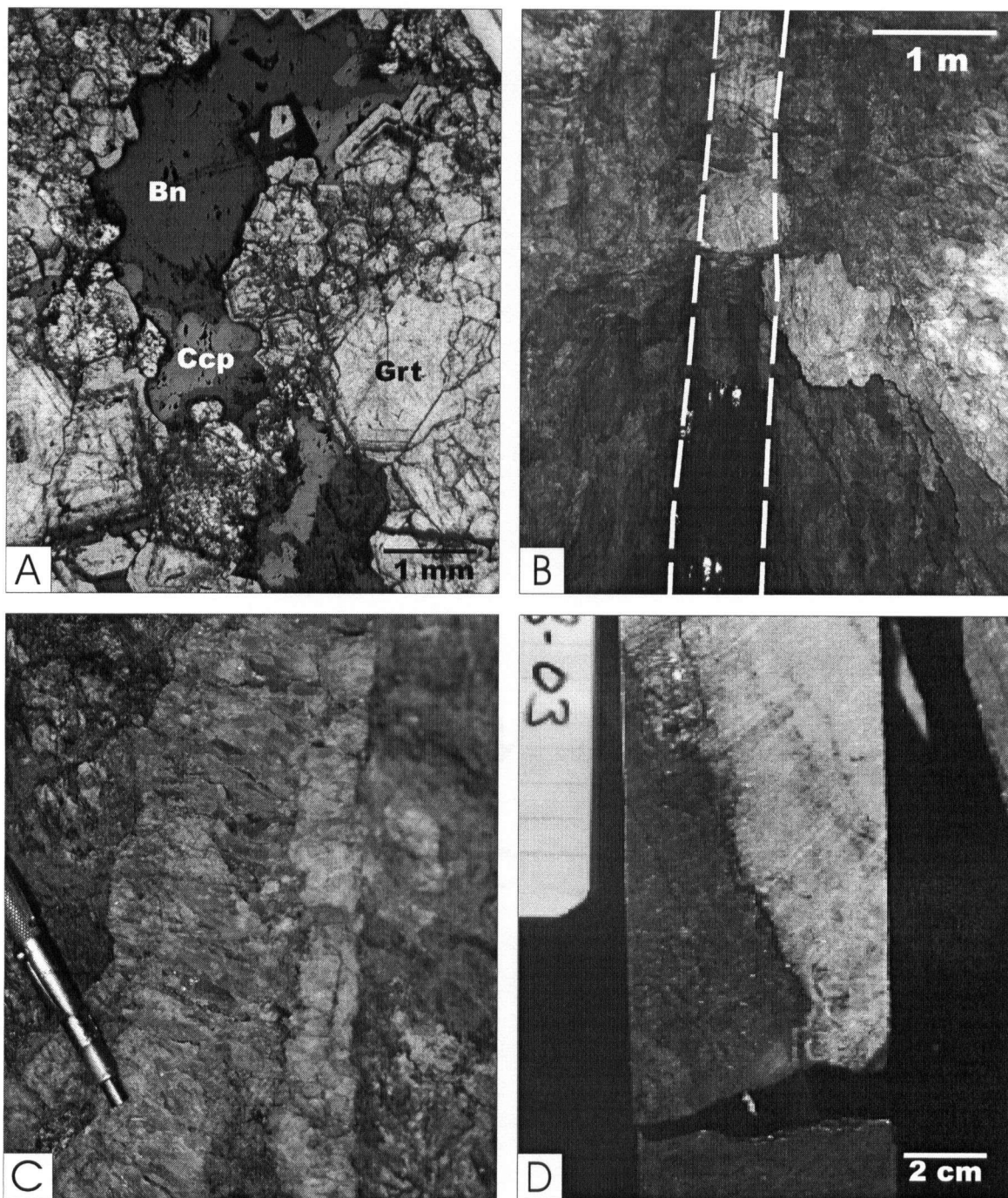
Lithologic Units

-  Cuesta del Cura Formation (limestone and chert)
-  Indidura Formation (limestone and shale)
-  40.1 +/- 0.5 Ma Granite
-  109 Ma Monzoniorite
-  Approximate boundary of mineralized fracture set
-  Mapped contact between the Cuesta del Cura and Indidura Formations

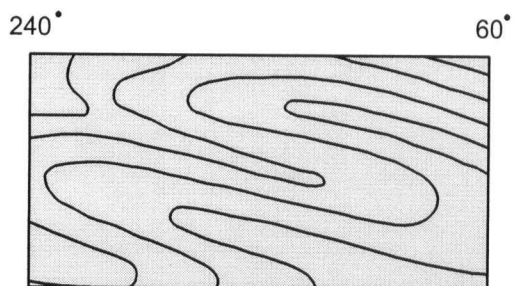
Alteration and Related Mineralization

- Hornfels**
 -  Quartz-Scapolite-Albite +/- Sericite
- Prograde Skarn**
 -  Garnet Skarn
 -  Disseminated Bornite-Chalcopyrite and Fracture-Controlled Mineralization
 -  Intense Silicification
 -  Quartz Vein Stockwork
 -  Quartz-Cemented Limestone Breccia
- Retrograde Skarn**
 -  Pervasive Amphibole-Chlorite +/- Base and Precious Metal Mantos

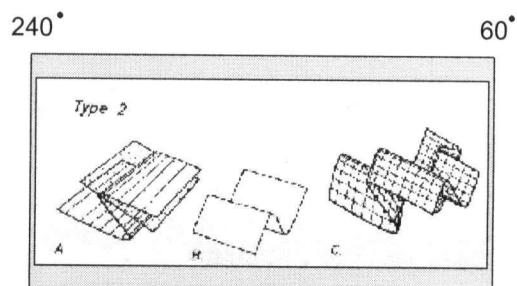
Patterson et al.: Figure 11



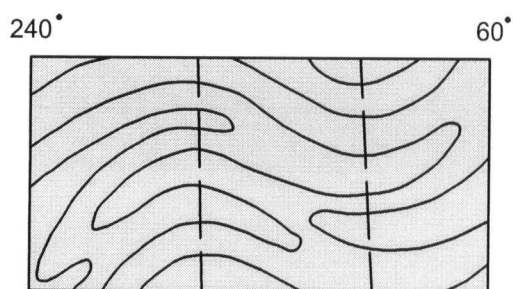
Patterson et al.: Figure 12



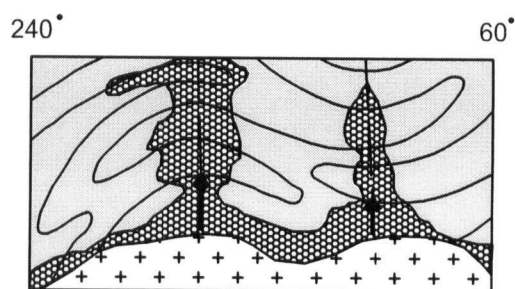
D1



D2

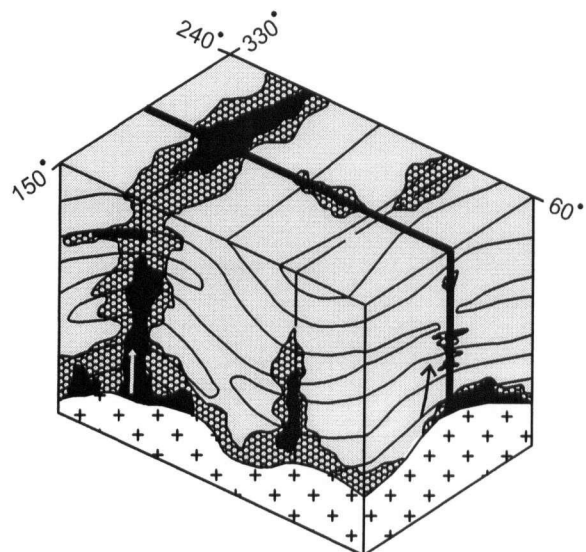


D3



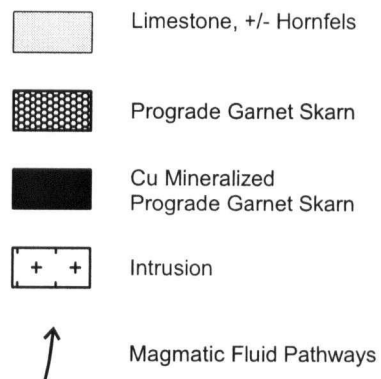
Intrusion, doming over pluton,
and garnet skarn

D4

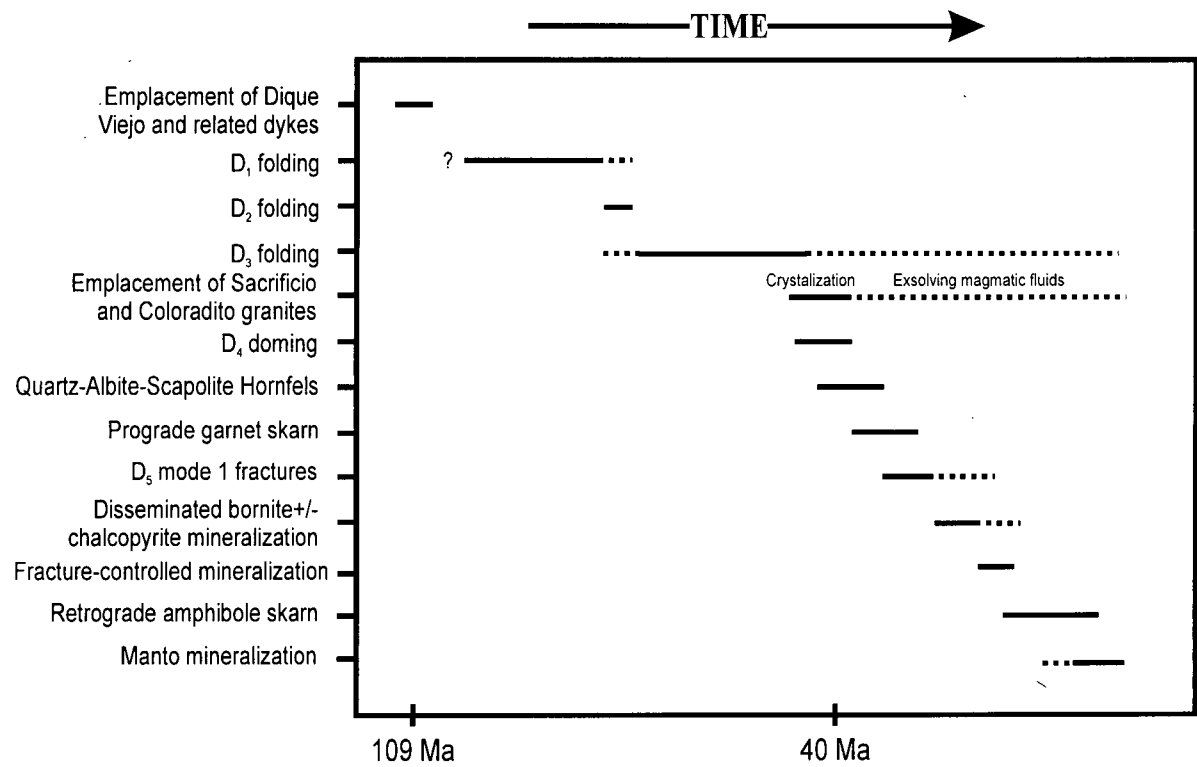


Opening of extensional fractures,
fluids channeled up fractures

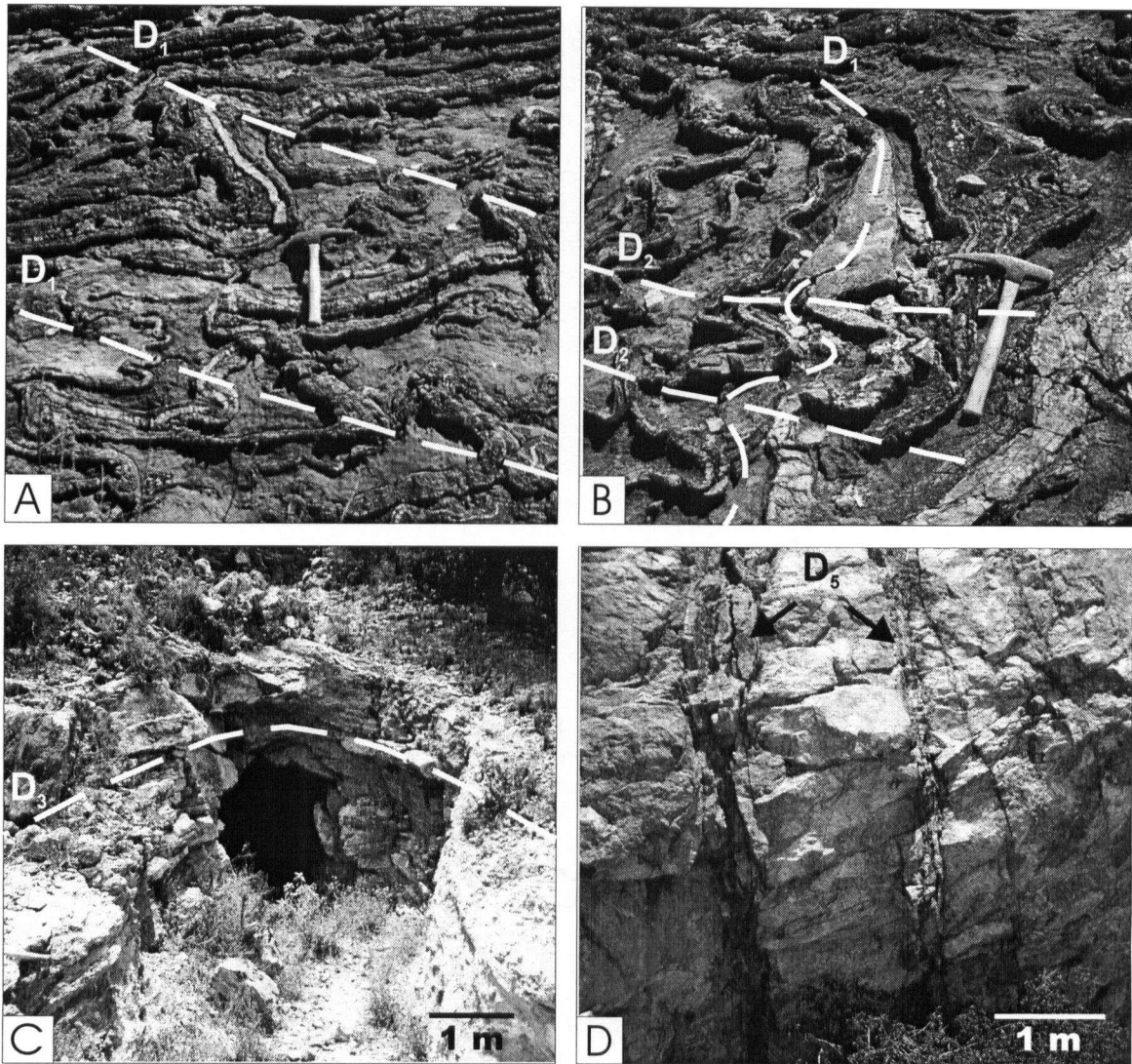
D5



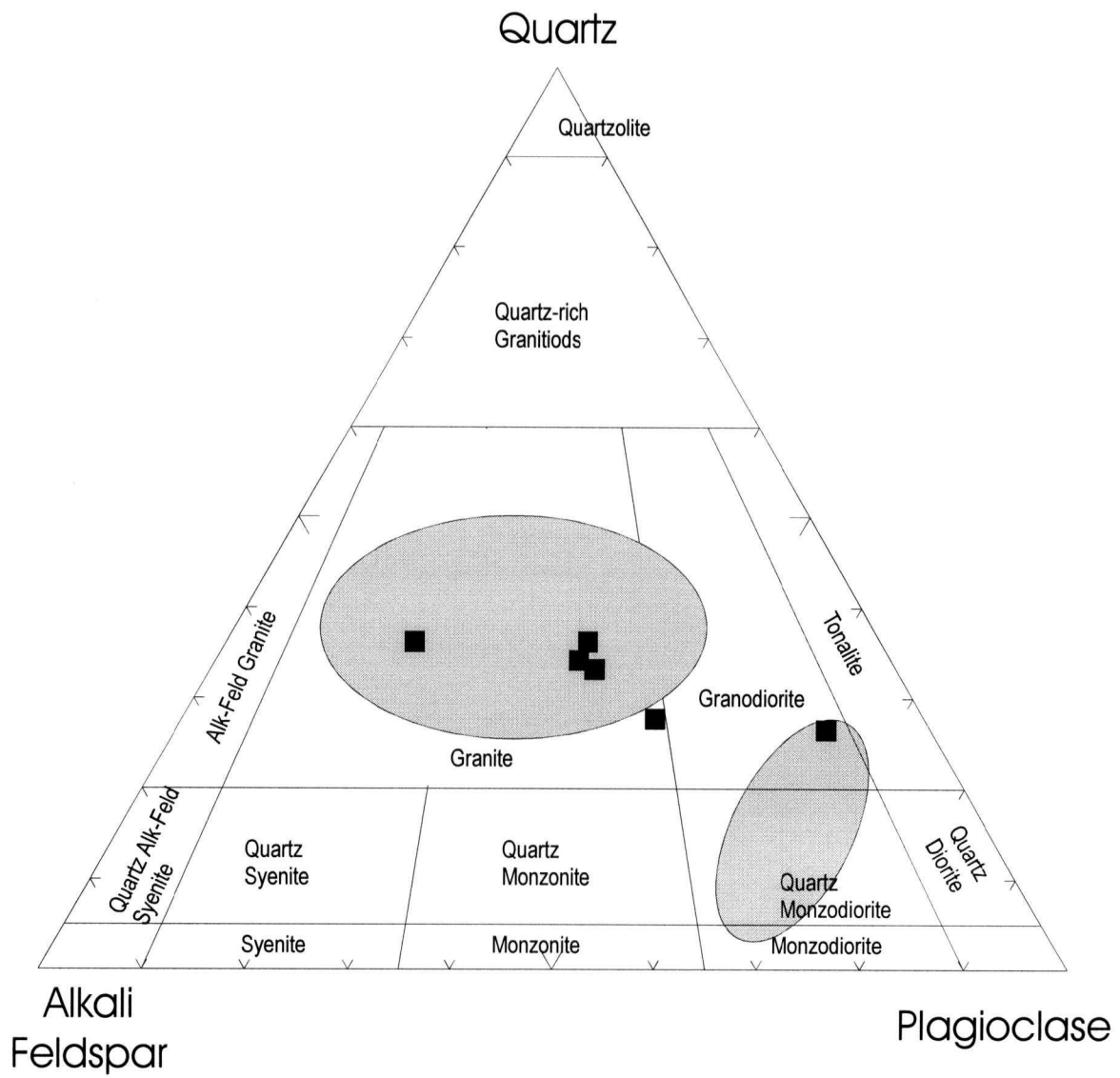
Patterson et al.: Figure 13



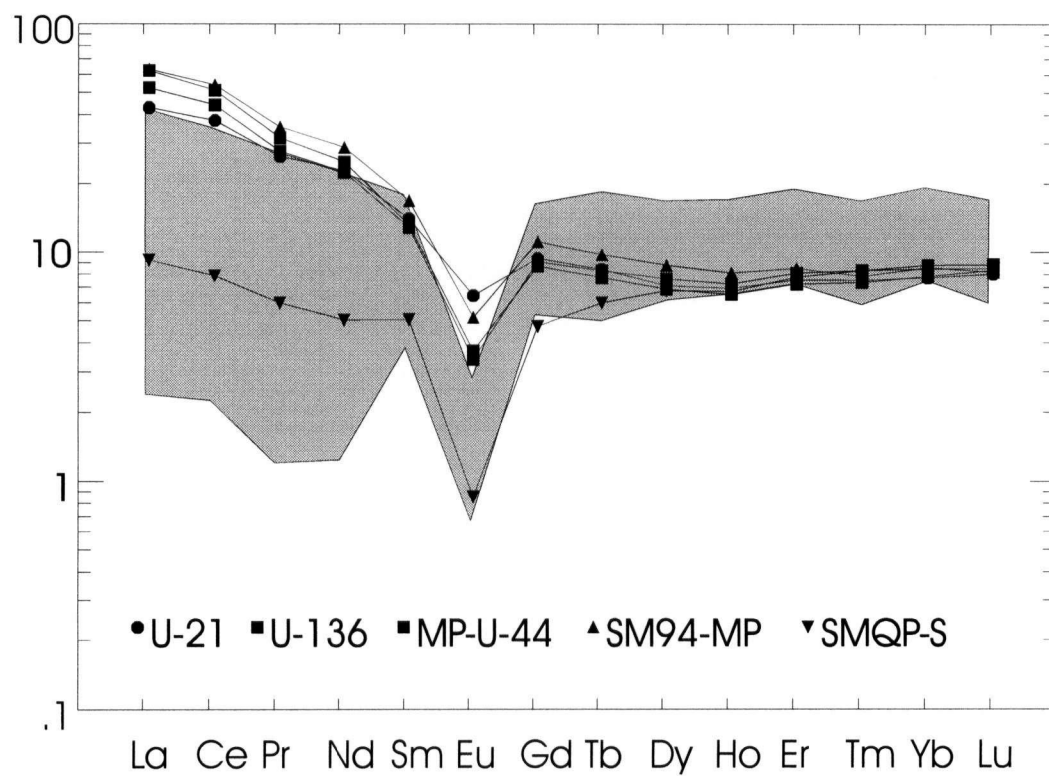
Patterson et al.: Figure 14



Patterson et al.: Figure 15



Patterson et al.: Figure 16



Patterson et al.: Figure 17

Table 1. Major Oxide Element and Rare Earth Element Abundances of Intrusive Rocks at the Sacrificio Deposit

sample	kp-1	kp-2	kp-3	kp-4	kp-5	kp-6	kp-7	kp-8	kp-9	kp-10	kp-11	kp-12	kp-13	kp-14	kp-16	kp-18	kp-19	kp-20
Oxides (wt %)																		
SiO ₂	74.59	61.94	74.68	62.01	74.67	74.33	73.44	62.96	58.23	62.43	75.66	75.55	93.9	75.66	74.49	74.2	75.67	76.58
TiO ₂	0.04	0.57	0.03	0.54	0.02	0.07	0.11	0.57	0.58	0.55	0.02	0.01	0.01	0.03	0.03	0.07	0.02	0.09
Al ₂ O ₃	13.51	16.71	12.61	16.66	13.02	13.45	13.13	16.53	18.26	17.03	13.06	12.81	2.78	12.68	13.03	13.17	13.1	11.65
Fe ₂ O ₃ ¹	0.48	4.17	0.18	1.33	0.93	0.27	1.51	3.35	3.55	4.31	0.31	0.68	0.19	0.1	1.36	1.12	0.34	0.95
MgO	0.04	2	<0.01	1.94	<0.01	<0.01	0.07	1.52	1.54	1.51	<0.01	<0.01	<0.01	<0.01	0.19	0.04	<0.01	0.02
MnO	0.01	0.09	<0.01	0.04	0.05	0.01	0.03	0.05	0.12	0.1	<0.01	0.03	0.01	<0.01	0.01	0.02	<0.01	0.04
CaO	0.25	5.1	0.28	4.66	0.53	0.47	0.8	4.82	10.23	4.71	0.44	0.46	0.04	0.23	1.99	0.99	0.99	0.91
Na ₂ O	3.31	3.79	1.17	6.96	3.8	4	3.33	5.74	4.69	5.62	3.67	3.39	0.04	1.13	2.52	3.56	3.59	2.2
K ₂ O	5.25	2.32	8.94	2.86	4.53	5.1	4.94	2.34	1.06	1.7	5.06	4.97	2	8.85	3.96	5	5.01	5.62
P ₂ O ₅	0.02	0.27	0.01	0.27	<0.01	0.03	0.04	0.28	0.31	0.26	0.01	0.01	0.01	0.02	0.01	0.01	<0.01	0.04
LOI	1.04	2.01	0.72	0.8	0.55	0.46	0.86	0.72	0.53	0.75	0.72	0.73	0.12	0.48	1.7	0.52	0.54	0.99
Total	98.54	98.97	98.62	98.07	98.1	98.19	98.26	98.88	99.1	98.97	98.95	98.64	99.1	99.18	99.29	98.7	99.26	99.09
Trace Elements (ppm)																		
La	1.5	28	4.5	23.5	4	12	27	36	15.5	35.5	4.5	5	1	3	4	18.5	7	24.5
Ce	3.5	54.5	9.5	48	11.5	29.5	56.5	72	40	72.5	9	18	3.5	7.5	9	39.5	19	53
Pr	0.3	6.6	1.5	5.8	1.2	4.1	6.9	8.9	5.5	8.5	1.3	1.8	0.6	1	1.2	5	2.7	6.2
Nd	1.5	25	7	25	5	17	26.5	33.5	25	33	5.5	8.5	3.5	4.5	6	18.5	12	23.5
Sm	1.5	5	3	5.4	2.1	6.1	7	6.8	5.6	6.4	2.6	4.5	1.7	1.8	3	5.4	6.3	6.2
Eu	0.1	1.2	0.1	1	<0.1	0.2	0.4	1.8	1	1.7	<0.1	<0.1	<0.1	<0.1	0.1	0.4	0.1	0.3
Gd	3.5	4.7	4.7	4.6	3	8.5	8	6.2	5.7	5.8	5.1	6.1	2.3	2.9	4.7	7.3	8.6	7
Tb	0.9	0.6	1	0.6	0.6	1.8	1.4	0.7	0.6	0.7	1.3	1.5	0.4	0.5	1.1	1.3	1.8	1.2
Dy	6.4	2.8	6.7	2.6	4.1	10.8	7.4	3.5	3.1	3.3	7.5	9.2	2.9	4.2	7.4	7.5	10.7	6.5
Ho	1.6	0.6	1.7	0.6	1	2.5	1.7	0.7	0.7	0.6	1.9	2.2	0.6	1	1.7	1.7	2.4	1.4
Er	4.8	1.7	5	1.9	3.5	8.1	5.3	2.3	1.8	2	6.1	7.1	1.6	3.2	5.6	5.1	7.6	4.6
Tm	0.7	0.2	0.7	0.2	0.5	1.1	0.7	0.3	0.3	0.2	0.9	1	0.2	0.4	0.8	0.7	1.1	0.6
Yb	5.6	1.8	4.7	1.4	4.2	8.3	5.3	1.8	2.1	2.1	6	7	1.3	3.4	6.1	5	6.9	4.5
Lu	0.7	0.1	0.7	0.2	0.5	1.1	0.7	0.2	0.2	0.2	0.8	1	<0.1	0.4	0.7	0.7	1	0.6

Analysis by Chemex Labs Ltd.; major oxide values by X-ray fluorescence spectroscopy; trace elements by inductively-coupled plasma – mass spectroscopy; 2σ error for major element concentrations is ± <0.3%, 2σ error for trace element concentrations is ± <0.5ppm with the exceptions of La, Ce, and Nd which are ± <2ppm (M.D.R.U. internal error analysis; S. Piercey, pers. commun., 2001); sample locations are shown in Figure 4.

¹ All iron reported as Fe₂O₃

kp-1 = Coloradito Eocene dike

kp-2 = Coloradito Cretaceous dike

kp-3 = Coloradito Eocene dike

kp-4 = Coloradito Cretaceous dike

kp-5 = Coloradito biotite granite

kp-6 = Coloradito Eocene dike

kp-7 = Sacrificio granite

kp-8 = Dique Viejo

kp-9 = Dique Viejo

kp-10 = Dique Viejo

kp-11 = Coloradito granite

kp-12 = Coloradito biotite granite

kp-13 = Coloradito silicified zone

kp-14 = Coloradito Eocene dike

kp-16 = Sacrificio granite (from core)

kp-18 = Sacrificio granite (from core)

kp-19 = Sacrificio granite (from core)

kp-20 = Sacrificio granite (from core)

Table 2. U-Pb isotope data

Sample Description ¹	Wt (mg)	U content (ppm)	Pb ² content (ppm)	²⁰⁶ Pb/ ²⁰⁴ Pb (meas.) ³	total common Pb (pg)	% ²⁰⁸ Pb ²	²⁰⁶ Pb/ ²³⁸ U ⁴ (± % 1σ)	²⁰⁷ Pb/ ²³⁵ U ⁴ (± % 1σ)	²⁰⁷ Pb/ ²⁰⁶ Pb ⁴ (± % 1σ)	²⁰⁶ Pb/ ²³⁸ U age (Ma; ± % 2σ)	²⁰⁷ Pb/ ²⁰⁶ Pb age (Ma; ± % 2σ)
KP-11											
A: N5,+104	0.032	12607	75.5	1725	94	4.3	0.00637(0.16)	0.04143(0.26)	0.04717(0.14)	40.9(0.1)	57.8(6.7)
B: N5,+104	0.030	12195	72.0	423	351	4.9	0.00624(0.24)	0.04027(0.61)	0.04682(0.51)	40.1(0.2)	40.0(24.3)
C: N5,+104	0.027	8713	51.7	700	136	5.0	0.00626(0.16)	0.04043(0.48)	0.04682(0.41)	40.2(0.1)	40.1(19.8)
D: N5,+104	0.028	11788	70.0	712	186	4.8	0.00629(0.18)	0.04057(0.38)	0.04682(0.28)	40.4(0.1)	40.1(13.4)
E: N5,+104	0.027	14149	82.7	983	153	4.4	0.00621(0.15)	0.04009(0.31)	0.04683(0.21)	39.9(0.1)	40.3(10.0)
KP-14											
A: N5,+104	0.045	8013	47.8	1599	91	3.7	0.00638(0.21)	0.04150(0.29)	0.04719(0.15)	41.0(0.2)	58.6(6.9)
B: N5,+104	0.047	12904	74.0	1069	221	3.6	0.00614(0.36)	0.03967(0.44)	0.04683(0.19)	39.5(0.3)	40.6(9.3)
C: N5,+104	0.043	10188	59.7	669	262	4.0	0.00625(0.26)	0.04035(0.54)	0.04681(0.43)	40.2(0.2)	40.1(20.4)
D: N5,+104	0.027	10077	59.2	1259	86	3.8	0.00628(0.14)	0.04051(0.33)	0.04681(0.25)	40.3(0.1)	40.1(12.2)
KP-7											
A: N2,+134	0.060	454	3.1	1296	9	9.3	0.00691(0.15)	0.04585(0.32)	0.04813(0.25)	44.4(0.1)	105.7(11.8)
B: N2,+134	0.050	233	1.4	801	6	7.3	0.00620(0.13)	0.04003(0.46)	0.04682(0.40)	39.8(0.1)	40.0(19.3)
C: N2,+134	0.105	662	4.4	535	57	8.5	0.00678(0.15)	0.04428(0.43)	0.04735(0.33)	43.6(0.1)	43.6(15.6)
D: N2,+134	0.107	623	3.5	977	25	8.4	0.00577(0.15)	0.03727(0.42)	0.04682(0.35)	37.1(0.1)	40.2(16.9)
E: N2,+134	0.084	524	3.3	1334	13	8.5	0.00640(0.11)	0.04155(0.24)	0.04709(0.17)	41.1(0.1)	53.7(7.9)
KP-9											
A: N2,+104,	0.076	408	12.1	3818	16	6.9	0.03061(0.10)	0.2230(0.18)	0.05284(0.10)	194.4(0.4)	321.8(4.6)
B: N2,+104	0.101	567	12.2	2200	36	8.4	0.02184(0.11)	0.1524(0.20)	0.05206(0.12)	139.3(0.3)	223.8(5.4)
C: N2,+104	0.103	498	13.1	5611	15	7.4	0.02696(0.11)	0.1982(0.17)	0.05332(0.09)	171.5(0.4)	342.6(4.1)
D: N2,+104	0.162	540	12.5	2156	60	8.3	0.02343(0.11)	0.1809(0.21)	0.05600(0.12)	149.3(0.3)	452.6(5.3)
E: N2,+104	0.159	426	9.5	1940	50	7.2	0.02286(0.10)	0.1669(0.21)	0.05295(0.13)	145.7(0.3)	326.7(5.9)
F: N2,74-104	0.017	784	19.2	1515	13	8.8	0.02472(0.18)	0.1691(0.37)	0.04961(0.29)	157.4(0.6)	176.8(13.6)
G: N2,74-104	0.013	566	16.7	2991	4	7.4	0.03003(0.12)	0.2275(0.25)	0.05495(0.18)	190.7(0.4)	410.2(8.1)
H: N2,+104,t	0.030	390	7.8	548	26	10.1	0.01981(0.16)	0.1352(0.45)	0.04947(0.35)	126.5(0.4)	170.2(16.4)
I: N2,+104,t	0.008	525	10.7	525	2	4.9	0.05402(0.24)	0.1466(0.54)	0.04963(0.47)	136.6(0.6)	177.9(22.0)
J: N2,62-74,e,u	0.048	462	7.8	875	26	7.6	0.01724(0.14)	0.1210(0.91)	0.05088(0.86)	110.2(0.3)	235.4(39.7)
K: N2,44-62,e,u	0.066	417	6.9	822	35	7.6	0.01707(0.18)	0.1135(1.25)	0.04824(1.19)	109.1(0.4)	110.8(56.4)

¹ N2, M2 = non-magnetic, magnetic at indicated number of degrees side slope on Frantz isodynamic magnetic separator; grain size given in microns; e = elongate; t = tabular, u = unabrased.

² radiogenic Pb, corrected for blank, initial common Pb, and spike

³ corrected for spike and fractionation

⁴ corrected for blank Pb and U, and common Pb

Table 3. Paragenesis of Alteration and Mineralization at the Sacrificio Deposit

Alteration		Mineralization	
<u>Style</u>	<u>Mineralogy</u>	<u>Style</u>	<u>Mineralogy</u>
Contact Metamorphism	quartz-albite-scapolite ± sericite ± chlorite	None	None
Prograde Skarn	garnet-wollastonite- clinopyroxene- vesuvianite	Disseminated Cu-Ag	bornite ± chalcopyrite
Minor Silicification	quartz	Fracture-controlled Cu-Ag±Au	chalcopyrite ± bornite ± sphalerite ± galena ± arsenopyrite
Retrograde Skarn	amphibole-chlorite ± epidote ± calcite	Massive Manto Zn-Cu-Pb-Ag±Au	sphalerite-galena- chalcopyrite- arsenopyrite-pyrite- pyrrhotite-bornite

Notes: only the major minerals are listed; secondary copper-oxide minerals are variably developed near surface in all styles of mineralization.

Chapter 3

Evolution and source of mineralizing fluids in the Sacrificio Cu (Zn-Pb-Ag-Au) skarn deposit, Durango, Mexico

Keith M. Patterson

(Co-Author: Stephen M. Rowins)

Abstract

The Sacrificio deposit, which is located in southeastern Durango State, Mexico, is hosted by mid-Cretaceous limestone, chert, and minor shale of the Cuesta del Cura and Indidura formations. Intrusive rocks include two temporally and compositionally distinct suites, dated at 109.1 ± 0.4 Ma (mid-Cretaceous) and 40.1 ± 0.5 Ma (Middle Eocene). The Middle Eocene granite suite is associated with the development of skarn and related sulfide mineralization that forms the Sacrificio deposit. Three episodes of pre-intrusion regional deformation (D_1 to D_3) and two episodes of syn-intrusion local deformation are recognized at the Sacrificio deposit. Skarn and skarn-related mineralization is localized within these regional and local structures and their intersections.

Alteration at the Sacrificio deposit is divided into pre-mineralization contact metamorphism, prograde skarn, and retrograde skarn. Three styles of skarn-related sulfide mineralization are present: (1) disseminated to semi-massive bornite and lesser chalcopryite filling secondary porosity in prograde garnet skarn; (2) fracture-controlled bornite-chalcopryite \pm sphalerite \pm galena \pm arsenopyrite with high Ag contents; and (3) fine- to coarse-grained semi-massive to massive sulfide bodies or "mantos", which are associated with retrograde amphibole skarn and contain a sulfide assemblage of arsenopyrite, pyrite, pyrrhotite, bornite, chalcopryite, sphalerite and galena. Rare quartz-arsenopyrite veins post-date all alteration and mineralization.

Skarn and sulfide-forming fluids at the Sacrificio deposit are interpreted to be magmatic in origin from lead isotope data. Compositions of garnet (Ad_{65} -

$_{100}\text{Gr}_{0-35}$) and pyroxene ($\text{Di}_{68-94}\text{Hd}_{5-30}\text{Jo}_{1-3}$) from prograde skarn that hosts disseminated bornite-chalcopyrite mineralization classify the Sacrificio skarn as a copper skarn. Fluid inclusion studies indicate that mineralizing fluids were dominantly H_2O -NaCl mixtures, although depressed eutectic temperatures indicate the presence of additional divalent cations (i.e., Mg^{2+} , Fe^{2+} , and Ca^{2+}). Disseminated and manto-style mineralization formed from fluids containing 0.5 – 13.8 wt. % NaCl equivalent, whereas post-skarn quartz-arsenopyrite veins were formed from fluids containing 6.1 – 19.7 wt. % NaCl equivalent. Pressures during the development of the Sacrificio deposit are estimated at approximately 0.5 to 1.0 kbar from stratigraphic reconstructions and geologic evidence. Temperatures of skarn formation and sulphide deposition show a gradual cooling of the skarn system. Prograde skarn formed at 460° to 580° C, disseminated Cu-Ag mineralization at 291° to 504° C, and mantos at 247° to 396° C. This was then overprinted by a final pulse of hotter fluids (318° to 480° C) which formed the late quartz-arsenopyrite veins.

Introduction

The Mexican Altiplano is host to numerous skarn and carbonate replacement deposits, which are significant past and present producers of Ag, Zn, Pb, and Cu (e.g., San Martin, Fresnillo, Chalchihuites, Concepcion del Oro, Velardeña; Megaw, 1999). The Sacrificio Cu (Zn-Pb-Ag-Au) skarn deposit occurs within this district (Fig. 18) and exhibits many of the features that characterize this class of mineral deposit. Pre- and syn-intrusion deformation is critically

important in controlling the distribution of mineralization at the Sacrificio deposit. The structural model developed at Sacrificio to explain the location of mineralization within regional and local structures (Patterson et al., *in review*) can be applied to many of the skarn and carbonate replacement deposits in the Altiplano. In this contribution, fluid inclusion, lead isotope, and mineralogical studies are used to investigate the source of the mineralizing fluids and the physicochemical conditions (P-T-X) of skarn formation and related mineralization at the Sacrificio deposit. Understanding fluid evolution and the localization of skarn-related mineralization at the Sacrificio deposit is important not only for local exploration activity, but also for predicting the location of undiscovered zones of mineralization in skarn and carbonate replacement deposits throughout the Mexican Altiplano.

Regional Geological Setting

The Sacrificio deposit is situated 80 km southeast of Durango, in a well-recognized northwest-trending belt of skarn and carbonate replacement deposits which include San Martín, Fresnillo, and Chalchihuites (Fig. 18). In this paper, the term deposit is used to describe the skarn-related sulfide mineralization at Cerro el Sacrificio owing to the ~15 years of production activity in the 1970's and 1980's at Mina Embotelladora, a small underground copper mine located on the northern flank of Cerro el Sacrificio. Additionally, numerous small historic adits and pits are present in the area (Fig. 19) and are evidence of previous mining activity.

The Sacrificio deposit lies within the Altiplano ("high plateau") of central Mexico which is underlain by thick Jurassic to Lower Cretaceous metasedimentary rocks which consist primarily of marine carbonate rocks with interbedded chert and shale (Sedlock et al., 1993). Mid-Tertiary plutons ranging from granite to diorite in composition intrude the Jura-Cretaceous strata. In addition to causing extensive hydrothermal alteration of adjacent host-rocks, these intrusions are thought to be responsible for the precious and base metal-rich mineral deposits of the Altiplano (e.g., Rubin and Kyle, 1988; Barton et al., 1995; Megaw, 1999).

The dominant structural fabric of the Altiplano is attributed to strong north-northeast-directed contraction associated with the Late Cretaceous to Middle Eocene Mexican fold-and-thrust belt (Sutter, 1987; Sedlock et al., 1993). The Sacrificio deposit lies in the westernmost or hinterland portion of the Mexican fold-and-thrust belt where regional folding is intense. In the Altiplano, folding and thrusting generally verges northeast to east-northeast, consistent with deformation throughout the North American Cordillera (e.g., Drewes, 1991). Deformation in the Mexican fold-and-thrust belt occurred during latest Cretaceous to Middle Eocene time (~ 70 to 45 Ma) and is temporally and kinematically similar to "Laramide" deformation in the southwestern U.S. (e.g., Sedlock et al., 1993).

The Mexican fold-and-thrust belt deformation front was spatially time transgressive, with deformation younging to the east (de Cserna, 1989). Magmatism associated with the orogeny was simultaneous with deformation but

localized some distance west of the thrust front and therefore after peak deformation (Sedlock et al., 1993). This simple relationship explains the post- to syn-deformation timing of pluton emplacement at Cerro el Sacrificio and at many other intrusion-related mineral deposits in central Mexico (e.g., Megaw, 1999).

Local Geological Setting

Supracrustal rocks which host the Sacrificio deposit consist of limestone, chert, and minor shale of the Cuesta del Cura (Upper Albian-Cenomanian) and overlying Indidura (Cenomanian to Santonian) formations (Longoria et al., 1999) (Fig. 19). Thick beds (10 to 40 cm) of grey limestone are interbedded with thin beds (1 to 10 cm) of white to grey chert in the Cuesta del Cura Formation. The Indidura Formation is similar, but also contains rare beds of black argillaceous shale. At the San Martin mine 30 km to the southeast, these formations are in excess of 1000 m in thickness (Rubin, 1986) and form a compositionally monotonous succession of chemically receptive host-rocks.

Intrusive rocks at the Sacrificio deposit comprise two temporally and compositionally distinct magmatic suites. The older suite is mid-Cretaceous in age (109.1 ± 0.4 Ma; U-Pb zircon age) and consists of feldspar-phyric quartz monzodiorite dikes of which Dique Viejo is the largest (e.g., Fig. 19). The younger suite is Middle Eocene in age (40.1 ± 0.5 Ma; U-Pb zircon age) and consists of the Sacrificio and Coloradito intrusions, both of which are multiphase, equigranular granites (Patterson et al., *in review*). A variety of geological evidence led Patterson et al. (in review) to conclude that skarn formation, sulfide

mineralization, and some of the local structures were caused by the emplacement of the Middle Eocene intrusive suite (Fig. 19).

Skarn-related Mineralization

Three styles of skarn-related sulfide mineralization are recognized at the Sacrificio deposit. These are (1) disseminated Cu-Ag mineralization in prograde skarn, (2) fracture-controlled Cu-Ag \pm Au mineralization in prograde skarn, and (3) massive to semi-massive sulfide or manto-style Zn-Cu-Pb-Ag-Au mineralization associated with retrograde skarn development. The fracture-controlled and disseminated styles of mineralization are spatially and genetically related, but macroscopic differences discussed below require that they be classified separately. Note that fractures are referred to as veins where filled by minerals in accordance with the terminology of the American Geological Institute (AGI) (Bates and Jackson, 1983). Rare, 1 to 3 cm wide, quartz-arsenopyrite veins cross-cut all mineralization styles and intrusive rocks.

Disseminated Cu-Ag mineralization is the most widespread style of mineralization at the Sacrificio deposit. It is characterized by small disseminations (up to 3 mm in diameter) and large, irregularly shaped clots (up to 2 cm in longest dimension) of bornite and lesser chalcopyrite filling secondary porosity in prograde garnet and wollastonite skarn (Fig. 20A). Relatively large areas (hundreds to thousands of square meters - Fig. 21) host disseminated bornite-chalcopyrite mineralization in prograde skarn on surface. Significant drill

core intersections of this style of mineralization include 1.72% Cu and 121 grams per tonne (g/t) Ag over 24.3 m (Terry et al., 1999).

Zones of fracture-controlled Cu-Ag \pm Au mineralization commonly contain very high grades of copper and silver (channel samples include up to 6.51% Cu and 554 g/t Ag over 1.5 m), but are generally of limited extent and tonnage. Sulfide minerals in this style of mineralization occur as coatings on fractures, as fillings in veins, and as disseminations concentrated within about 30 cm of the fractures (Fig 20B). This disseminated mineralization proximal to the fractures grades into the more widespread disseminated mineralization described above, but is differentiated from it based on the presence of sulfides other than bornite and chalcopyrite, and the concentration of this mineralization style near the fractures.

Veins typically are filled with quartz, calcite, and up to about 5% chalcopyrite and/or bornite plus minor sphalerite, galena, and arsenopyrite. Some rare veins, however, are composed almost entirely of sulfide minerals. Fractures and veins commonly occur together in zones several tens of meters in width with centimeter- to meter-scale spacing between individual fractures. Vein widths range from millimeters to tens of centimeters, with typical thicknesses on the order of 1 to 10 cm. Secondary copper minerals such as malachite, azurite, and chrysocolla commonly are developed in fracture zones due to the secondary oxidization of primary sulfide minerals.

Polymetallic mantos are becoming recognized as an increasingly important style of mineralization in the Sacrificio deposit (Terry et al., 1999). The

recent discovery of several new mantos by exploration diamond drilling has greatly increased the economic attractiveness of the deposit by increasing its metal potential from one of copper and minor silver to one of copper, zinc, silver and gold. Sulfide minerals identified in the mantos by reflected light microscopy and scanning electron microscopy (SEM) include sphalerite, galena, chalcopyrite, arsenopyrite, pyrite, pyrrhotite and bornite with rare tetrahedrite, stibnite, and stannite (Fig. 20C). Several mantos contain high concentrations of silver and locally gold. The best manto intersection includes 16.43 m of 1.48% Zn, 1.34% Cu, 0.99% Pb, and 174.6 g/t Ag (Terry et al., 1999).

Contact relationships between the mantos, prograde skarn, and marble indicate that the mantos post-date the prograde skarn and marble development. Common gangue minerals occurring with the mantos are characteristic of retrograde skarns (e.g., Einaudi et al., 1981) and include amphibole, chlorite, epidote, and calcite. In combination, these data indicate that polymetallic manto mineralization post-dates the disseminated and fracture-controlled Cu-Ag \pm Au mineralization.

Alteration

Alteration is divided into three types at the Sacrificio deposit. These are (1) pre-mineralization contact metamorphism, (2) prograde skarn, and (3) retrograde skarn. The contact metamorphism forms a large halo around the Sacrificio and Coloradito intrusions whereas the distribution of both prograde and retrograde skarn is strongly controlled by proximity to well-developed structures (Fig. 21).

The timing and association of mineralization and alteration styles is given in Table 4.

The earliest and most widespread style of alteration identified at the Sacrificio deposit is the pervasive development of hornfels in limestone and chert surrounding the Sacrificio and Coloradito intrusions (Fig. 21). Alteration minerals formed during this event include quartz, albite, scapolite, and minor sericite. This assemblage preferentially replaces chert beds (but locally also replaces limestone) in a halo up to 500 m wide surrounding the intrusions. The distribution of this alteration is controlled by proximity to the intrusions - it is unaffected by the structures that localized prograde and retrograde skarn. This hornfels is interpreted as a product of heat generated by the intrusions.

Structurally controlled prograde skarn, which hosts the disseminated bornite-chalcopyrite mineralization, is the most strongly developed hydrothermal alteration exposed on surface at the Sacrificio deposit (Fig. 21). Prograde skarn dominantly consists of massive to poddy garnet but also includes wollastonite, clinopyroxene, and vesuvianite. The garnets, as determined by electron microprobe analysis (see below), are members of the grossular-andradite solid solution series using the method of classification of Rickwood (1968). They occur as euhedral, coarse-grained, apple green crystals up to 2 cm in diameter. In thin section, garnets invariably display compositional zoning and weak anisotropism (Fig. 22A). Wollastonite occurs as white, bladed, commonly radiating crystals up to 3 cm in length. Clinopyroxene is typically dark green and occurs as masses of anhedral to subhedral crystals that in thin section generally show evidence of

alteration and/or replacement (Fig. 22B). Vesuvianite is present as brown, subhedral to euhedral laths ranging up to 1 cm in length that characteristically display weak compositional zonation in thin section. At the scale of outcrop, garnet, wollastonite, clinopyroxene, and vesuvianite generally occur together as prograde skarn. At the scale of hand sample or thin section, a zonation is developed from proximal garnet, to garnet+clinopyroxene, to more distal wollastonite \pm vesuvianite with increasing distance from a fracture or vein.

Retrograde skarn occurs at several locations on the Sacrificio property and is commonly associated with manto-style mineralization. Dark green, pervasive, poddy and veinlet-controlled amphibole typify this alteration style. Associated minerals include chlorite, quartz, calcite, and epidote. On surface, retrograde skarn forms zones tens to hundreds of square meters in area peripheral to both the Sacrificio and Coloradito intrusions (Fig. 21). In thin section, amphibole generally occurs as fine-grained, subhedral to anhedral crystals, although rare occurrences of course-grained, euhedral, laths are noted (Fig. 22C). Most amphibole examined is actinolite to ferro-actinolite with rare hornblende in some zones. In drillcore, retrograde skarn clearly post-dates prograde garnet-wollastonite skarn (Fig. 22D).

Quartz-arsenopyrite veins cut all styles of mineralization, alteration, and types of lithologies at the Sacrificio deposit. These veins are generally 1 to 3 cm in width and are surrounded by a weak alteration halo (up to 10 cm in width) consisting mainly of quartz and sericite. Quartz-arsenopyrite veins are best

recognized in drill core where they commonly cut the Coloradito and Sacrificio intrusions.

Garnet and Clinopyroxene Mineral Chemistry

Einaudi et al. (1981) demonstrated that skarn deposits are best classified by their dominant economic metals into six types, namely: iron, tungsten, copper, zinc-lead, molybdenum, and tin. Meinert (1989) subsequently classified gold skarns as a separate type. Classification of the polymetallic Sacrificio skarn deposit is somewhat problematic because it contains elements of both copper and zinc skarns (e.g., Einaudi et al., 1981). For example, the extensive zones of fracture-controlled and disseminated bornite-chalcopyrite mineralization at Mina Embotelladora are characteristic of copper skarns, whereas the sphalerite-rich mantos mined at Rosas de Diciembre (Fig. 19), and intersected in diamond drill core, are typical of zinc skarns. Fortunately, the compositions of garnet and clinopyroxene associated with the formation of prograde skarn can be used, in addition to metal abundances, to discriminate between copper and zinc skarns (e.g., Einaudi et al., 1981; Meinert, 1992). To this end, the compositions of garnet and clinopyroxene in a suite of prograde skarn samples were determined by electron microprobe analysis in order to classify the Sacrificio skarn deposit. Classification of the Sacrificio deposit allows for comparison with other similar deposits and application of genetic models developed elsewhere to the Sacrificio skarn. Samples containing both garnet and pyroxene in close association with

disseminated bornite-chalcopyrite mineralization were collected from large exposures of prograde skarn directly above the Sacrificio intrusion.

Garnet microprobe analyses were recast into mol. % end-members grossular (Gr), Andradite (Ad), Spessartine (Sp), and Almadine (Ad) following the procedure of Rickwood (1968). These data indicate that garnets are members of the Ad - Gr solid-solution series (i.e., grandite garnet) and range in composition from nearly pure Ad to 35 mol. % Gr. Representative analyses are given in Table 5. This chemical variation is explained by a nearly perfect 1:1 substitution of Al^{3+} for Fe^{3+} (Fig. 23). This chemical substitution is reflected optically in garnets by the lighter colored bands having more grossular-rich (Al-rich) compositions than the darker colored bands which are more andradite-rich (Fe-rich).

Clinopyroxene analyses were recalculated into mol.% end-members hedenbergite (Hd), diopside (Di) and johannsenite (Jo) following the method of Deer et al. (1992). The microprobe analyses reveal that clinopyroxenes lie along the Di-Hd solid-solution series and have only a minor Jo component. Compositions range from 68 to 94 mol. % Di, 5 to 30 mol. % Hd, and 1 to 3 mol. % Jo. Representative analyses are given in Table 5. Clinopyroxene compositions are evenly distributed along these ranges with an average composition of $\text{Di}_{84}\text{Hd}_{14}\text{Jo}_2$. Zoning was not observed in the clinopyroxene.

These garnet and clinopyroxene compositions fall within the range of compositions for copper skarns as defined by Meinert (1992) (Fig. 24). This finding, in addition to the relative abundance of copper mineralization compared to zinc mineralization, classifies the Sacrificio deposit as a copper skarn.

Structural Model

The localization of skarn mineralization and alteration within structures at the Sacrificio deposit is explained within a framework of five distinct episodes of deformation (Patterson et al., *in review*). Briefly, the three earliest deformation events (D_1 to D_3) recognized at the Sacrificio deposit are attributable to long-lived, progressive, deformation within the Mexican fold-and-thrust belt. The final two events (D_4 and D_5) are attributed to the emplacement of the Sacrificio intrusion. A sequential rendition of deformation and associated mineralization from D_1 to D_5 is schematically illustrated in Figure 25. The paragenetic relationships between the structures and the various styles of alteration and mineralization are detailed in Figure 26.

D_1 is a relatively ductile folding event, which records an estimated 100 to 150% shortening in the area of Cerro el Sacrificio. D_1 folds are tight to isoclinal, inclined to recumbent, and generally have amplitudes of ten centimeters to three meters. D_1 folds are strongly asymmetric and typically verge to the west. D_1 fold axes trend towards 330° with a maximum shortening direction of east-northeast.

D_2 is a minor event likely due to a local realignment of regional stresses as a result of strain partitioning or extreme competency contrast. It has limited effect on the present form of stratified rocks in the mapped area, but is unambiguously recognized at several outcrops. D_2 consists of type 2 refolding of D_1 folds (fold axial surfaces approximately perpendicular; McClay, 1987).

With respect to localization of skarn, D_3 folding is the most important deformation event defined at Sacrificio. D_3 folds are large amplitude (hundreds of

meters), gentle to open, upright folds which refold D_1 folds with similarly oriented fold axes (type 3: McClay, 1987). D_3 fold axial surfaces, particularly in anticlines, have focussed ascending metalliferous and skarn-forming magmatic fluids leading to the present distribution of garnet skarn and disseminated mineralization. The largest and most strongly mineralized D_3 fold mapped at the Sacrificio deposit is the Central Anticline (Fig. 19). D_3 fold axes trend toward 330° and plunge gently to the north or south depending on their location within the dome produced by D_4 .

D_4 is attributed to the forceful emplacement of the Sacrificio intrusion, which resulted in the gentle doming of rocks above and around the intrusion as defined by the plunges of D_1 and D_3 fold axes. In rocks above the northern half of the intrusion, D_1 and D_3 fold axes plunge to the north-northwest, whereas in rocks above the southern half of the intrusion, these fold axes plunge to the south-southeast. Fluids released from the crystallizing intrusion at this time were channeled upward along D_3 fold axial surfaces as evidenced by the localization of prograde skarn.

Elevated pore fluid pressures due to continued exsolution of magmatic fluids and/or their interaction with carbonate host rocks causing an increase in the partial pressure of H_2CO_3 , (e.g., Shoji, 1975; Johnson and Norton, 1985), are proposed to have caused mode I (extension) fractures to form above the intrusion (D_5). D_5 fractures are dominantly steeply dipping and generally strike east-northeast (Fig. 21), possibly indicating that a weak east-northeast oriented regional compressional stress field still existed at this time. Metalliferous fluids

exsolved from the intrusion were preferentially channeled into these newly formed fractures and subsequently into porous garnet skarn. This channeling of fluids resulted in significant concentrations of disseminated bornite and lesser chalcopyrite in garnet skarn proximal to the D₅ fractures. The sequence of events presented here is consistent with field evidence that show intersections between garnet skarn and D₅ fractures invariably host strong disseminated bornite-chalcopyrite mineralization.

Fluid Inclusion Microthermometry

A study of fluid inclusions trapped in hydrothermal quartz from several styles of mineralization and post-mineralization quartz-arsenopyrite veins was undertaken in order to determine the temperatures of mineralization and the composition of the metalliferous fluids. In addition, these data are used to document fluid evolution in the skarn system and provide insight into the processes responsible for mineral deposition (i.e., fluid mixing, fluid boiling or phase separation, etc...). Integration of these fluid inclusion data with lead isotope studies (see below) and detailed structural, petrological, and geochronological data (Patterson et al., *in review*), permit the construction of a comprehensive mineralization model for the Sacrificio deposit.

Methodology

Microthermometric data were collected from one hundred and seventy eight fluid inclusions in ten rock-samples considered representative of (1)

disseminated Cu-Ag mineralization associated with prograde skarn, (2) polymetallic manto mineralization associated with retrograde skarn, and (3) unmineralized quartz-arsenopyrite veins that post-date skarn formation. Note that because the fractured-controlled Cu-Ag \pm Au mineralization is genetically related to the disseminated Cu-Ag mineralization, its fluid inclusion characteristics can be approximated by the microthermometric data collected for the disseminated Cu-Ag style. Microthermometric measurements of fluid inclusions were conducted using a FLUID INC.-adapted USGS gas-flow heating-freezing stage at the University of British Columbia. Accuracy of the measurements was ensured by calibration against the triple point of pure CO₂ (-56.6° C), the freezing point of water (0.0° C), and the critical point of water (374.1° C), using synthetic fluid inclusions supplied by FLUID INC. Accuracy of the temperatures obtained in this study was $\pm 0.2^\circ$ C for freezing runs, and $\pm 3.0^\circ$ C for heating runs between 40° to 600° C. Measurements were made using a heating rate of approximately 1° C per minute. Freezing runs were conducted prior to heating runs in order to minimize the possibility of stretching and post-entrapment leakage of fluid inclusions (e.g., Roedder, 1984). Wafers of doubly polished thin sections containing fluid inclusions were cooled rapidly to approximately -120° C and then warmed slowly in order to measure both the first ice melting or eutectic temperature (T_e) and the final ice melting temperature (T_m). Continued heating permitted the determination of total homogenization temperatures (T_h) for these same inclusions. In some wafers it was possible to collect additional T_h data where suitable inclusions occurred in the same field of

view as the inclusions undergoing complete microthermometric analyses (i.e., both freezing and heating runs). Reduction of microthermometric data was done with the MacFlinco software program (Brown and Hagemann, 1995).

Fluid inclusion petrography

Doubly polished thin sections of each sample were examined in detail to record the nature of fluid inclusion distribution, size, and types, and to determine their spatial, temporal, and textural relationships. All inclusions studied were hosted in crystals of quartz with petrographic evidence for co-precipitation with sulfide mineralization. Genetic classification of inclusions as primary, pseudosecondary, or secondary follows the criteria given by Roedder (1984). In this study only primary, or rarely pseudosecondary, inclusions with regular edges and rounded shapes were used in order to minimize the possibility of analyzing secondary inclusions unrelated to mineralization (or arsenopyrite crystallization in the case of the quartz-arsenopyrite veins). Finally, microthermometric analysis was conducted only on inclusions with diameters greater than 8 μm to permit the determination of phase changes with a high degree of accuracy.

Primary and pseudosecondary fluid inclusions encountered during the course of this study are remarkably similar in appearance at room temperature. They normally range from 5 to 30 μm in diameter (averaging about 12 μm) and contain separate aqueous liquid and vapor phases (Fig. 27). A separate carbonic phase is not present. All inclusions studied are liquid-rich (i.e., >50 volume % liquid), with 84% containing greater than 70 volume % liquid. Interestingly, those primary

and/or pseudosecondary inclusions localized in trails and clusters invariably display consistent proportions of liquid and vapor. Daughter minerals are rare, although approximately 16% of the inclusions studied contain a small rounded solid (1 to 3 μm in diameter) with high birefringence under crossed-polars in transmitted light. This daughter mineral is almost certainly a carbonate species (e.g., Shepherd et al., 1985). Halite is notably absent in all inclusions studied, but a small irregularly shaped opaque solid in small percentage of inclusions may be a sulfide mineral.

Microthermometric data

The microthermometric data of fluid inclusions from the two styles of mineralization and the late-stage quartz-arsenopyrite veins are summarized in Table 6 and discussed below. Eutectic temperatures were measured for sixty-three fluid inclusions associated with disseminated and manto mineralization and the post-mineralization quartz-arsenopyrite veins in order to determine the cation composition of the fluids. The range of eutectic temperatures (-19.7° to -47.0° C) is similar for both styles of mineralization and the quartz-arsenopyrite veins (Figs. 28A-C). The depression of T_e below -21.2° C is suggestive of the presence of divalent cations such as Mg^{2+} , Fe^{2+} , and Ca^{2+} in the fluids in addition to Na^+ (e.g., Borisenko, 1977; Crawford, 1981; Davis et al., 1990). This finding is consistent with the presence of carbonate daughter minerals and expected fluid compositions in the calcic skarn environment (e.g., Bowman, 1998). The overlapping range of eutectic temperatures for the disseminated and manto

mineralization associated with prograde and retrograde skarn, and the post-skarn quartz-arsenopyrite veins, suggests that overall fluid compositions did not change systematically during evolution of the Sacrificio skarn system.

The final ice melting temperatures from sixty-eight fluid inclusions were used to estimate the salinity of the mineralizing fluids (e.g., Bodnar, 1993). Although fluids were not pure H₂O-NaCl mixtures, the presence of additional cations does not introduce appreciable error into the calculation of salinities (Clynne and Potter, 1977), which are expressed as weight percent NaCl equivalents (wt.% NaCl eq.). Clathration did not occur during any heating or freezing runs supporting the lack of optical evidence (i.e., a separate carbonic phase) for significant CO₂-CH₄ in the fluid. Final melting temperatures of inclusions from the disseminated Cu-Ag mineralization vary from -0.8° to -9.9° C indicating a salinity of 1.3 to 13.8 wt.% NaCl eq. (Fig. 28D). The T_m of inclusions from the mantos vary from -0.3° to -5.4° C, equivalent to a salinity of 0.5 to 8.4 wt.% NaCl eq. (Fig. 28E). These data are virtually identical to those of inclusions from the disseminated Cu-Ag mineralization (Figs. 28D & E). Inclusions in the quartz-arsenopyrite veins, however, have T_m between -5.0° and -16.4° C which correspond to salinities between 6.1 to 19.7 wt % NaCl eq., a range significantly higher than that of both the disseminated and manto styles of mineralization (Fig. 28F).

Homogenization temperatures were measured for one hundred and fifty eight fluid inclusions in order to place constraints on the temperatures of mineralization. Homogenization temperatures of the disseminated Cu-Ag

mineralization vary between 251° and 389° C and display two broad maxima: a lower temperature maximum at about 300° C and a higher temperature maximum at around 370° C (Fig. 28G). The T_h measured for manto mineralization are lower and range from 205° to 306° C with a broad maximum at around 275° C (Fig. 28H). Homogenization temperatures of inclusions in the quartz-arsenopyrite veins are similar to those in the disseminated mineralization and range from 278° to 383° C and lack any pronounced maximum (Fig. 28I).

Microthermometry results

The absence of vapor-rich inclusions and groups of inclusions with substantially variable liquid/vapor ratios indicates that fluid boiling or phase separation (e.g., Pichavant et al., 1982; Bodnar et al., 1985; Brown 1998) did not occur during formation of the Sacrificio deposit. The fact that all inclusions homogenized to the liquid phase also supports this conclusion. Consequently, the homogenization temperatures measured in this study provide only minimum estimates of the temperatures of mineralization (Roedder, 1984). In order to estimate the true trapping temperatures, a "pressure-correction" must be added to the measured temperatures of homogenization (e.g., Potter, 1977). To calculate this pressure correction for H₂O-NaCl fluids, it is necessary to estimate the trapping pressure under which the mineralization formed. At the Sacrificio deposit, trapping pressure can be estimated from an approximation of the thickness of overlying strata at the time of mineralization. Graf (1987) estimates that at the time of ore formation at the nearby San Martin mine, the thickness of

strata above the mineralizing intrusion was 1.5 to 3.0 km. The Sacrificio deposit occurs at the same stratigraphic level as the San Martin mine (i.e., just below the Indidura/Cuesta del Cura Formation contact) and likely formed under a similar depth of cover. From these stratigraphic considerations and assuming an average crustal density of 2.7 g/cm^3 (i.e., lithostatic conditions), it is estimated that the Sacrificio deposit has formed at pressures between 0.5 and 1.0 kbar. Details on the method of calculation are given in Shepherd et al. (1985). These pressure estimates are robust and do not change more than 0.1 or 0.2 kbar if the values for depth of cover and crustal density are varied to reflect geological uncertainty. The assumption that mineralization formed under near-lithostatic pressure conditions appears justified for the Sacrificio deposit as the calculated range of pressures using a lithostatic load is similar to that expected for copper skarn deposits (e.g., Einaudi et al., 1981; Bowman, 1998).

Using these pressure estimates and assuming a fluid salinity of 5 wt.% NaCl eq., the figures of Potter (1977) indicate that pressure corrections of 40° to 115°C and 40° to 90°C are required for disseminated Cu-Ag and polymetallic manto styles of mineralization, respectively. These pressure corrections give trapping temperatures of 291° to 504°C for disseminated Cu-Ag mineralization and 247° to 396°C for polymetallic manto mineralization. Similar calculations for the quartz-arsenopyrite veins assuming a fluid salinity of 10 wt.% NaCl eq. result in pressure corrections of 40° to 97°C . This yields trapping temperatures of 318° to 480°C . These pressure correction data are represented graphically in figures

29 and 30, which are pressure-temperature plots of isochores for the system $\text{H}_2\text{O}-\text{NaCl}$ (Bodnar and Vityk, 1994).

Lead Isotope Study

A lead isotope study was undertaken in order to constrain the source(s) of lead and, by inference, other metals in the Sacrificio deposit. Under the appropriate geological conditions, lead isotope studies are a very effective means of identifying the source(s) of metals in a wide variety of ore deposits (e.g., Richards et al., 1991; Rowins et al., 1997; Tosdal et al., 1999). Samples of potential source rocks including intrusions and meta-sedimentary host rocks were analyzed, as were samples of the different styles of mineralization (Table 7). Lead isotope compositions were obtained for sixteen samples of sulfide minerals using galena where possible and trace lead in other sulfides where galena was unavailable. Whole rock lead isotope compositions were obtained from three samples of unaltered limestone and shale. Lead isotope compositions from four samples of intrusive rock were determined using feldspar.

Analytical procedure

Lead isotope analyses were done in the geochronology laboratory at the University of British Columbia. Small clean cubes of galena were handpicked, washed, and dissolved in dilute HCl. Trace lead analyses of sulfide and feldspar samples were prepared from pure, hand-picked grains. Sulfide samples for trace Pb analysis were leached in HCl to remove surface contamination before

dissolution in nitric acid. Feldspar samples were ground and sieved and the 100-200 mesh fraction was first leached in a mixture of HF and HCL, and subsequently dissolved in concentrated HF. Trace lead whole rock samples were prepared from approximately 50mg of crushed rock, that was leached in dilute hydrochloric acid then dilute hydrofluoric and hydrobromic acids to remove surface contamination before dissolution in hydrofluoric acid and nitric acid. Separation and purification of Pb for trace Pb analyses employed ion exchange column techniques. The samples were converted to bromide, and the solution was passed through ion exchange columns in HBr, and the lead eluted in 6N HCl. The total procedural blank on the trace lead chemistry was 100-110 pg.

Approximately 10-25 ng of lead in chloride form was loaded on a rhenium filament and isotopic compositions were determined on a Faraday collector using a modified VG54R thermal ionization mass spectrometer. The measured ratios were corrected for instrumental mass fractionation of 0.12% per mass unit based on repeated measurements of the N.B.S. SRM 981 Standard Isotopic Reference Material. Errors reported in Table 7 were obtained by propagating all mass fractionation and analytical errors through the calculation.

Results and Interpretation

Thorogenic ($^{208}\text{Pb}/^{204}\text{Pb}$ vs. $^{206}\text{Pb}/^{204}\text{Pb}$), uranogenic ($^{207}\text{Pb}/^{204}\text{Pb}$ vs. $^{206}\text{Pb}/^{204}\text{Pb}$), and $^{208}\text{Pb}/^{206}\text{Pb}$ vs. $^{207}\text{Pb}/^{206}\text{Pb}$ lead plots (Fig. 31) show lead compositions of all styles of mineralization to cluster tightly with those of the intrusive rocks. Lead compositions of sedimentary host rocks including limestone

and shale from the Cuesta del Cura and Indidura Formations are considerably more radiogenic. From these data it is interpreted that lead and, by inference, other metals (e.g., Henley et al., 1984; James and Henry, 1993; Megaw et al., 1996; Tosdal et al., 1999) in mineralization at the Sacrificio deposit were derived almost exclusively from magmatic-hydrothermal fluids originating from the intrusions. Implicit in this interpretation is the assumption that if sedimentary host rocks contributed significant lead to the mineralization, lead isotope signatures in the mineralization would trend towards the values of the host rocks.

The fact that both the older (109.1 ± 0.4 Ma) and younger (40.1 ± 0.5 Ma) intrusive suites have similar lead isotopic signatures makes it impossible to assign one or the other as the source of mineralization based solely on lead isotope data. However, the spatial distribution of alteration and mineralization styles, together with the weak alteration of the older Dique Viejo, conclusively identifies the younger intrusive suite (i.e., the Coloradito and Sacrificio intrusions) as the source of mineralization and alteration on the property.

Discussion

Skarn Classification

Garnet and pyroxene compositional data in addition to relative metal abundances allow the classification of the Sacrificio deposit as a copper skarn. The deposit shares many of the features found in copper skarns as detailed by Einaudi et al. (1981). These include a zonation from proximal garnet to garnet-

pyroxene to distal wollastonite-vesuvianite prograde skarn as distance from a fluid pathway increases, and high overall garnet to pyroxene ratios.

Source of Metals and Fluids

The source of mineralizing fluids at the Sacrificio deposit has been very effectively constrained through the use of lead isotope data. These data (Fig. 31 and Table 7) show that sulfides in all styles of mineralization have similar lead isotopic signatures to the intrusive rocks on the property. Given that the sedimentary host rocks, the only other likely source of lead in the district, have significantly more radiogenic lead isotope signatures, it is concluded that the lead and, by inference, other metals in the sulfide minerals are derived from the intrusions. Consequently, it may be tentatively concluded that skarn and sulfide mineralization at the Sacrificio deposit formed from fluids of magmatic origin. This lead isotope evidence of a magmatic origin for the skarn- and sulfide-forming fluids is consistent with the timing of mineralization with respect to the development of late structures at the Sacrificio deposit. D₄ (dome formation) is attributed to emplacement of the Sacrificio intrusion and D₅ (east-northeast-striking fractures) to elevated pore fluid pressures associated with exsolving magmatic fluids.

Physicochemical Conditions of Skarn Formation and Related Mineralization

The pressures and temperatures attending evolution of the Sacrificio skarn system have been constrained with fluid inclusion data and stratigraphic

reconstructions. Pressure is assumed to have remained relatively constant throughout the development of the skarn system at 0.5 to 1.0 kbar, whereas temperature varied considerably.

Maximum temperatures in wallrock surrounding the Sacrificio intrusion can be estimated using heat flow-balance considerations (Bowman, 1998). Heat flow-balance gives a maximum temperature in wallrock of approximately 60% of the difference between initial magma and initial wallrock temperature plus the initial wallrock temperature (Turcotte and Schubert, 1982). Assuming intrusion crystallization temperatures of approximately 900° C (Philpotts, 1990), a geothermal gradient of 35° C per kilometer (Blackwell et al., 1990), and 1.5 to 3.0 km depth of burial, maximum wallrock temperature is calculated to be approximately 560° to 580° C. These temperatures represent maximum temperatures for prograde skarn formation.

Minimum temperatures of prograde skarn formation are constrained by the presence of wollastonite. Pressure-temperature conditions of the reaction forming wollastonite from quartz and calcite at a mol. fraction $[X(\text{CO}_2)]$ of 0.1 are shown in Figure 32. Low $X(\text{CO}_2)$ in skarn-forming fluids (likely <0.04) is indicated by the lack of immiscible carbonic phases in fluid inclusions studied (e.g., Bowers and Helgeson, 1983). Given these considerations, a $X(\text{CO}_2)$ of 0.1 is an appropriate maximum approximation for fluids forming prograde skarn. Estimated pressures of 0.5 to 1.0 kbar give minimum temperatures of prograde skarn formation of 460° to 510° C (Fig. 32). Together with the maximum temperatures given by heat flow-balance calculations, it is concluded that the temperatures of

prograde skarn formation are 460° to 560° C at 0.5 kbar and 510° to 580° C at 1.0 kbar.

Disseminated Cu-Ag mineralization (and by inference the genetically related fracture-controlled Cu-Ag \pm Au mineralization) postdates the prograde skarn and formed at significantly lower temperatures. The temperatures of disseminated Cu-Ag mineralization given by fluid inclusion data range from 291° to 444° C at 0.5 kbar and 333° to 504° C at 1.0 kbar.

Manto mineralization and associated retrograde skarn formation postdates both prograde skarn and disseminated Cu-Ag mineralization. It records an overall cooling of the skarn system as the intrusive heat source wanes. Fluid inclusion data give temperatures of formation of manto mineralization from 247° to 346° C at 0.5 kbar and 286° to 396° C at 1.0 kbar.

Temperatures of formation of prograde skarn, disseminated mineralization, and manto mineralization record a consistent cooling of the skarn system (Fig. 33). Quartz-arsenopyrite veins, which postdate skarn formation and cut both the Sacrificio and Coloradito intrusions, represent a reversal in this cooling trend with higher temperatures of 318° to 423° C at 0.5 kbar and 368° to 480° C at 1.0 kbar. This temperature increase late in the evolution of the system, and the significantly higher salinity of the fluids forming these veins (6.1 – 19.7 wt.% NaCl eq. versus 0.5 – 13.8 wt. % NaCl eq. for the disseminated and manto mineralization; Table 6), suggest that the quartz-arsenopyrite veins may have formed from fluids related to a late, more deeply buried, intrusive phase that has yet to be identified.

The evolutionary trends in trapping temperatures identified in this study will remain valid regardless of the exact pressures of skarn formation and related sulfide mineralization due to the relative constancy of pressure during formation of the deposit. Consequently, changes to the trapping pressure will simply shift the trapping temperatures for all styles of mineralization and the unmineralized quartz-arsenopyrite veins to uniformly higher or lower temperatures depending on the nature of the pressure change.

Conclusions

The source, composition, and pressure-temperature conditions of fluids forming calc-silicate skarn, and the various styles of sulfide mineralization, at the Sacrificio Cu (Zn-Pb-Ag-Au) deposit have been determined using lead isotope, fluid inclusion, and geological data. The Sacrificio deposit has been classified as a copper skarn through the use of garnet and pyroxene compositional data in addition to metal abundances.

Fluids responsible for skarn and sulfide mineralization at the Sacrificio deposit are identified as magmatic in origin through lead isotope studies of intrusive rocks, metasedimentary host rocks, and different styles of mineralization. Fluid inclusion studies indicate that mineralizing fluids were dominantly H₂O-NaCl mixtures, although depressed eutectic temperatures indicate the presence of additional divalent cations (i.e., Mg²⁺, Fe²⁺, and Ca²⁺). Disseminated Cu-Ag and manto-style mineralization formed from fluids containing 0.5 to 13.8 wt. % NaCl eq., whereas post-skarn quartz-arsenopyrite

veins formed from fluids containing 6.1 to 19.7 wt. % NaCl eq. Pressures of mineralization at the Sacrificio deposit are estimated to range from 0.5 to 1.0 kbar based on stratigraphic reconstructions and assuming near-lithostatic conditions. Temperatures of skarn formation and sulfide deposition indicate a gradual cooling of the skarn system. Prograde skarn formed at 460° to 580° C, disseminated Cu-Ag mineralization at 291° to 504° C, and mantos at 247° to 396° C. The final hydrothermal event recorded at the Sacrificio deposit is the formation of unmineralized quartz-arsenopyrite veins from fluids with higher temperatures (318° to 480° C) than those which formed the mantos and retrograde skarn.

Consideration of the geochemical and isotopic data from this study, together with the structural and geochronological data from Patterson et al. (in review), has enabled the construction of a detailed fluid evolution model for skarn formation at Cerro el Sacrificio. Application of the findings from this study to other large, polymetallic, skarn deposits or prospects in Mexico could lead to the discovery of new orebodies.

Acknowledgments

This paper is a portion of the senior author's M.Sc. research undertaken at the University of British Columbia. The research was supported both financially and logistically by Boliden Limited. Additional financial assistance was provided by NSERC grant 22R80466 to Rowins, a Thomas and Marguerite MacKay memorial scholarship to Patterson, and an SEGF student research grant to Patterson. In

particular, we would like to thank David Terry and Chris Rockingham for the many ideas they have contributed throughout the course of this study. Additionally, James Mortensen is thanked for a critical review of this manuscript. Fieldwork could not have been undertaken without the logistical aid of David Aguilar Ortiz, Ricardo Flores, and Florentino Munoz of Luismin, S.A. de C.V. Mati Raudsepp and Elisabetta Pani contributed much knowledge and expertise to the microbeam analyses. Finally, Janet Gabites, from the Geochronology Laboratory at the University of British Columbia, is thanked for the lead isotope analyses.

References

- Albinson, T., 1988, Geologic reconstructions of paleosurfaces in the Sombrerete, Colorada, and Fresnillo Districts, Zacatecas State, Mexico: *Econ. Geol.*, v. 83, p. 1647-1667.
- Barton, M.D., Staude, J-M.G., Zurcher, L., and Megaw, P.K.M., 1995, Porphyry copper and other intrusion-related mineralization in Mexico, *in* Pierce, F.W. and Bolm, J.G., eds., *Porphyry copper deposits of the American Cordillera: Arizona Geological Society Digest*, v. 20, p. 487-524.
- Bates, R.L., and Jackson, J.A., 1983, *Dictionary of Geological Terms*, 3rd Edition: American Geological Institute, Doubleday Anchor, New York, 571 p.
- Blackwell, D.D., Steele, J.L., Frigme, C.F., Murphey, C.F., Priest, G.R., and Black, G.L., 1990, Heat flow in the Oregon Cascade Range and its correlation with regional gravity, Curie point depths, and geology: *Journal of Geophysical Research*, v.95-B12, p. 19475-19493.
- Bodnar, R.J., 1993, Revised equation and table for determining the freezing point depression of H₂O-NaCl solutions: *Geochimica Cosmochimica Acta*, v. 57, p. 683-684.
- Bodnar, R.J., Reynolds, T.J., and Kuehn, C.A., 1985, Fluid inclusion systematics in epithermal systems, *in* B.R. Berger & P.M. Bethke, eds., *Geology and Geochemistry of Epithermal Systems: Society of Economic Geology Reviews in Economic Geology*, v. 2, p. 73-96.
- Bodnar, R.J. and Vityk, M.O., 1994, Interpretation of microthermometric data for

- H₂O-NaCl fluid inclusions, *in* De Vivo, B. and Frazzotti, M.L. eds., Fluid inclusions in minerals: methods and applications, Short course of the working group (IMA) "Inclusions in Minerals" Pontignano, Italy. p. 117-130.
- Borisenko, A.S., 1977, Study of salt composition and solutions of gas-liquid inclusions in minerals by the cryometric method: *Geologiya i Geofizika*, v. 8, p. 16-27.
- Bowers, T.S. and Helgeson, H.C., 1983, Calculation of the thermodynamic and geochemical consequences of nonideal mixing in the system H₂O-CO₂-NaCl on phase relations in geologic systems: metamorphic equilibria at high pressures and temperatures: *American Mineralogist*, v. 68, p. 1059-1075.
- Bowman, J.R., 1998, Basic aspects and applications of phase equilibria in the analysis of metasomatic Ca-Mg-Al-Fe-Si skarns, *in* Lentz, D.R. ed., Mineralized intrusion-related skarn systems: Mineralogical Association of Canada Short course series, v. 26, p. 1-50.
- Brown, P.E., 1998, Fluid inclusion modeling for hydrothermal systems, *in* Richards, J.P. & Larson, P.B., eds., Techniques in Hydrothermal Ore Deposits Geology: Society of Economic Geology Reviews in Economic Geology, v. 10, p. 151-169.
- Brown, P.E. and Hagemann, S.G., 1995, MacFlinCor: A computer program for fluid inclusion data reduction and manipulation, *in* De Vivo, B. and Frazzotti, M.L. eds., Fluid inclusions in minerals: methods and

- applications, Short course of the working group (IMA) "Inclusions in Minerals" Pontignano, Italy. p. 231-250.
- Crawford, M.L., 1981, Phase equilibria in aqueous fluid inclusions: Mineralogical Association of Canada Short Course Handbook, v. 6, p. 75-100.
- Davis, D.W., Lowenstern, T.K., and Spencer, R.J., 1990, The melting behavior of fluid inclusions in laboratory-grown halite crystals in the systems NaCl-H₂O, NaCl-KCl-H₂O, NaCl-MgCl₂-H₂O, and NaCl-CaCl₂-H₂O: *Geochimica et Cosmochimica Acta*, v. 54, p. 591-601.
- Deer, W.A., Howie, R.A., and Zussman, J., 1992, An introduction to the rock-forming minerals: 2nd edition, Longman Group UK Limited, Essex, U.K., 696 p.
- de Cserna, Z., 1989, An outline of the Geology of Mexico, *in* Bally, A. W., and Palmer, A. R., eds., *The Geology of North America – An overview*: Boulder, Colorado, Geological Society of America, *The Geology of North America*, v. A.
- Drewes, H., 1991, Description and Development of the Cordilleran Orogenic Belt in the Southwestern United States and Northern Mexico: U.S. Geological Survey Professional Paper 1512, 87 p.
- Einaudi, M.T., Meinert, L.D., and Newberry, R.J., 1981, Skarn Deposits, *in* Skinner, B.J., ed., *Economic Geology 75th Anniversary Volume: Economic Geology Publishing Company*, El Paso, Texas, p. 317-391.
- Graf, A., 1997, Geology and porphyry-style mineralization of the Cerro de la Gloria

- stock associated with high-T, carbonate-hosted Zn-Cu-Ag(-Pb) skarn mineralization, San Martin District, Zacatecas, Mexico: Unpublished M.Sc. Thesis, University of Arizona, 154 p.
- Henley, R.W., Truesdell, A.H., Barton, P.B., and Whitney, J.A., 1984, Fluid-mineral equilibria in hydrothermal systems: Society of Economic Geologists, Reviews in Economic Geology, v. 1, 267 p.
- James, E.W. and Henry, C.D., 1993, Pb isotopes of ore deposits in Trans-Pecos Texas and northeastern Chihuahua, Mexico: Basement, igneous, and sedimentary sources of metals: Econ. Geol., v. 88, p. 934-947.
- Johnson, J.W. and Norton, D.L., 1985, Theoretical prediction of hydrothermal conditions and chemical equilibria during skarn formation in porphyry copper systems: Economic Geology, v. 80, p. 1797-1823.
- Kretz, R., 1983, Symbols for rock-forming minerals: American Mineralogist, v. 68, p. 277-279.
- Longoria, J.F., Clowes, D.M., and Monreal, R., 1999, Type Mesozoic succession of northern Mexico: Canon La Casita, *in* Bartolini, C., Wilson, J.L., and Lawton, T.F., eds., Mesozoic sedimentary and Tectonic History of North-Central Mexico: Boulder Colorado, Geological Society of America Special Paper 340, p. 287-318.
- McClay, K.R., 1987, The Mapping of Geological Structures, John Wiley and Sons, West Sussex, England, 161 p.
- Megaw, P.K.M., 1999, The high-temperature, Ag-Pb-Zn-(Cu) carbonate-replacement deposits of central Mexico *in* Jambor, J.L., ed., VMS and

- carbonate-hosted polymetallic deposits of central Mexico; Cordilleran Roundup, 1999, p. 81-84.
- Megaw, P.K.M., Barton, M.D., and Falce, J.I., 1996, Carbonate-hosted lead-zinc (Ag, Cu, Au) deposits of northern Chihuahua, Mexico, In D.F. Sangster, ed., Carbonate-hosted Lead-Zinc Deposits: Society of Economic Geologists Special Publication Number 4, p. 277-289.
- Meinert, L.D., 1989, Gold skarn deposits – Geology and Exploration Criteria, In R.R. Keays, W.R.H. Ramsay, & D.I. Groves, eds., The Geology of Gold Deposits: Economic geology monograph 6, Society of Economic Geologists, p. 537-552.
- Meinert, L.D., 1992, Skarns and Skarn deposits, Geoscience Canada, v. 19, p. 145-162.
- Meinert, L.D., 1997, Application of skarn zonation models to mineral exploration: Exploration and Mining Geology, v. 6, no. 2, p. 185-208.
- Patterson, K.M., Rowins, S.M., Mortensen, J.K., and Terry, D.A., in review, Controls on the distribution of polymetallic skarn mineralization by pre- and syn-intrusion deformation at Cerro el Sacrificio, Durango, Mexico: Economic Geology.
- Philpotts, A.R., 1990, Principals of igneous and metamorphic petrology, Prentice Hall, New Jersey, 498 p.
- Pichavant, M., Ramboz, C., and Weisbrod, A., 1982, Fluid immiscibility in natural processes: Use and misuse part 1: Phase equilibria analysis – A theoretical and geometrical approach: Chemical Geology, v. 37, p. 1-27.

- Potter, R.W., 1977, Pressure corrections for fluid-inclusion homogenization temperatures based on the volumetric properties of the system NaCl-H₂O: Journal of Research of the United States Geological Survey, v. 5, no. 5, p. 603-607.
- Richards, J.P., McCulloch, M.T., Chappell, B.W., and Kerrich, R., 1991, Sources of metals in the Porgera gold deposit, Papua New Guinea: Evidence from alteration, isotope and noble gas geochemistry: *Geochimica et Cosmochimica Acta*, v. 55, p. 565-580.
- Rickwood, P.C., 1968, On recasting analyses of garnet into end-member molecules: *Contributions to Mineralogy and Petrology*, v. 18, p.175-198.
- Roedder, E., 1984, Fluid Inclusions. *Reviews in Mineralogy: Mineralogical Society of America*, v.12, 646 p.
- Rowins, S.M., Groves, D.I., McNaughton, N.J., Palmer, M., and Eldridge, C.S., 1997, A reinterpretation of the role of granitoids in the genesis of Neoproterozoic gold mineralization in the Telfer Dome, Western Australia: *Economic Geology*, v. 92, p. 133-160
- Rubin, J.N., 1986, Mineralogy and Ore Genesis at the San Martin Mine, Zacatecas, Mexico: Unpublished M.Sc. Thesis, The University of Texas at Austin, 97 p.
- Rubin, J. N. and Kyle, J. R., 1988, Mineralogy and geochemistry of the San Martin skarn deposit, Zacatecas, Mexico: *Economic Geology*, v. 83, p. 1782-1801.
- Sedlock, R. L., Ortega-Gutierrez, F., and Speed, R. C., 1993,

- Tectonostratigraphic terranes and tectonic evolution of Mexico: Boulder, Colorado, Geological Society of America Special Paper 278.
- Shepherd, T.J., Rankin, A.H., and Alderton, D.H.M., 1985, A Practical Guide to Fluid Inclusion Studies: Blackie, London, U.K., 239 p.
- Shoji, T., 1975, Role of temperature and CO₂ pressure in the formation of skarn and its bearing on mineralization: *Economic Geology*, v. 70, p. 739-749.
- Sutter, M., 1987, Structural traverse across the Sierra Madre Oriental fold-thrust belt in east-central Mexico: *Geological Society of America Bulletin*, v. 98, p. 249-264.
- Terry, D.A., Patterson, K.P., Warman, T., and Gibson, K., 1999, Report on diamond drilling, geological mapping, and geophysical surveys carried out on the Cerro Sacrificio project, Durango state, Mexico (November 1998 to July 1999): Boliden Limited, Unpublished report, 49 p.
- Tosdal, R. M., Wooden, J. L., and Bouse, R. M., 1999, Pb Isotopes, Ore Deposits, and Metallogenic Terranes *In* Lambert, D.D. and Ruiz, J. eds., *Application of Radiometric Isotopes to Ore Deposit Research and Exploration*, Society of Economic Geologists, *Reviews in Economic Geology*, v. 12, p. 1-28.
- Turcotte, D.L. and Schubert, G., 1982, *Geodynamics*, John Wiley and Sons, New York, 450 p.
- Zartman, R.E. and Doe, B.R., 1981, Plumbotectonics – the model: *Tectonophysics*, v. 75, p. 135-162.

Figure Captions

Figure 18. Location map for the Sacrificio deposit, Durango State, Mexico. Solid squares and circles represent major cities and significant mineral deposits in the region, respectively.

Figure 19. Simplified geological map of the Sacrificio property. Heavy dashed line is the approximate subsurface extent of the Sacrificio intrusion inferred from geophysical and drillhole data (Terry et al., 1999). Solid squares are sites of previous mining activity (after Patterson et al., *in review*).

Figure 20. Examples of the main styles of mineralization in the Sacrificio deposit. A. Disseminated Cu-Ag mineralization. Photomicrograph of prograde garnet skarn with bornite (Bn) and chalcopyrite (Ccp) filling intermineral porosity between euhedral crystals of garnet (Grt). B. Fracture-controlled Cu-Ag \pm Au mineralization. Historic adit exploiting an east-northeast-striking vein (filled D₅ fracture). Dashed line marks the boundary between the vein and the disseminated sulfide mineralization in prograde garnet skarn. C. Drillhole intersection of massive polymetallic manto showing contact with marble.

Figure 21. Surface distribution of skarn alteration and related sulfide mineralization at the Sacrificio deposit (after Patterson et al., *in review*). Garnet skarn and disseminated bornite-chalcopyrite mineralization are strongly controlled by D₃ fold axial planes and their intersections with major and minor D₅ fracture sets. Only the major fracture sets and folds are shown. Note the localization of most skarn alteration and mineralization above the intrusion rather than around the margins as is typical of many skarn deposits (Meinert, 1997).

Figure 22. Photomicrographs of common skarn minerals from the Sacrificio deposit. A. Optically and compositionally zoned crystal of grandite garnet in prograde skarn. B. Subhedral clinopyroxene (Cpx) and euhedral garnet (Grt) crystals in prograde skarn. C. Mass of medium-grained, euhedral hornblende crystals in retrograde skarn. D. Retrograde amphibole (Amp) skarn replacing garnet (Grt) - wollastonite (Wo) prograde skarn and marble (Mb).

Figure 23. Mol. % iron versus mol. % aluminum in grandite garnets from prograde skarn. Analyses show an almost perfect 1:1 substitution (correlation coefficient, $r^2=0.995$) between iron and aluminum in the octahedral site. High iron values correspond to high mol. % andradite, whereas high aluminum values correspond to high mol. % grossular.

Figure 24. Ternary diagrams of garnet (Gr-Ad-Sp+Al) and pyroxene (Di-Hd-Jo) compositions from the Sacrificio deposit. Circles are individual analyses. Shaded fields indicate typical garnet and pyroxene compositions from Zn (Pb), Fe, and Cu skarns (after Meinert, 1992). Abbreviations for garnet end-members are as follows: Gr = grossular, Ad = andradite, Sp = spessartine, Al = almandine, Di = diopside, Hd = hedenbergite, Jo = johannsenite. See text for further discussion.

Figure 25. Interpreted sequence of deformation events affecting Cerro el Sacrificio (after Patterson et al., *in review*). D1 – Tight to isoclinal, west-verging, recumbent folds. D2 – Type 2 refolding of D₁ folds. D3 – Large amplitude, gentle to open, upright folds trending 330° that refold D₁ and D₂ folds. D4 – Doming of previously deformed strata over the intrusion during its emplacement, with

exsolved magmatic fluids focused along D_3 axial surfaces. D_5 – Increase in pore fluid pressure above the intrusion and opening of mode 1 fractures oriented east-northeast, parallel to maximum compressive stress. Mineralizing fluids are channeled by these fractures with bornite and chalcopyrite filling secondary porosity in garnet skarn proximal to the D_5 fractures. The formation of retrograde skarn and mantos postdate D_5 and are not included in this schematic diagram.

Figure 26. Relative timing of deformation, alteration, and mineralization events at the Sacrificio deposit. Absolute ages are derived from U-Pb dating of intrusive rocks; all other timing is relative, i.e. the time axis is not to scale (after Patterson et al., *in review*).

Figure 27. Fluid inclusion microphotographs. A. Fluid inclusions in quartz associated with disseminated Cu-Ag mineralization. Note rare carbonate daughter mineral. B. Fluid inclusions in quartz associated with polymetallic manto mineralization. C. Fluid inclusions in quartz in quartz-arsenopyrite veins.

Figure 28. Microthermometric fluid inclusion data for the Sacrificio deposit. A. Eutectic temperatures from disseminated mineralization. B. Eutectic temperatures from manto mineralization. C. Eutectic temperatures from quartz-arsenopyrite veins. D. Fluid salinities (in wt.% NaCl eq.) calculated from final ice melting temperatures in disseminated mineralization. E. Fluid salinities (in wt.% NaCl eq.) calculated from final ice melting temperatures in manto mineralization. F. Fluid salinities (in wt.% NaCl eq.) calculated from final ice melting temperatures in quartz-arsenopyrite veins. G. Temperatures of homogenization (to liquid) for fluid inclusions in disseminated mineralization. H. Temperatures of

homogenization (to liquid) for fluid inclusions in manto mineralization. I. Temperatures of homogenization (to liquid) for fluid inclusions in quartz-arsenopyrite veins.

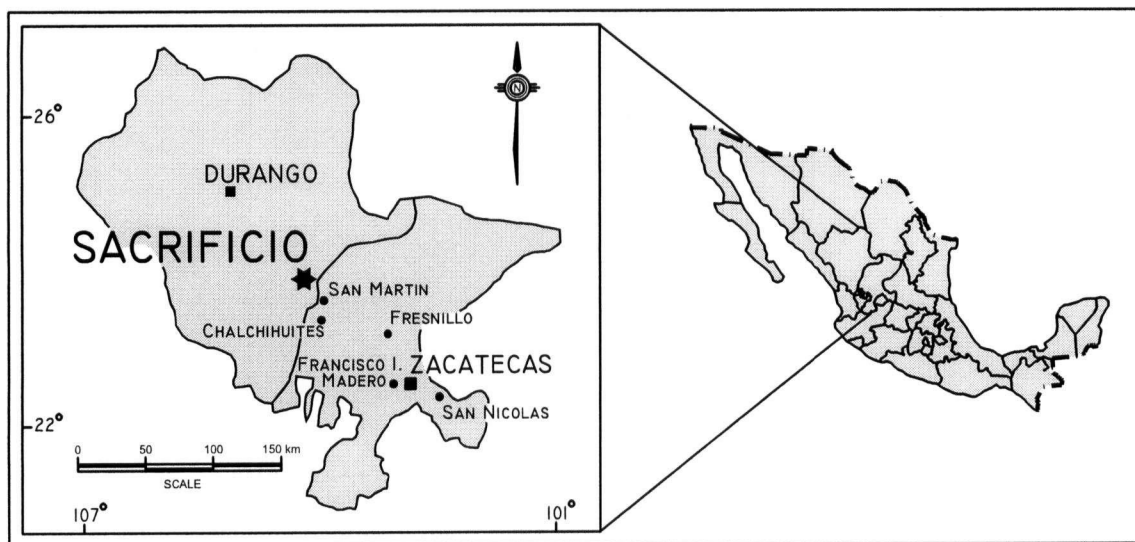
Figure 29. Trapping temperatures of manto (247° to 396°C; light shaded field, overlapping with dark shaded field) and disseminated (291° to 504°C; dark shaded field) mineralization at pressures of 0.5 to 1.0 kbar and fluid salinities of 5 wt % NaCl eq. The trapping temperatures are obtained from projection along isochores corresponding to the homogenization temperatures of the disseminated (251° to 389°C) and manto (205° to 306°C) styles of mineralization, respectively (Table 6). Figure modified from Bodnar and Vityk (1994).

Figure 30. Trapping temperatures of arsenopyrite-quartz veins (318° to 480°C; shaded field) at pressures of 0.5 to 1.0 kbar and a salinity of 10 wt.% NaCl eq. The trapping temperatures are obtained from projection along isochores corresponding to the homogenization temperatures (278° to 383°C) of the veins (Table 6). Figure modified from Bodnar and Vityk (1994).

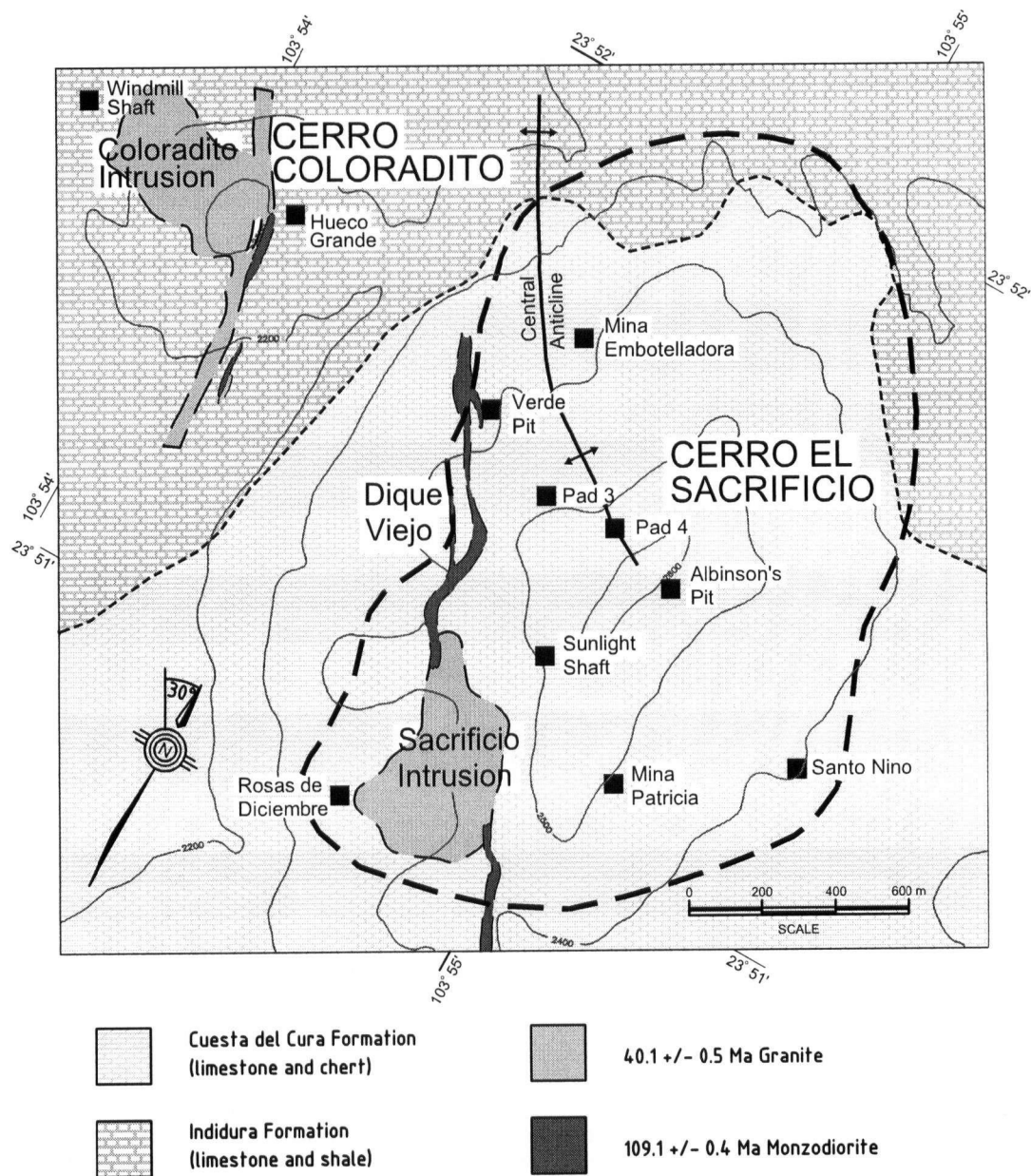
Figure 31. Lead isotope data for sulfide mineralization and host-rocks from the Sacrificio deposit. A. $^{208}\text{Pb}/^{206}\text{Pb}$ vs. $^{207}\text{Pb}/^{206}\text{Pb}$. B. $^{207}\text{Pb}/^{204}\text{Pb}$ vs. $^{206}\text{Pb}/^{204}\text{Pb}$. C. $^{208}\text{Pb}/^{204}\text{Pb}$ vs. $^{206}\text{Pb}/^{204}\text{Pb}$. Symbols used in the diagrams are as follows: Diamonds = fracture-controlled mineralization; triangles = quartz-arsenopyrite veins; squares = manto mineralization; open circles = disseminated mineralization; vertical crosses = intrusive rocks; and inclined crosses = sedimentary host-rocks. Filled circles and associated trend-lines are the upper crust and orogene growth curves of Zartman and Doe (1981).

Figure 32. Pressure-temperature stability of wollastonite in H₂O-rich fluid with X(CO₂) of 0.1 (modified after Bowman, 1998). The presence of wollastonite in prograde skarn formed at pressures of 0.5 to 1.0 kbar gives minimum temperatures of prograde skarn formation between 460° to 510° C.

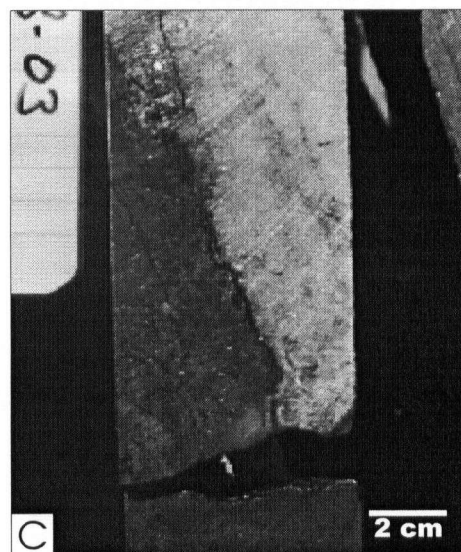
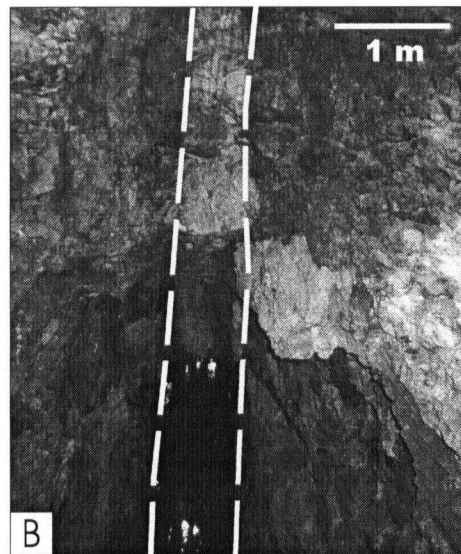
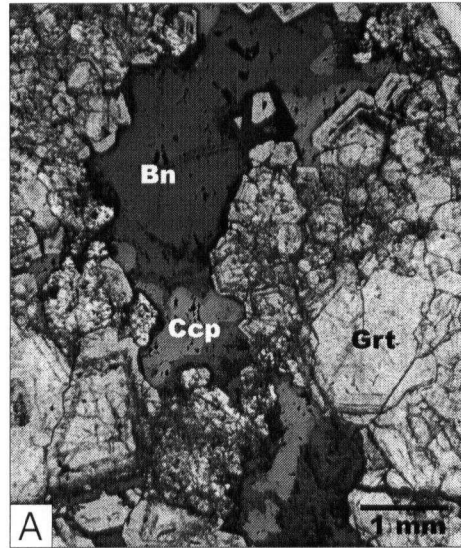
Figure 33. Temporal evolution of temperature in the Sacrificio skarn system. Dashed and solid lines are fluid trapping temperatures calculated at 0.5 and 1.0 kbar, respectively (minimum and maximum pressures estimated for skarn formation and related mineralization at Sacrificio). Note the cooling trend from prograde skarn to manto mineralization, whereupon a reversal occurs with the formation of post-skarn quartz-arsenopyrite veins. See text for further discussion.



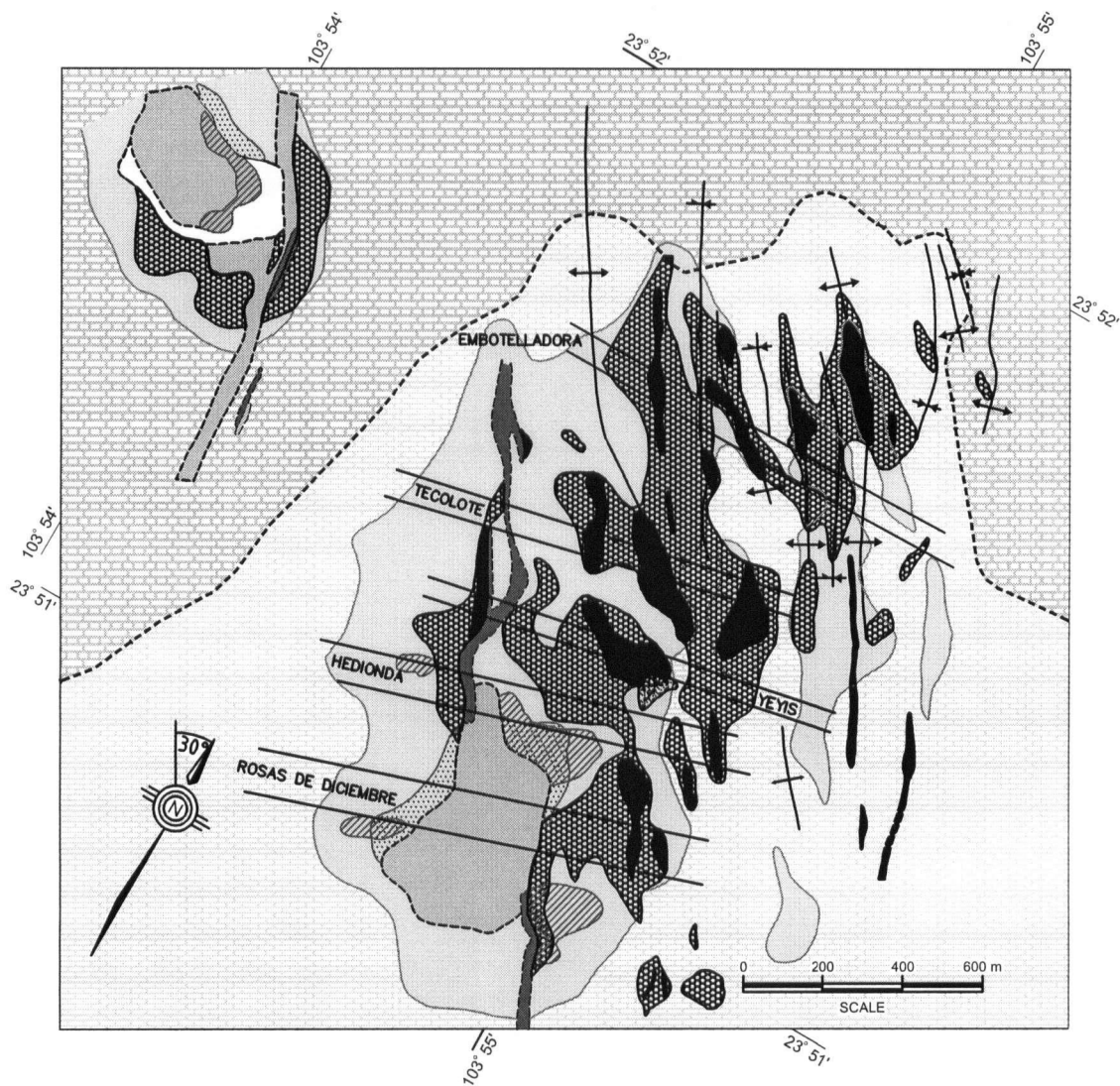
Patterson and Rowins: Figure 18



Patterson and Rowins: Figure 19



Patterson and Rowins: Figure 20



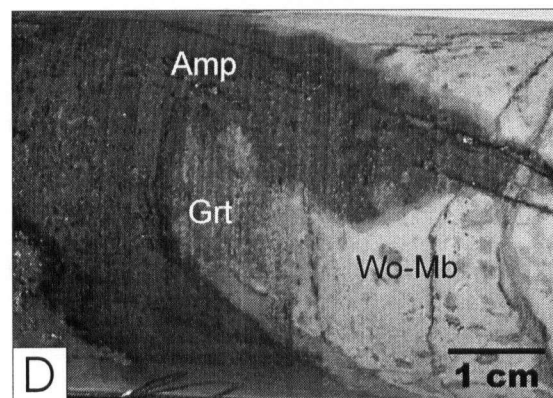
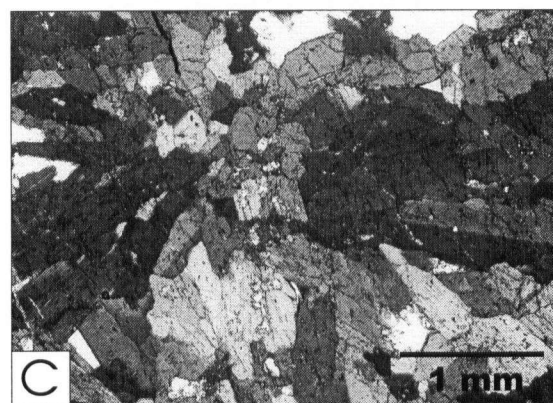
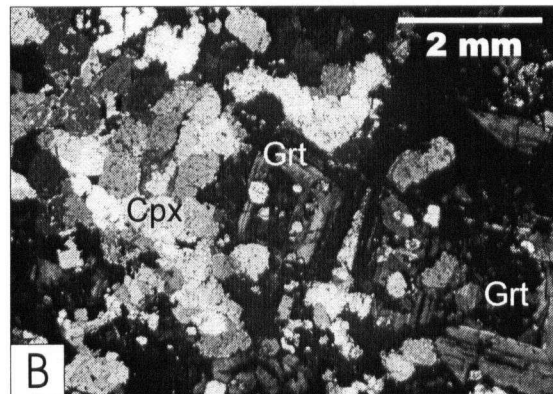
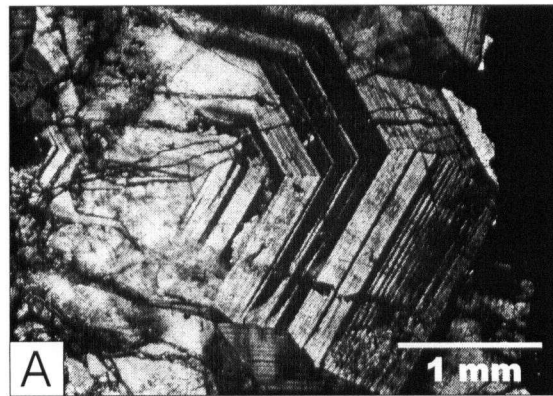
Lithologic Units

- Cuesta del Cura Formation (limestone and chert)
- Indidura Formation (limestone and shale)
- 40.1 +/- 0.5 Ma Granite
- 109 Ma Monzodiorite
- Approximate boundary of mineralized fracture set
- Mapped contact between the Cuesta del Cura and Indidura Formations

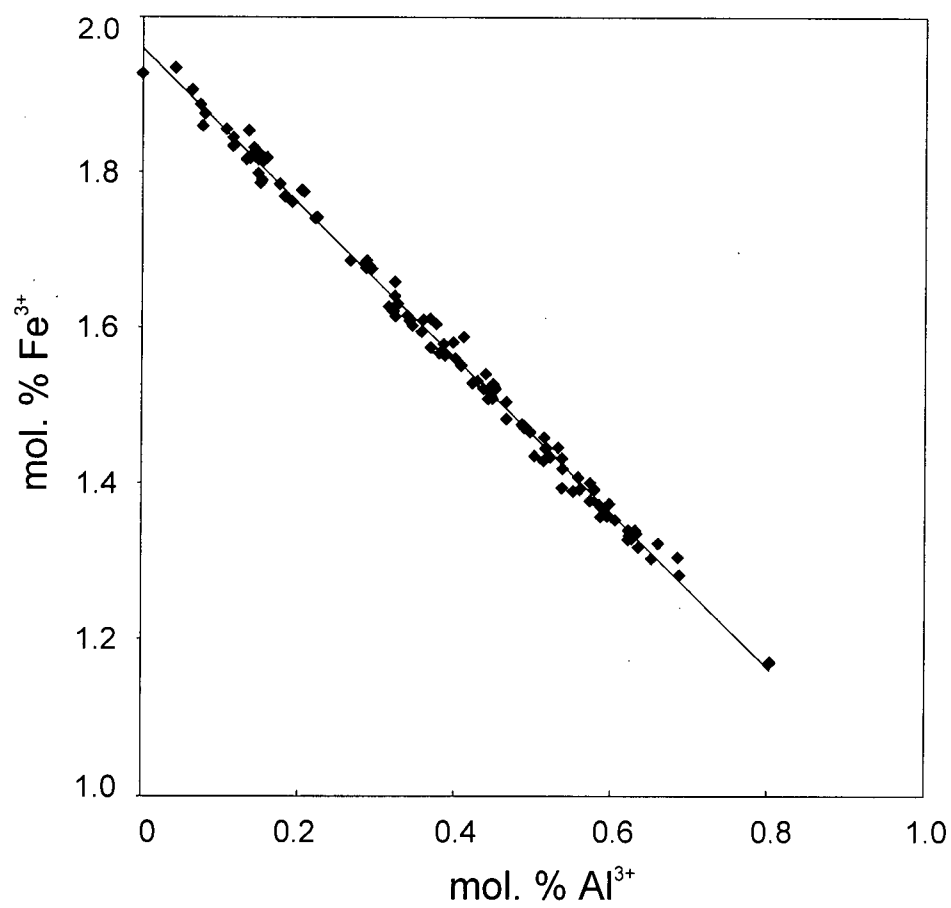
Alteration and Related Mineralization

- Hornfels**
 - Quartz-Scapolite-Albite +/- Sericite
- Prograde Skarn**
 - Garnet Skarn
 - Disseminated Bornite-Chalcopyrite and Fracture-Controlled Mineralization
 - Intense Silicification
 - Quartz Vein Stockwork
 - Quartz-Cemented Limestone Breccia
- Retrograde Skarn**
 - Pervasive Amphibole-Chlorite +/- Base and Precious Metal Mantos

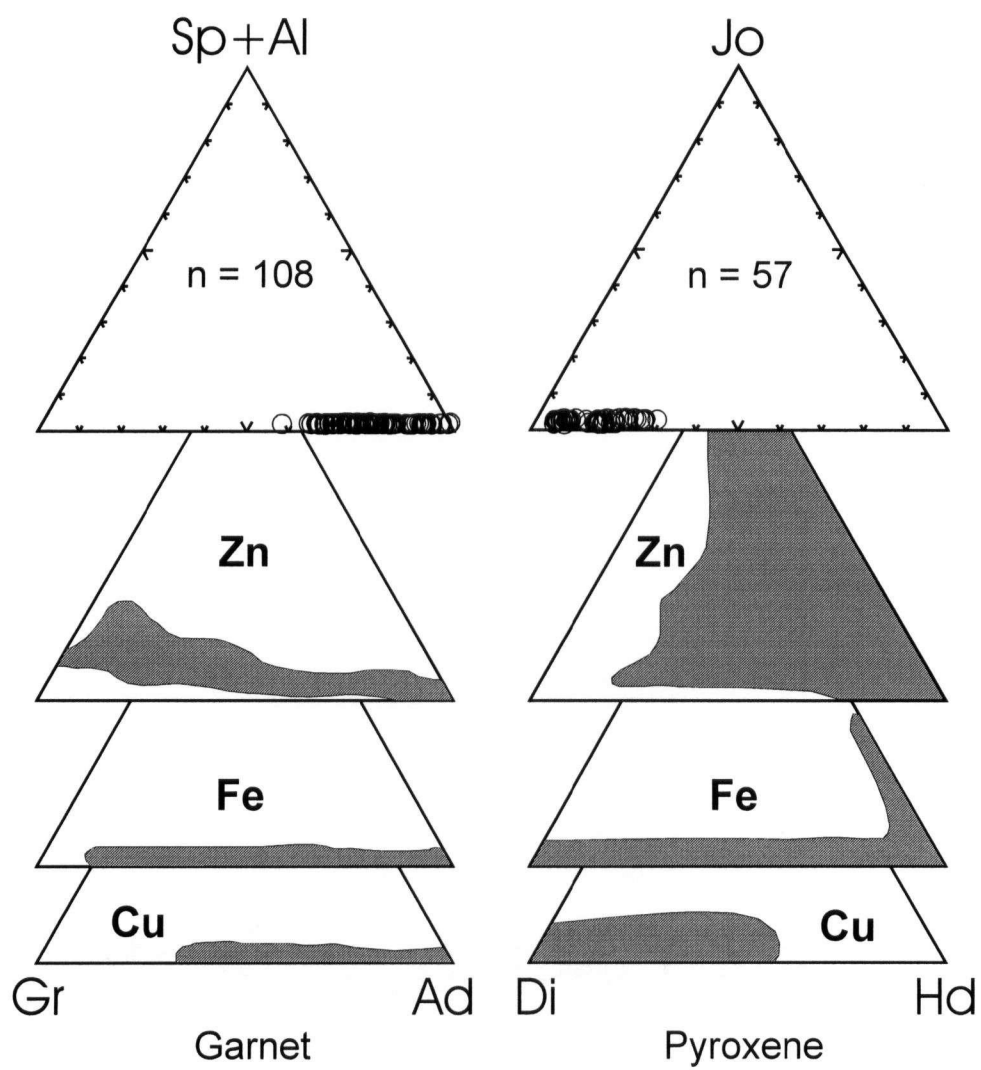
Patterson and Rowins: Figure 21



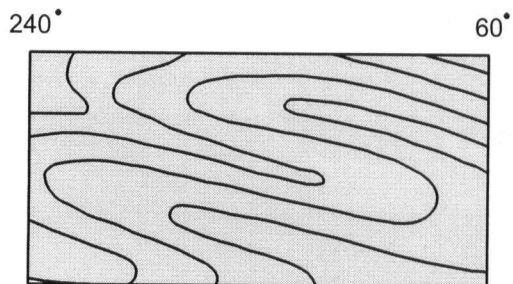
Patterson and Rowins: Figure 22



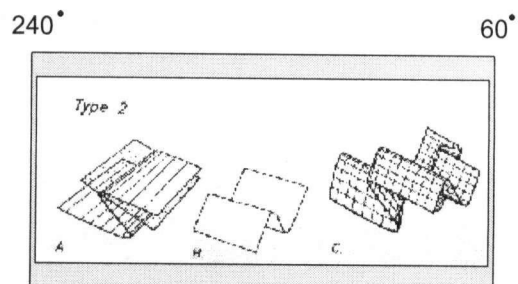
Patterson and Rowins: Figure 23



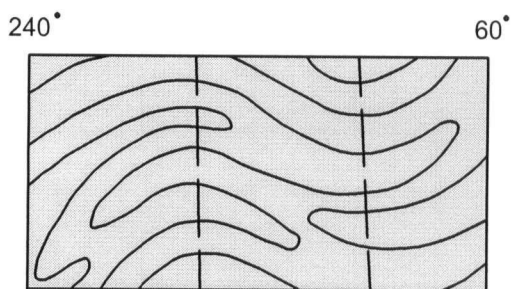
Patterson and Rowins: Figure 24



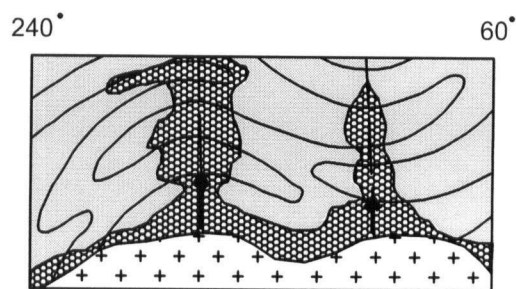
D1



D2

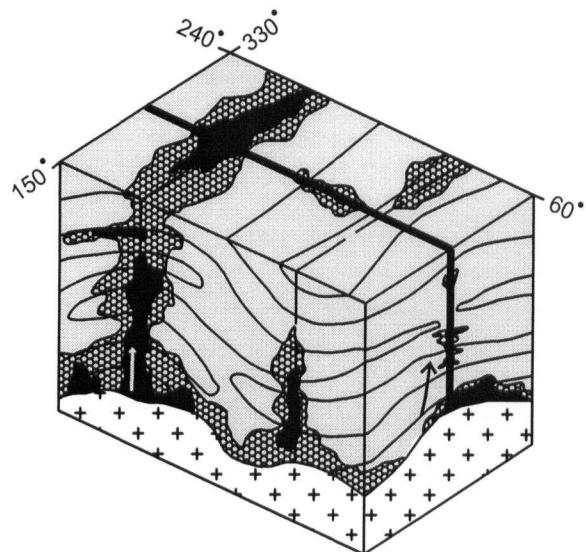


D3



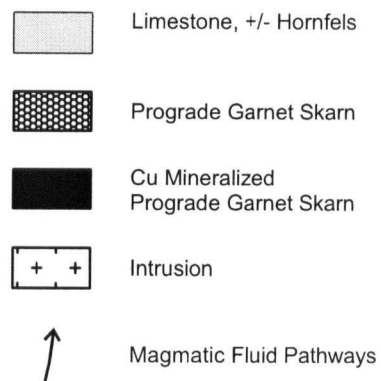
Intrusion, doming over pluton,
and garnet skarn

D4

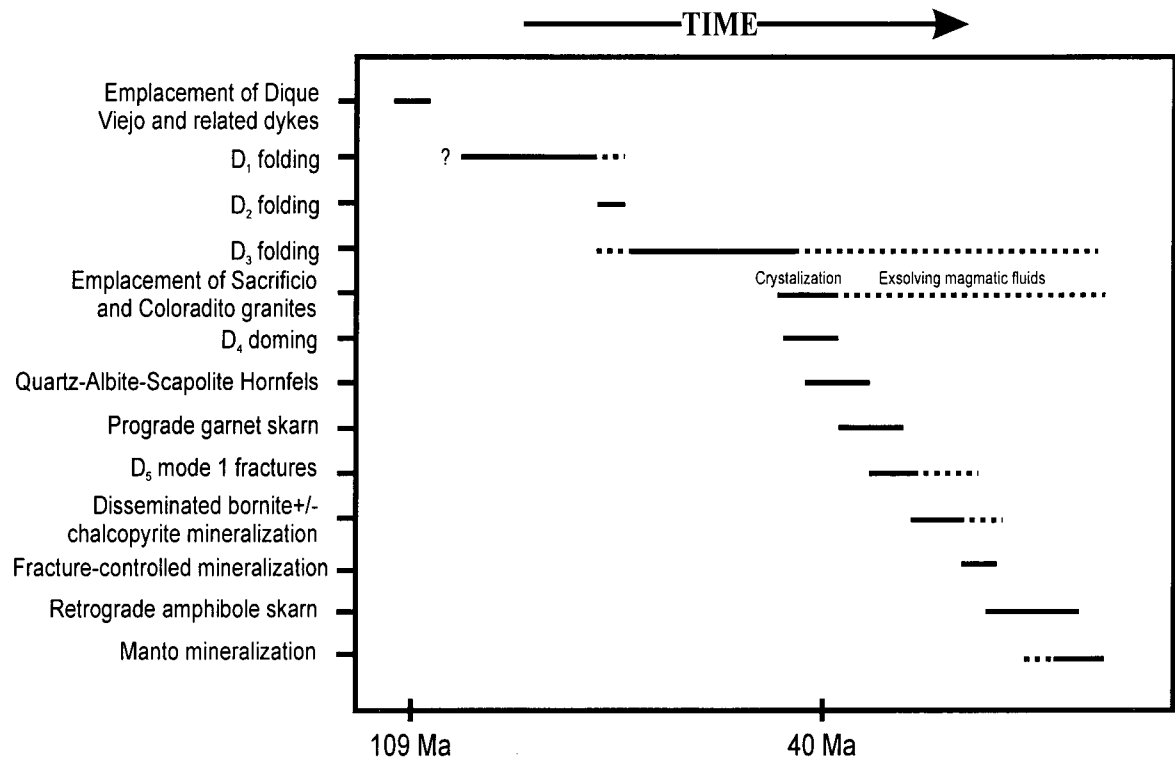


Opening of extensional fractures,
fluids channeled up fractures

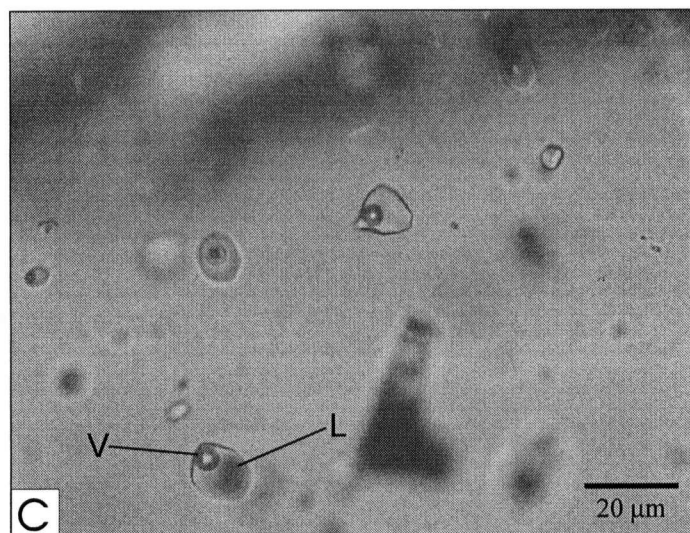
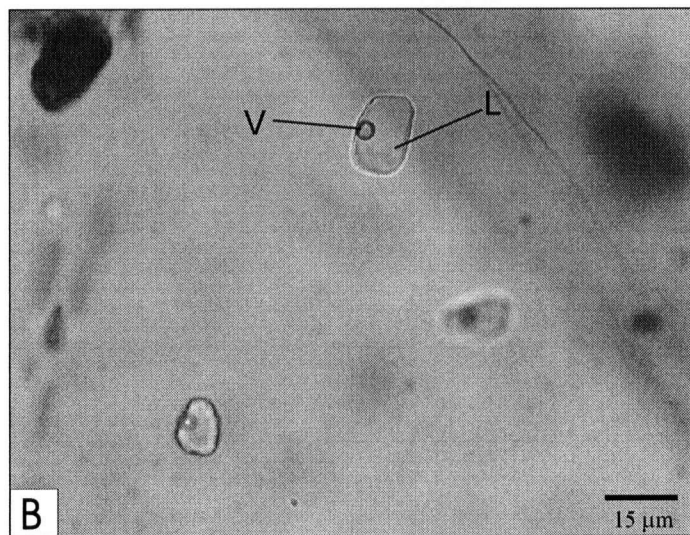
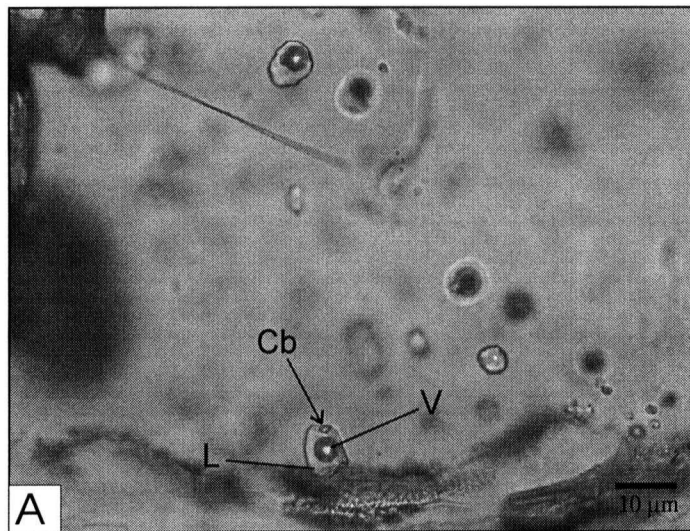
D5



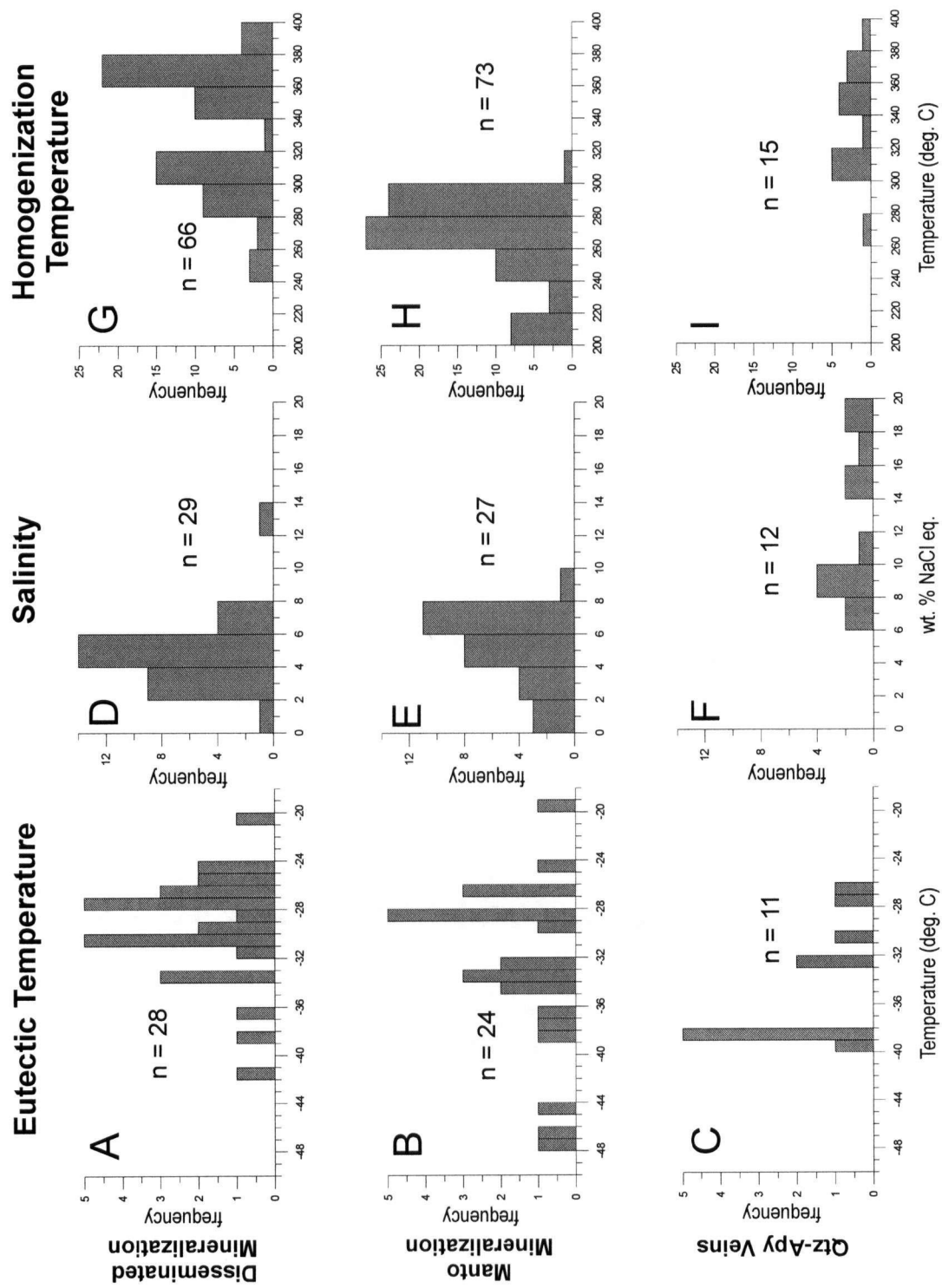
Patterson and Rowins: Figure 25



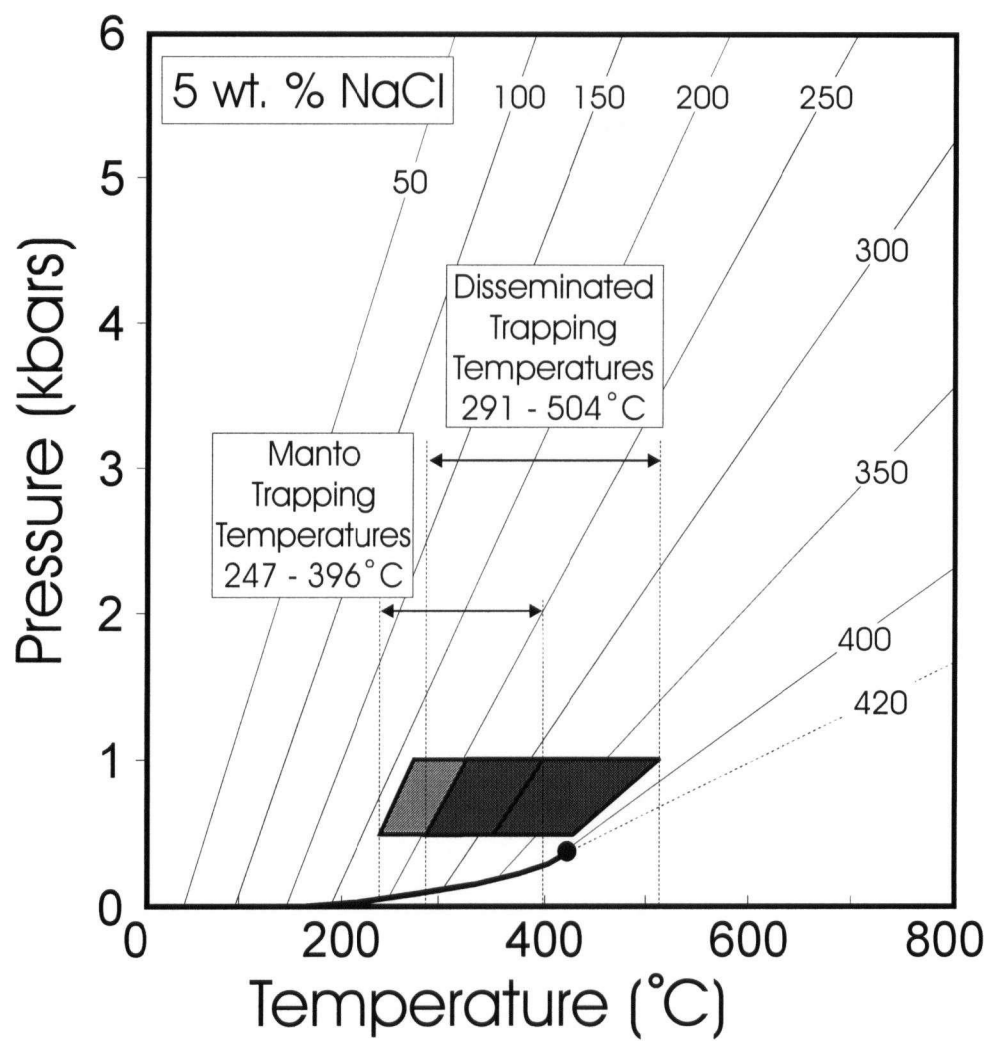
Patterson and Rowins: Figure 26



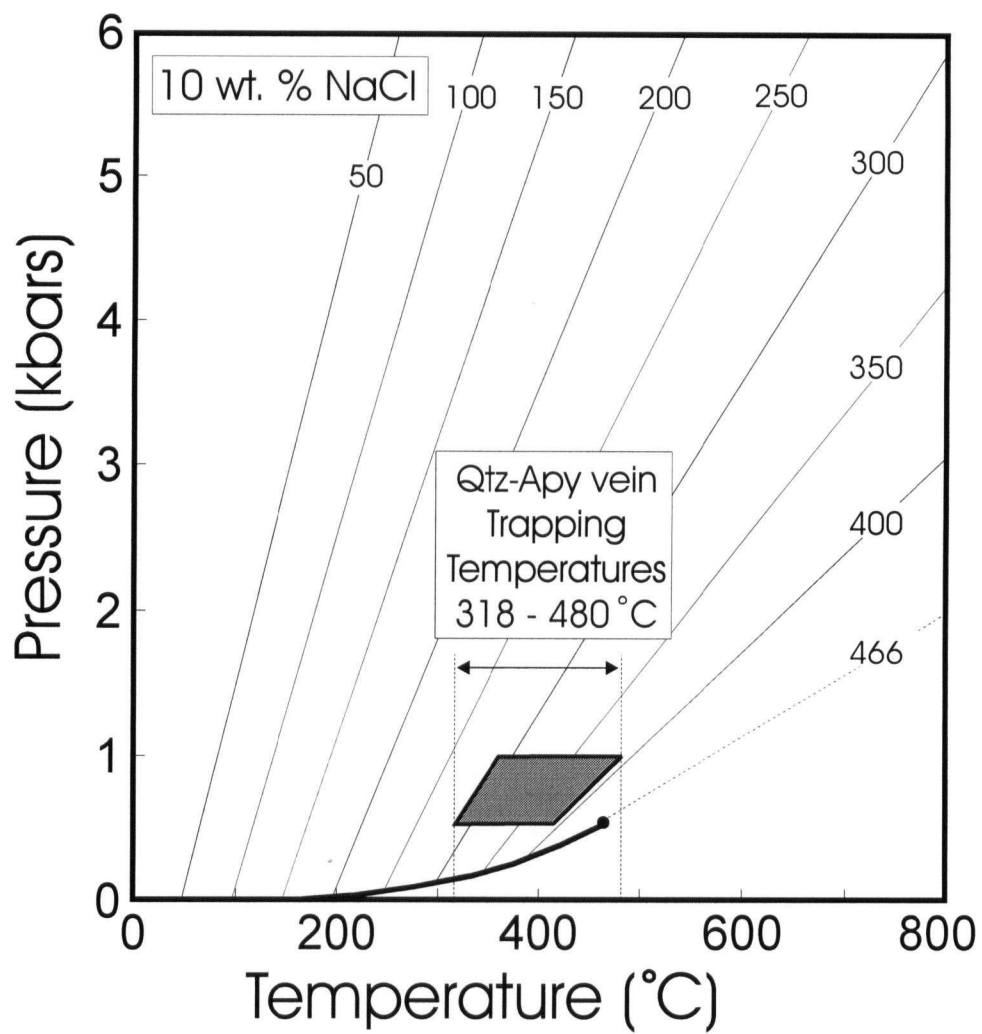
Patterson and Rowins: Figure 27



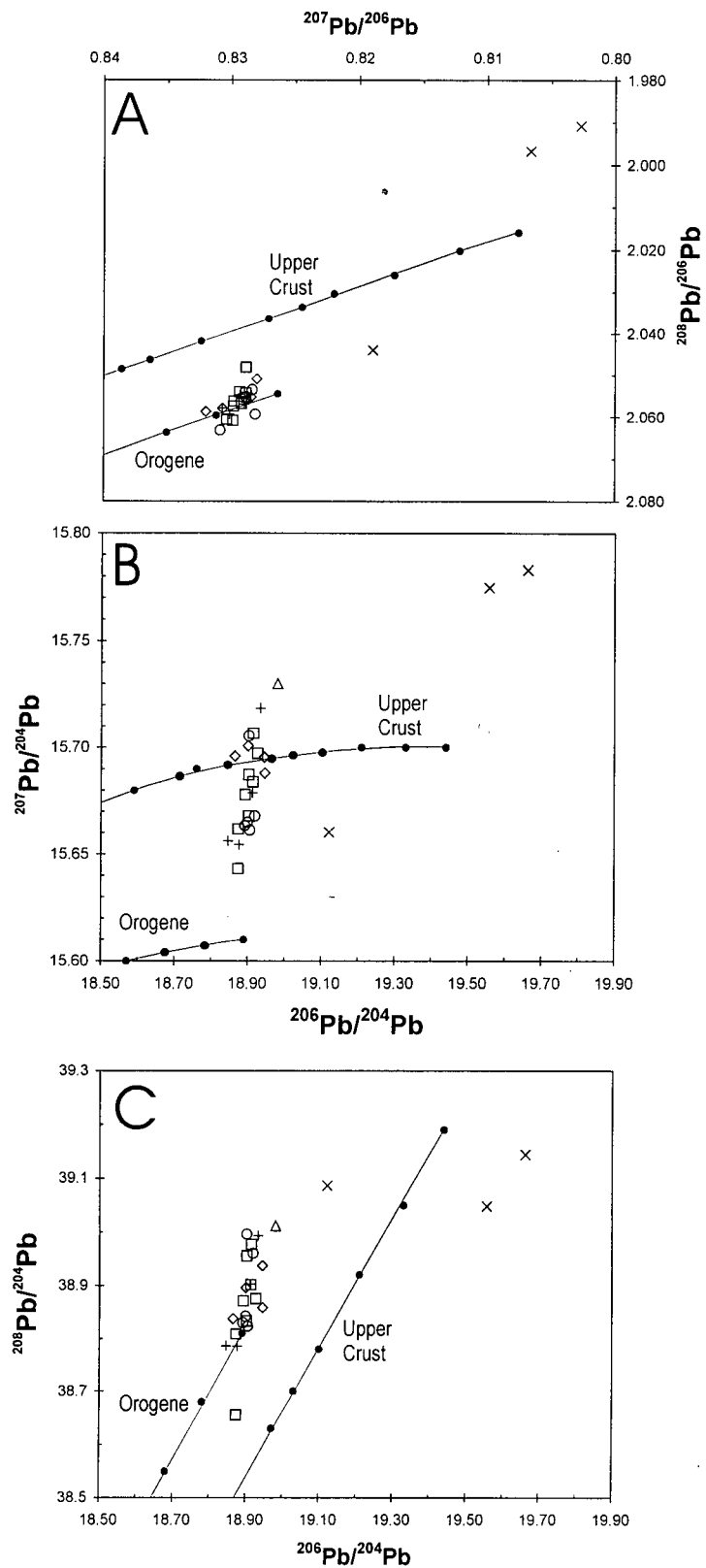
Patterson and Rowins: Figure 28



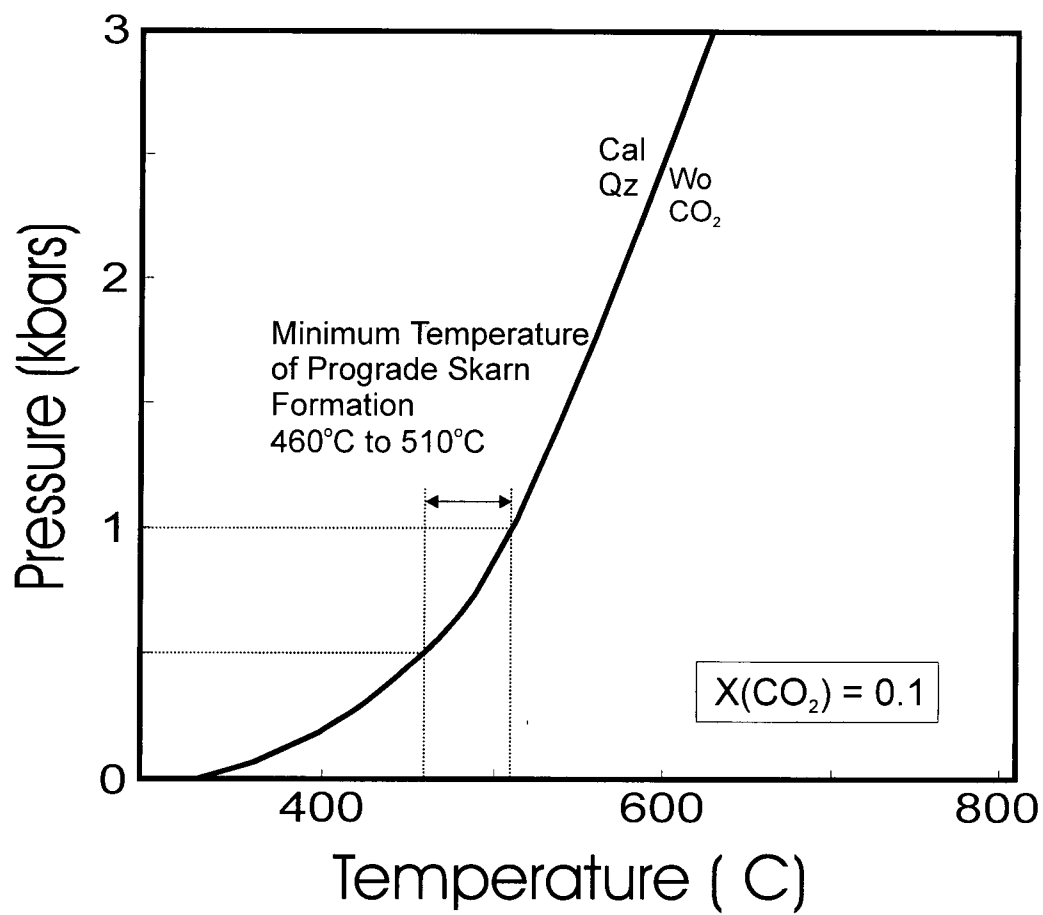
Patterson and Rowins: Figure 29



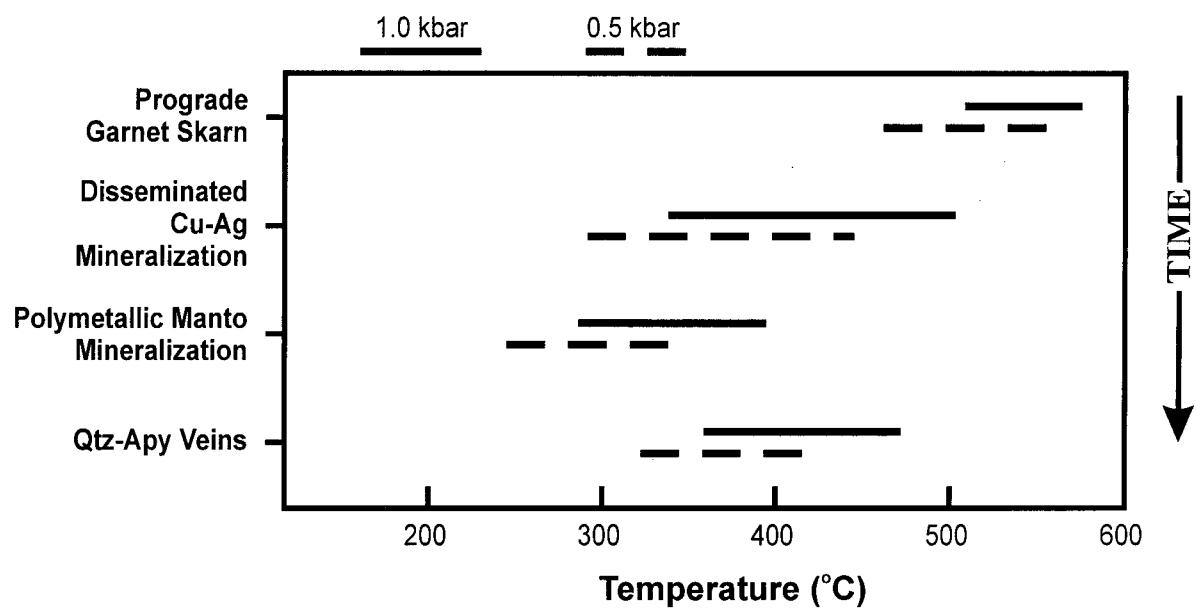
Patterson and Rowins: Figure 30



Patterson and Rowins: Figure 31



Patterson and Rowins: Figure 32



Patterson and Rowins: Figure 33

Table 4. Paragenesis of Alteration and Mineralization at the Sacrificio Deposit

TIME ↓	Alteration		Mineralization	
	<u>Style</u>	<u>Mineralogy</u>	<u>Style</u>	<u>Mineralogy</u>
	Contact Metamorphism	quartz-albite-scapolite ± sericite ± chlorite	None	None
	Prograde Skarn	garnet-wollastonite- clinopyroxene- vesuvianite	Disseminated Cu-Ag	bornite ± chalcopyrite
	Minor Silicification	quartz	Fracture-controlled Cu-Ag±Au	chalcopyrite ± bornite ± sphalerite ± galena ± arsenopyrite
	Retrograde Skarn	amphibole-chlorite ± epidote ± calcite	Massive Manto Zn-Cu-Pb-Ag±Au	sphalerite-galena- chalcopyrite- arsenopyrite-pyrite- pyrrhotite-bornite

Note: only major minerals are listed; secondary copper-oxide minerals are variably developed near surface in all styles of mineralization.

Table 5. Representative Microprobe Analyses of Garnets and Pyroxenes from Prograde Skarn

Analysis no.	Garnet								Pyroxene			
	kp-40a	kp-40b	kp-41a	kp-41b	kp-47a	kp-47b	kp-48a	kp-48b	kp-47c	kp-47d	kp-48c	kp-48d
SiO ₂	35.14	35.93	34.86	35.74	35.63	36.02	35.76	36.34	53.28	53.94	52.62	54.43
TiO ₂	0.00	0.06	0.00	0.06	0.01	0.27	0.05	0.10	0.04	0.00	0.01	0.00
Al ₂ O ₃	1.65	6.37	1.44	5.34	4.05	7.53	3.47	6.43	0.03	0.09	0.03	0.05
Cr ₂ O ₃	0.00	0.01	0.02	0.00	0.00	0.00	0.01	0.00	0.02	0.00	0.00	0.02
FeO									5.95	3.21	8.97	2.15
Fe ₂ O ₃ ⁽¹⁾	28.55	22.50	28.94	23.58	25.37	20.59	25.38	21.86				
MnO	0.09	0.09	0.16	0.10	0.12	0.16	0.08	0.15	0.77	0.58	0.69	0.59
MgO	0.08	0.08	0.06	0.08	0.10	0.13	0.11	0.22	14.34	16.26	12.52	17.06
CaO	34.04	35.04	33.53	34.73	33.65	34.25	33.63	33.78	25.08	25.67	25.15	25.65
Na ₂ O	0.01	0.00	0.00	0.00	0.02	0.01	0.00	0.01	0.04	0.00	0.04	0.01
total	99.54	100.07	99.02	99.63	98.94	98.95	98.47	98.89	99.54	99.74	100.03	99.96
Number of cations on the basis of 8 oxygens								Number of cations on the basis of 4 oxygens				
Si	2.95	2.93	2.95	2.94	2.97	2.95	3.00	2.99	1.99	1.98	1.98	1.98
Ti	0.00	0.00	0.00	0.00	0.00	0.02	0.00	0.01	0.00	0.00	0.00	0.00
Al	0.16	0.61	0.14	0.52	0.40	0.73	0.34	0.62	0.00	0.00	0.00	0.00
Cr	0.00	0.00	0.00	0.00	0.00	0.00	0.00	0.00	0.00	0.00	0.00	0.00
Fe ³⁺ ⁽²⁾	1.81	1.38	1.84	1.46	1.59	1.27	1.60	1.36	0.03	0.04	0.05	0.03
Fe ²⁺	0.00	0.00	0.00	0.00	0.00	0.00	0.00	0.00	0.16	0.06	0.24	0.04
Mn	0.01	0.01	0.01	0.01	0.01	0.01	0.01	0.01	0.02	0.02	0.02	0.02
Mg	0.01	0.01	0.01	0.01	0.01	0.02	0.01	0.03	0.80	0.89	0.70	0.93
Ca	3.06	3.06	3.04	3.06	3.01	3.01	3.03	2.98	1.00	1.01	1.01	1.00
Na	0.00	0.00	0.00	0.00	0.00	0.00	0.00	0.00	0.00	0.00	0.00	0.00
total	8.00	8.00	8.00	8.00	8.00	8.00	8.00	8.00	4.00	4.00	4.00	4.00
Endmembers (mol %)												
Andradite ⁽³⁾	91.71	70.69	93.70	74.46	80.39	64.53	82.36	68.44	80.18	89.90	71.24	92.979 Diopside ⁽⁴⁾
Grossularite	7.75	28.75	5.57	24.95	18.90	34.55	16.97	30.31	17.40	8.28	26.52	5.216 Hedenbergite
Spessartine	0.21	0.22	0.39	0.24	0.28	0.37	0.19	0.34	2.41	1.82	2.24	1.805 Johannsenite
Almandine	0.00	0.00	0.00	0.00	0.00	0.00	0.00	0.00				
Pyrope	0.33	0.32	0.27	0.34	0.43	0.55	0.45	0.90				
Uvarovite	0.00	0.02	0.06	0.01	0.00	0.00	0.03	0.01				

Microprobe analyses on CAMECA SX-50 microprobe, University of British Columbia. Operating conditions: excitation voltage, 15 kV; beam current, 20 nA; peak-count time, 20 s; background count time, 10 s; beam diameter, 5 μ m. Standards used in pyroxene analysis: diopside, MgK α , SiK α , TAP; diopside, CaK α , PET; rutile, TiK α , PET; synthetic Fe₂SiO₄, FeK α , LIF; synthetic MgCr₂O₄, CrK α , LIF; synthetic MnSiO₃, MnK α , LIF; albite, NaK α , TAP; kaersutite, AlK α , TAP. Standards used in garnet analysis: almandine, MgK α , SiK α , TAP; almandine, Fe K α , LIF; grossular, CaK α , PET; grossular, AlK α , TAP; rutile, TiK α , PET; synthetic MgCr₂O₄, CrK α , LIF; synthetic MnSiO₃, MnK α , LIF; elemental V, VK α , PET (corrected for overlap of TiK β)

Notes:

1. Total iron as Fe₂O₃
2. Fe²⁺/Fe³⁺ ratios calculated by charge balance
3. Garnet end-member calculations after Rickwood (1968)
4. Pyroxene end-member calculations after Deer et al. (1992)

Patterson and Rowins: Table 5

Table 6. Microthermometric Data

sample	mineralization type	T _e (°C)	mean ± 1σ	wt % NaCl eq. ¹	mean ± 1σ	T _h (°C)	mean ± 1σ
SAC98-3-260.6	Qtz-Apy vein	-38.0 to -39.1 (6)	-38.4 ± 0.4	6.1 to 10.5 (7)	8.1 ± 1.3	278 to 305 (6)	300 ± 11
COL-99-4-316A	Qtz-Apy vein	-26.9 to 32.6 (5)	-30.0 ± 2.6	14.2 to 19.7 (5)	16.7 ± 2.4	336 to 383 (9)	357 ± 13
SAC-98-4-62.2	disseminated	-20.0 to -41.5 (4)	-30.6 ± 9.9	5.5 to 13.8 (4)	7.9 ± 4.0	282 to 386 (18)	360 ± 28
Kp-53	disseminated	-25.6 to -33.4 (18)	-29.1 ± 2.5	3.6 to 4.7 (18)	4.2 ± 0.4	251 to 375 (24)	315 ± 38
Kp-40	disseminated	-28.3 (1)		6.1 (1)		n/a	
SAC-98-3-185.8	disseminated	-24.9 to -38.0 (6)	-29.5 ± 5.1	1.3 to 8.0 (6)	5.1 ± 2.6	285 to 389 (22)	338 ± 32
SAC-98-3-100A	manto	-28.1 to -36.0 (4)	-32.6 ± 3.3	4.3 to 7.3 (5)	6.2 ± 1.2	205 to 306 (24)	269 ± 26
SAC-98-3-209A	manto	-24.0 to -37.1 (10)	-30.0 ± 4.3	5.6 to 8.4 (9)	6.4 ± 0.9	224 to 292 (26)	269 ± 22
ROS-99-102A	manto	-38.0 to -47.0 (4)	-43.8 ± 4.0	5.0 to 7.1 (4)	5.9 ± 0.9	205 to 292 (10)	258 ± 43
SAC-98-3-103A	manto	-19.7 to -33.2 (6)	-28.2 ± 4.9	0.5 to 6.8 (9)	2.9 ± 2.1	216 to 287 (14)	263 ± 18

Abbreviations: Apy = arsenopyrite; Qtz = quartz; mean ± 1σ = mean value ± one standard deviation, T_e = eutectic temperature; T_h = homogenization temperature to liquid; wt % NaCl eq. = weight percent NaCl equivalent

¹ Determined from freezing point depressions using the equations of state of Bodnar and Vityk (1994)

Patterson and Rowins: Table 6

Table 7. Lead Isotope Analyses

Sample	Sample type	Mineral	$^{206}\text{Pb}/^{204}\text{Pb}$	% 1 σ	$^{207}\text{Pb}/^{204}\text{Pb}$	% 1 σ	$^{208}\text{Pb}/^{204}\text{Pb}$	% 1 σ	$^{207}\text{Pb}/^{206}\text{Pb}$	% 1 σ	$^{208}\text{Pb}/^{206}\text{Pb}$	% 1 σ
Kp-34	fracture	Sx	18.945	0.05	15.695	0.05	38.937	0.05	0.828	0.003	2.055	0.005
Kp-50b	fracture	Sx	18.946	0.05	15.688	0.05	38.859	0.05	0.828	0.007	2.051	0.008
Kp-50b	fracture	Sx	18.901	0.14	15.701	0.14	38.896	0.14	0.831	0.020	2.058	0.010
KP-50	fracture	Bn	18.865	0.08	15.696	0.08	38.838	0.09	0.832	0.029	2.059	0.023
COL9901-316.6	Qtz-Apy vein	Apy	18.981	0.01	15.730	0.00	39.012	0.01	0.829	0.011	2.055	0.005
LB9604-425	diss	Bn	18.919	0.05	15.668	0.04	38.961	0.07	0.828	0.021	2.059	0.047
SAC-PAD-4	diss	Bn	18.899	0.01	15.665	0.00	38.842	0.01	0.829	0.007	2.055	0.004
SAC9803-147	diss	Bn	18.893	0.03	15.664	0.02	38.830	0.03	0.829	0.013	2.055	0.017
Kp-38	diss	Sp	18.903	0.08	15.706	0.05	38.997	0.18	0.831	0.055	2.063	0.160
Kp-39	diss	Sp	18.906	0.02	15.661	0.02	38.824	0.02	0.828	0.003	2.054	0.000
Kp-42	manto	Mo	18.914	0.02	15.684	0.02	38.902	0.02	0.829	0.011	2.057	0.007
Kp-44	manto	Gn	18.893	0.01	15.678	0.01	38.871	0.02	0.830	0.011	2.057	0.007
Kp-49	manto	Gn	18.903	0.03	15.687	0.02	38.955	0.04	0.830	0.024	2.061	0.021
SAC98-03-76.3	manto	Sx	18.903	0.02	15.668	0.02	38.833	0.02	0.829	0.004	2.054	0.003
SAC9803-249.7	manto	Bn	18.915	0.02	15.707	0.01	38.977	0.03	0.830	0.016	2.061	0.020
SAC9803-100.7	manto	Apy	18.927	0.04	15.697	0.04	38.875	0.04	0.829	0.010	2.054	0.011
SAC9804-205	manto	Sp	18.874	0.04	15.662	0.03	38.809	0.06	0.830	0.029	2.056	0.047
COL9901-291.2	manto	Po	18.874	0.05	15.643	0.05	38.655	0.05	0.829	0.011	2.048	0.014
Kp-15	Ls	Wr	19.557	0.16	15.775	0.15	39.048	0.17	0.807	0.064	1.997	0.052
Kp-17	Ls	Wr	19.662	0.51	15.783	0.51	39.144	0.51	0.803	0.043	1.991	0.054
Kp-52	shale	Wr	19.122	0.12	15.660	0.09	39.087	0.14	0.819	0.088	2.044	0.066
Kp-01	Intr	Fs	18.913	0.02	15.679	0.01	38.903	0.02	0.829	0.018	2.057	0.010
Kp-07	Intr	Fs	18.847	0.01	15.656	0.01	38.786	0.01	0.831	0.009	2.058	0.004
Kp-09	Intr	Fs	18.934	0.03	15.719	0.03	38.993	0.04	0.830	0.009	2.059	0.021
Kp-12	Intr	Fs	18.877	0.03	15.655	0.02	38.785	0.03	0.829	0.018	2.055	0.006

Notes: analyses by Janet E. Gabites, Geochronology Laboratory, Department of Earth and Ocean Sciences, UBC.
Mineral abbreviations: Gn = galena; Sx = mixed sulphide; Sp = sphalerite; Po = pyrrhotite; Apy = arsenopyrite; Bn = bornite; Mo = molybdenum; Fs = feldspar; Wr = whole rock.
Sample Types: Fracture = fracture-controlled mineralization; Diss = disseminated Cu-Ag mineralization; Manto = polymetallic manto mineralization; Ls = limestone; Intr = intrusive rocks.

Patterson and Rowins: Table 7

Chapter 4

General Conclusions

The development of a detailed structural and fluid evolution model to explain the location of skarn-related Cu (Zn-Pb-Ag-Au) mineralization within regionally and locally developed structures has greatly enhanced understanding of the formation of the Sacrificio deposit. The results of this research show that both pre- and syn-mineralization deformation has strongly controlled the present-day distribution of the known mineralization. Extensive field mapping combined with detailed structural analysis, lithogeochemistry, and U-Pb geochronology have been used to understand the mineralizing process at the Sacrificio deposit. Additionally, the source and physicochemical conditions (P-T-X) of fluids forming calc-silicate skarn and sulphide mineralization have been determined using lead isotope, fluid inclusion, and mineralogical data. The Sacrificio deposit is classified as a copper skarn based on garnet and pyroxene compositions in addition to known metal abundances and dominant styles of mineralization. This study provides one of the most complete descriptions of a large, polymetallic skarn deposit in Mexico.

Three phases of pre-intrusion regional deformation are recognized in rocks at the Sacrificio deposit. D_1 and D_3 record strong east-northeast shortening associated with the Mexican fold-and-thrust belt, whereas D_2 indicates a minor re-orientation of shortening directions to produce rare east-trending folds. Two episodes of intrusion-related deformation post-date regional deformation. D_4 is

the formation of a broad dome above the Sacrificio intrusion and D_5 is the opening of extensional fractures and veins above and peripheral to the intrusion.

Skarn-forming fluids were preferentially channeled along axial surfaces of large amplitude, D_3 folds. This has resulted in the localization of garnet skarn along D_3 fold axial traces. Late mineralizing fluids were focussed mainly by D_5 fractures and precipitated bornite \pm chalcopyrite where they infiltrated porous garnet skarn. Thus, where late-stage, intrusion-related, east-striking fractures (D_5) intersect D_3 fold axial surfaces, disseminated Cu-Ag mineralization is formed. This structural intersection is a critical feature in the localization of skarn mineralization at the Sacrificio deposit.

Uranium-lead isotopic dating of four samples of intrusive rocks from the Sacrificio deposit revealed two temporally distinct intrusive suites. Lithogeochemical analysis of these suites revealed a correlative compositional distinction. The older suite, including Dique Viejo and several smaller dykes at Cerro Coloradito is interpreted to be 109.1 ± 0.4 Ma. The younger suite, which includes the Sacrificio and Coloradito intrusions is interpreted to be 40.1 ± 0.5 Ma. This younger Middle Eocene suite is interpreted to have caused the calc-silicate skarn and related mineralization at the Sacrificio deposit based on a variety of geological evidence.

Fluid inclusion studies of mineralization associated with prograde and retrograde skarn (disseminated Cu-Ag and manto mineralization, respectively) and of post-skarn quartz-arsenopyrite veins demonstrate that mineralizing fluids are predominantly NaCl-H₂O mixtures with additional divalent cations including

Mg²⁺, Fe²⁺, and Ca²⁺. The disseminated Cu-Ag and polymetallic manto mineralization was formed from fluids ranging in salinity from 0.5 to 13.8 wt. % NaCl equivalent, whereas late arsenopyrite veins were formed from fluids with salinities 6.1 to 19.7 wt. % NaCl equivalent. Temperatures of homogenization range from 251° to 389° C in disseminated mineralization, and 205° to 306° C in manto mineralization. Post-skarn quartz-arsenopyrite veins give homogenization temperatures of 278° to 383° C. Pressures during the development of the Sacrificio deposit are estimated at approximately 0.5 to 1.0 kbars based on evidence from stratigraphic reconstructions. Trapping temperatures are obtained by applying pressure corrections (dependant on both pressure and salinity of the fluid) to the measured temperatures of homogenization. Trapping temperatures obtained from fluid inclusion data and temperatures of prograde skarn formation obtained from mineral stability data demonstrate a gradual cooling of the skarn system. Prograde skarn formed at 460° to 580° C, disseminated mineralization at 291° to 504° C, and polymetallic manto mineralization was formed at cooler temperatures of 220° - 390° C. This was then overprinted by a final pulse of hotter fluids (330° - 495° C) which formed the post-skarn quartz-arsenopyrite veins.

Studies of Pb-isotope compositions of mineralization and potential lead 'reservoirs' commonly are used to trace the source of metals in mineral deposits (e.g., Richards et al., 1991; Tosdal et al., 1999). At the Sacrificio deposit, Pb-isotope compositions of sulphide minerals associated with mineralization, intrusive rocks, and sedimentary host-rocks strongly indicate a magmatic source

has contributed the lead, and by inference, other metals that now comprise the mineralization at the Sacrificio deposit.

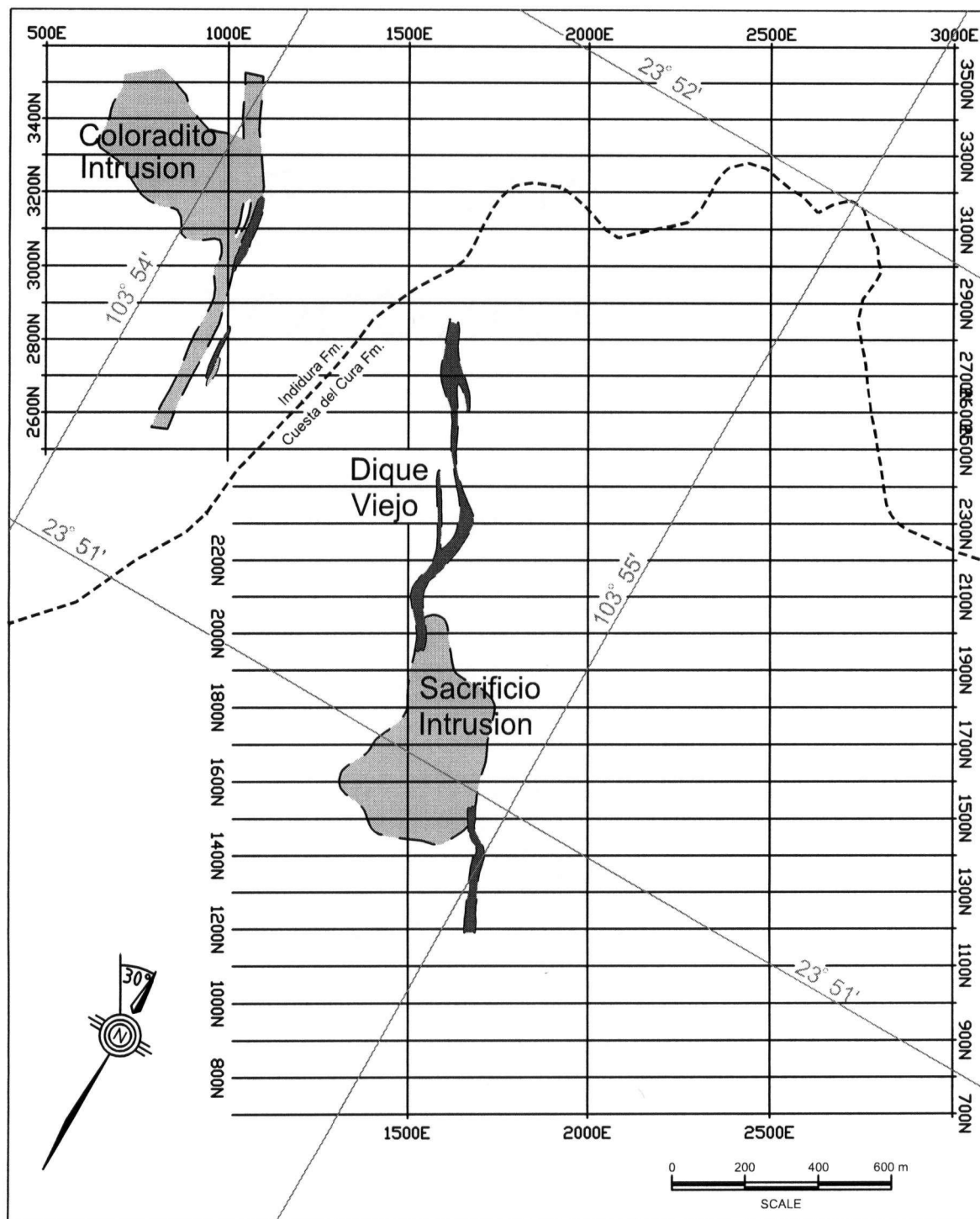
In summary, the results of this study provide constraints on the structures, fluid sources, and physicochemical conditions of skarn formation and related mineralization at the Sacrificio deposit. It has been demonstrated that both pre- and syn-intrusion structures are key elements in the development of the Sacrificio skarn system. The structural model developed at the Sacrificio deposit may be applied to other skarn and carbonate replacement deposits of the Mexican Altiplano and elsewhere in the world.

References

- Richards, J.P., McCulloch, M.T., Chappell, B.W., and Kerrich, R., 1991, Sources of metals in the Porgera gold deposit, Papua New Guinea: Evidence from alteration, isotope and noble gas geochemistry: *Geochimica et Cosmochimica Acta*, v. 55, p. 565-580.
- Tosdal, R. M., Wooden, J. L., and Bouse, R. M., 1999, Pb Isotopes, Ore Deposits, and Metallogenic Terranes: *In* Lambert, D.D. and Ruiz, J., eds., *Application of Radiometric Isotopes to Ore Deposit Research and Exploration*, Society of Economic Geologists, Reviews in Economic Geology, v. 12, p. 1-28.

Appendix A

Location Map of Local Sacrificio Grid and Grid Coordinates



Appendix B

Structural Data - Sacrificio Deposit

Sacrificio Structural Data

Note: all data reported using right-hand-rule

Locations given in grid coordinates as shown in appendix A

Location		bedding		fractures		fold axes		axial planar fracture	
easting	northing	strike	dip	strike	dip	trend	plunge	strike	dip
1020	700	145	65						
1736	713	90	90						
1010	780	144	70						
1628	817	165	75						
2010	820	111	65						
1794	867	185	74						
2030	875	5	45						
1656	923	155	72						
1014	927	144	70						
1752	943	160	71						
1728	944	154	70						
2010	950	145	62						
2030	950			60	83				
1522	982	135	70						
1830	1010	325	68						
1912	1014	115	85						
1595	1015	142	75						
1610	1015	147	75						
1920	1020					286	64		
1370	1025	152	88						
1420	1025	154	83						
1460	1025	155	84						
1502	1026	174	73						
1520	1030					182	69		
1021	1030	160	87						
1850	1080					166	58		
1960	1080	143	90						
1975	1080			249	68				
1990	1090	19	40						
2100	1110	40	43						
1030	1115	165	70						
1200	1120	120	81						
1650	1120			90	90				
1990	1120	184	75						
2190	1120	15	18						
2250	1120	30	72						
1600	1130	160	74						
1915	1130	355	70						
1950	1130	140	57						
1970	1130	2	77						
1658	1132	120	43						
1248	1133	183	72						
2151	1135	176	67						
1468	1139	145	78						
1613	1147	135	77						
1627	1157					138	22		
1568	1216	45	60						
1520	1220	135	60						
1780	1220								
1885	1220	140	44						
1960	1220	135	37						
2215	1220	25	90						
1612	1223	180	90						
1300	1225	155	76						
1490	1225	150	83						
2150	1225			270	82				
2200	1225			285	75				
1944	1227	155	47						
1974	1229	144	59						
1469	1229	115	74						
1180	1230	155	90						
1340	1230			275	65				

Location		bedding		fractures		fold axes		axial planar fracture	
easting	northing	strike	dip	strike	dip	trend	plunge	strike	dip
2070	1230	130	53						
2100	1230	175	80						
2255	1230	15	88						
1415	1231	155	76						
1242	1232			225	90				
1601	1232	160	45						
2234	1234			275	70				
1435	1234	148	77						
1861	1237	130	43						
1027	1237			236	69				
1964	1239			290	58				
1386	1239	178	71						
1368	1240	173	74						
1990	1240	175	81						
1001	1244	140	76						
1768	1245	143	52						
1240	1250			257	75				
2179	1258	130	77						
1983	1260	165	86						
2060	1280					170	40		
2160	1280					95	56		
1985	1285	165	72						
1985	1315	160	72						
1480	1320			255	74				
1590	1320	120	90						
1810	1320			250	70				
1875	1320			252	60				
1950	1320	150	67						
2040	1320	25	77						
1280	1324					148	60		
1497	1324	170	90						
1293	1325	158	69						
1915	1325			258	90				
2320	1325	165	54						
1061	1326	176	57						
1196	1328	130	84						
1230	1330	157	75						
1250	1330			75	75				
1365	1330	130	84						
1990	1330					155	9		
2010	1330			100	77				
2115	1330			277	77				
1021	1330	142	80						
1165	1333	130	80						
1932	1334	165	80						
1205	1335					120	58		
2205	1335	162	66						
2076	1339	155	67						
1640	1340	140	50						
2060	1340			285	75				
2098	1340	170	77						
2180	1340			260	72				
2160	1341	160	53						
1871	1344	165	90						
1263	1348	160	70						
2009	1365	125	36						
2082	1371					170	18		
2129	1374					174	28		
1160	1375					170	57		
2055	1375					140	35		
2188	1376					190	30		
2258	1376					140	25		
2031	1388					190	28		
2233	1389			220	85				
1165	1390			265	76				
2000	1400			265	90				

Location		bedding		fractures		fold axes		axial planar fracture	
easting	northing	strike	dip	strike	dip	trend	plunge	strike	dip
2050	1400	75	30						
2100	1400					190	45		
2300	1400	178	65						
1165	1410	30	66						
1890	1415			237	90				
1915	1415	170	66						
2252	1418	55	26						
1049	1420	152	69						
1185	1420	155	70						
1530	1420	160	90						
1620	1420			16	80				
1672	1420	5	90						
1805	1420	165	70						
1640	1422	165	90						
1036	1423			233	90				
2159	1425	65	30						
1200	1425	145	82						
1220	1425	140	76						
1395	1425	155	90						
1485	1425			254	90				
1505	1425	154	82						
1600	1425			135	90				
1705	1425	25	59						
1734	1425	20	82						
1775	1425	170	72						
1820	1425			265	76				
1835	1425					175	10		
1793	1428					170	15		
1757	1429	180	88						
1305	1430	30	76						
1960	1430	158	72						
1935	1435			255	75				
1010	1438	144	78						
1530	1466			286	74				
1030	1467								
2119	1469					150	35		
1971	1472					196	35		
1996	1472	136	40						
2083	1475					165	28		
1093	1477			265	50				
1070	1477	140	65						
1816	1479	105	30						
2026	1480					132	10		
2169	1481					142	23		
1301	1481	105	70						
1254	1482					168	35		
2143	1484	104	20						
1857	1484	100	50						
2054	1485	205	10						
1350	1485	125	60						
2277	1485					168	35		
1230	1490	150	70						
2207	1491					152	15		
2306	1491			90	90				
1124	1497			65	90				
2000	1500	106	40						
1094	1508			36	85				
1782	1508	118	60						
1724	1514	28	53						
2078	1517			55	80				
1836	1519								
1767	1523					170	30		
2232	1523	90	30						
1265	1525	16	20						
1931	1533	135	40						
1024	1550	150	80						

Location		bedding		fractures		fold axes		axial planar fracture	
easting	northing	strike	dip	strike	dip	trend	plunge	strike	dip
2293	1565					154	22		
1222	1570	130	62						
2005	1570	154	40						
2058	1573	155	48						
2197	1573					165	14		
2324	1574					154	32		
2137	1575					170	20		
2231	1576					144	28		
2077	1578					172	20		
2252	1579					148	30		
2270	1579	75	22						
2373	1580					145	20		
1739	1581	80	40						
2167	1581	105	20						
2540	1592	158	55						
1992	1595			258	78				
1972	1595	120	30						
2200	1600	100	20						
2584	1610			330	90				
1903	1612	45	40						
2613	1615	350	80						
1854	1616	80	35						
1726	1618	18	35						
2182	1620			272	50				
1768	1621	130	50						
2239	1622	85	20						
1958	1625	28	30						
1995	1628	150	22						
2552	1629					355	5		
1305	1641								
1989	1649					178	8		
2025	1650					210	25		
2025	1650			28	50				
2025	1650			75	90				
1936	1657			95	90				
2156	1659					135	20		
1970	1659			198	90				
2051	1662			200	68				
2178	1663	115	20						
2139	1665			260	85				
2016	1672			85	80				
1922	1679	75	20						
2510	1679	140	25						
2496	1679					155	10		
1962	1681	140	28						
2571	1682	134	42						
2223	1684					145	20		
2193	1689	135	50						
2248	1691	90	20						
1575	1706			295	52				
2524	1709	330	75						
2401	1709	10	40						
2461	1710	326	60						
2012	1713					158	15		
1854	1715			70	80				
2079	1716	160	35						
2221	1717			260	75				
1277	1719			220	80				
2122	1719	136	40						
1925	1719			255	75				
1793	1720	75	30						
2050	1720			258	80				
1889	1721	8	35						
2103	1721					148	20		
2341	1722	108	28						
2026	1724					180	15		

Location		bedding		fractures		fold axes		axial planar fracture	
easting	northing	strike	dip	strike	dip	trend	plunge	strike	dip
1836	1725					170	35		
1392	1728	120	45						
1362	1728	155	70						
2174	1730					135	2		
1246	1731	120	65						
1998	1736	140	45						
1158	1740	142	60						
1081	1742	156	50						
1991	1764			100	20				
1302	1765								
2038	1766	120	30						
2121	1766	175	25						
2082	1767	140	20						
2145	1772					158	12		
2400	1774	338	40						
2648	1774	170	70						
2434	1775	148	80						
2511	1775	120	25						
1932	1776					160	20		
2540	1777					145	4		
1326	1779								
2172	1781	98	30						
1208	1781	148	55						
2705	1782	340	80						
2331	1782	60	20						
2622	1783					345	2		
2370	1786					138	12		
2260	1787					162	25		
1164	1787	154	50						
2236	1788	190	25						
1972	1790			260	83				
1248	1790	130	50						
1920	1792			245	90				
2297	1794	126	20						
2480	1797	70	18						
2640	1800			95	85				
2024	1805			228	76				
1837	1807			250	85				
2427	1813					133	15		
1361	1814								
1321	1815								
2356	1823	335	30						
2223	1824					145	17		
2077	1825					180	16		
1970	1829	152	30						
1474	1829	125	60						
1073	1830	135	65						
2201	1835	160	30						
1406	1839	152	55						
1347	1849	153	40						
2617	1852			80	90				
2158	1870					162	20		
1253	1872	170	45						
2653	1874			342	41				
1898	1876					130	6		
2224	1877	110	12						
2173	1878	110	15						
1962	1879	90	20						
2007	1879	156	48						
2112	1880					168	8		
2544	1880	352	40						
2505	1882	320	20						
2047	1882	138	45						
2345	1884					143	10		
2619	1884	162	65						
2313	1886					150	10		

Location		bedding		fractures		fold axes		axial planar fracture	
easting	northing	strike	dip	strike	dip	trend	plunge	strike	dip
2260	1895					146	7		
2701	1896	140	7						
2140	1900					166	5		
2284	1909			60	85				
2367	1909	238	14						
2168	1911			30	90				
1944	1912			246	85				
2574	1913			85	90				
2141	1914			262	70				
2452	1916					156	7		
2052	1918			245	85				
2515	1919			85	90				
2394	1919	85	18						
1866	1920	115	12						
1990	1920			270	75				
1438	1923	152	48						
1966	1924	128	25						
2319	1925	200	15						
1066	1925	145	80						
1296	1925	145	65						
1920	1926					150	12		
1106	1926	140	45						
1214	1926	178	45						
2105	1932	156	15						
2476	1942	185	18						
1835	1960			200	80				
1857	1964			100	35				
2663	1964	175	50						
2012	1967					136	28		
2482	1970					348	5		
2029	1977	100	33						
1826	1977			242	80				
2609	1980	170	35						
2246	1981					160	14		
2542	1981	145	50						
2227	1981	130	15						
2089	1985	135	25						
2343	1986					146	5		
2052	1986			105	90				
1340	1987	158	54						
2191	1987					125	5		
2217	1987			200	85				
2292	1990					166	8		
1816	1995			260	85				
1223	1996					170	9		
1150	2000					152	10		
2125	2000					170	10		
2625	2000					168	24		
2358	2002			105	90				
1843	2005					148	20		
1734	2008	50	20						
1474	2012	154	50						
2714	2012	316	55						
1759	2014	0	40						
1253	2014								
1862	2016	338	20						
1697	2018	140	10						
2474	2019	345	15						
1178	2019	348	75						
2581	2020					350	5		
2423	2021	110	15						
2154	2021	190	20						
1294	2022	155	50						
2644	2022			94	90				
2695	2022	166	28						
1906	2023	124	25						

Location		bedding		fractures		fold axes		axial planar fracture	
easting	northing	strike	dip	strike	dip	trend	plunge	strike	dip
2044	2024					140	2		
1949	2024	145	23						
2183	2026	135	20						
2295	2026			106	90				
2341	2027	154	25						
2665	2027					315	18		
2124	2028	340	30						
2615	2032					314	20		
1258	2035								
2509	2071	148	20						
2008	2071			280	80				
2569	2071	155	40						
2059	2073					152	12		
1751	2074			236	90				
2082	2076	150	30						
2189	2076	158	60						
2805	2078	155	50						
1789	2080			152	90				
2550	2080	190	15						
1936	2081			275	90				
2122	2083	160	55						
2159	2084	145	30						
1093	2085	144	65						
2046	2088			60	90				
2340	2089			100	90				
2180	2089			235	74				
2222	2091					146	4		
1173	2091					158	20		
2276	2093	140	27						
1823	2093	105	32						
1945	2094			270	90				
2372	2095	142	35						
1850	2100	30	20						
2300	2100					350	5		
2350	2100					145	5		
2400	2100	197	20						
2435	2100					320	11		
2600	2100	175	15						
2730	2100	330	65						
2760	2100	348	78						
2850	2100	150	58						
2020	2106	102	10						
2004	2109			320	45				
2803	2116					334	10		
2027	2118	104	10						
1193	2119	22	40						
1735	2119	248	12						
1987	2120			246	90				
2491	2122			80	80				
1926	2122	125	15						
2343	2124					352	2		
1814	2124					175	35		
2711	2127	200	27						
1243	2127	152	50						
1148	2127	147	55						
2661	2128	160	30						
1285	2128	124	53						
2685	2128					320	10		
2181	2130			106	90				
2217	2130					323	2		
2199	2132	130	35						
2280	2132					345	5		
2163	2132					335	2		
1894	2137			240	82				
2001	2138			235	75				
2162	2159					325	2		

Location		bedding		fractures		fold axes		axial planar fracture	
easting	northing	strike	dip	strike	dip	trend	plunge	strike	dip
2112	2167	175	10						
2590	2167	185	25						
2194	2168	165	15						
2378	2168	160	30						
2081	2169	92	25						
2429	2169	142	25						
2326	2169	155	10						
2137	2171					160	3		
1239	2172	160	55						
1933	2172					338	12		
2510	2173			160	75				
1201	2173	153	58						
2687	2173	350	60						
1704	2175					320	2		
1649	2176			138	40				
2011	2177					160	8		
2049	2178					164	25		
2178	2179			68	85				
1665	2179			120	80				
2850	2180	130	35						
1162	2180					150	20		
2476	2181	165	30						
2996	2182	160	65						
2909	2183	162	44						
1106	2185	150	60						
2159	2185	185	20						
2221	2185			80	80				
1635	2187			222	75				
1900	2189	163	26						
2076	2192			80	85				
1476	2195	145	40						
1400	2200	140	42						
2561	2204	340	80						
2534	2205	145	15						
2790	2207	328	45						
1929	2210			244	85				
1968	2211	270	18						
2470	2214			100	90				
1738	2216								
1712	2218	308	15						
2691	2218					346	10		
2388	2219	120	15						
2493	2221	137	35						
2616	2222					326	10		
2356	2222			298	85				
2368	2223					345	10		
1794	2224	134	25						
2287	2224			100	90				
2092	2225			104	90				
1846	2226					313	24		
2211	2227			5	70				
2065	2228					145	18		
2419	2228					336	5		
2247	2231			100	90				
1553	2233	175	60						
2028	2236	148	25						
2138	2241	130	22						
2401	2259	152	23						
2566	2266	153	75						
1975	2269	157	12						
2452	2269	185	15						
2036	2270			175	75				
2356	2271	150	25						
1601	2271	160	10						
2897	2271	240	85						
2315	2272	180	20						

Location		bedding		fractures		fold axes		axial planar fracture	
easting	northing	strike	dip	strike	dip	trend	plunge	strike	dip
2835	2273	345	65						
2527	2274					170	5		
2128	2275	146	30						
1256	2275	155	70						
1497	2278	155	60						
2179	2280			82	80				
1717	2280	95	20						
2951	2281	340	80						
2620	2281	170	55						
1619	2282					162	22		
1859	2283			77	70				
2503	2284	98	5						
2649	2290			55	90				
1991	2291			260	75				
2240	2300			60	90				
2270	2300	184	20						
2231	2303			95	90				
2712	2309	170	60						
2251	2309	347	20						
2873	2310			225	80				
1864	2311	144	20						
2153	2313	325	5						
2301	2314			85	90				
2281	2314					352	6		
1357	2315	108	10						
1752	2315	345	30						
1880	2317					170	20		
2379	2317					316	12		
1782	2318			95	80				
2625	2318					344	10		
1903	2319	140	15						
2185	2320	168	22						
1947	2323	156	20						
1714	2324					328	8		
2482	2324			95	90				
1199	2325	148	58						
2084	2327	167	50						
2009	2328			85	90				
1832	2328	152	26						
1995	2328	162	15						
2106	2329			95	85				
2308	2332	140	12						
2056	2333	100	12						
2011	2339			70	72				
2800	2340			86	90				
2540	2341	145	12						
2042	2346					320	10		
2129	2360	305	12						
2184	2362	135	45						
1813	2366	340	30						
2030	2374	322	45						
1657	2376			275	65				
1843	2376					340	6		
2861	2377	178	50						
2255	2379			85	90				
2447	2379	328	74						
1305	2380	160	65						
1466	2380	165	60						
1950	2381	148	32						
1737	2382	160	20						
2405	2382			100	85				
2353	2382	182	35						
1904	2383	145	35						
2003	2384	160	15						
1559	2384	155	50						
1406	2385	165	30						

Location		bedding		fractures		fold axes		axial planar fracture	
easting	northing	strike	dip	strike	dip	trend	plunge	strike	dip
2694	2386					354	20		
1985	2387			110	60				
2013	2388			30	85				
1246	2390	155	60						
1860	2390			74	73				
2675	2391	178	90						
2000	2400			285	75				
2000	2400			107	65				
1879	2403			240	75				
2094	2405					328	20		
2352	2411			85	90				
1531	2411	135	40						
1761	2411					330	2		
2306	2412					338	15		
1979	2414			66	65				
1955	2415					340	15		
2864	2417	306	58						
1791	2418	152	25						
2031	2419			200	24				
2262	2419	180	25						
2404	2421	325	70						
2327	2421	163	35						
2150	2423	144	35						
2472	2423	155	45						
1881	2424			228	25				
2055	2424					326	15		
2080	2424	334	50						
2210	2428					340	5		
2382	2429	154	40						
1654	2430	154	50						
2099	2433			100	78				
2072	2450			85	80				
2078	2463	305	20						
2276	2465					312	8		
2497	2469					312	25		
2559	2469	285	17						
2334	2469	160	75						
1347	2471	154	75						
2411	2472	168	35						
2598	2474	335	90						
1493	2474	150	48						
1866	2475	154	30						
2351	2475			100	90				
2170	2475	214	12						
2693	2476	180	15						
1310	2479	168	70						
1193	2479	160	75						
1269	2480	165	68						
1427	2481	167	45						
2479	2483	172	25						
2451	2485	178	15						
2569	2490	290	20						
2063	2490					10	12		
1620	2500			118	80				
2030	2500			66	86				
2939	2505	330	30						
2107	2508					340	5		
2339	2510					330	45		
2285	2511					315	22		
2756	2511	324	70						
2375	2512			85	90				
2090	2512	347	20						
2156	2514	180	20						
2201	2517	148	75						
1597	2518	150	30						
2001	2518	320	70						

Location		bedding		fractures		fold axes		axial planar fracture	
easting	northing	strike	dip	strike	dip	trend	plunge	strike	dip
1763	2519	315	12						
1810	2519	275	20						
1913	2519	150	45						
2314	2519	142	40						
2056	2521	300	44						
2474	2521					338	20		
2025	2523					0	10		
2578	2524			45	90				
2711	2525	290	28						
2521	2526					332	6		
1880	2527					8	10		
1453	2528					346	10		
2501	2535	230	10						
2792	2540					340	10		
1980	2550	325	60						
2212	2561					315	25		
1826	2562					305	12		
2295	2563					350	2		
1859	2568	165	25						
880	2571	348	90						
2073	2573	288	20						
1952	2574					350	25		
2268	2574	146	30						
1742	2576	165	40						
748	2576	335	80						
830	2578			275	60				
2220	2579			104	90				
1103	2579	155	72						
2976	2582	174	60						
1705	2584	150	64						
2646	2585	178	12						
2137	2586			102	90				
975	2600	175	85						
1950	2600	165	20						
2350	2600			5	90				
2350	2600			200	85				
2350	2600			276	85				
2450	2600	185	12						
2531	2605	227	20						
2934	2605	185	30						
2403	2607	286	20						
2755	2609	325	55						
2261	2611			90	90				
2018	2612			66	80				
1992	2613	315	55						
1771	2613			90	90				
3004	2613			60	90				
1967	2615	285	30						
1789	2615					325	30		
1880	2616	158	30						
2983	2617					336	10		
2201	2618	142	24						
2216	2619					334	15		
2157	2624	285	30						
2340	2625					334	8		
1857	2626	157	40						
1825	2626	184	30						
2295	2631	315	25						
2332	2632	318	12						
2370	2633	208	10						
2501	2634	184	25						
1681	2635	168	45						
2250	2638							324	90
2008	2646			158	85				
2375	2650			83	85				
1985	2653					183	2		

Location		bedding		fractures		fold axes		axial planar fracture	
easting	northing	strike	dip	strike	dip	trend	plunge	strike	dip
1646	2653			85	90				
2036	2654			90	85				
1779	2656	160	57						
600	2658	164	65						
1703	2659			242	85				
2404	2659			210	90				
2343	2660			275	85				
1905	2661	312	24						
2648	2665	335	30						
2224	2666					335	5		
2016	2666	235	25						
2382	2666							335	90
2036	2667	4	40						
1983	2670	324	30						
2484	2672					158	20		
1772	2673			280	75				
2729	2675	208	26						
2010	2675			135	30				
2690	2676	175	60						
902	2677	175	75						
1127	2680	157	60						
2075	2681	345	25						
2161	2681			100	90				
2518	2683			30	90				
2885	2683	320	40						
2417	2688			85	90				
1941	2700					10	5		
2717	2706			222	80				
1738	2709	173	35						
2649	2713					345	8		
2848	2714	320	70						
2476	2715	130	30						
2697	2715					350	15		
2190	2716	205	25						
2351	2716	166	43						
2223	2717	320	30						
2732	2717					310	25		
1684	2720					186	10		
1666	2721	170	65						
2310	2723	158	70						
2135	2723	184	25						
1443	2723	162	70						
2155	2725					332	25		
2388	2725	332	55						
1082	2727	168	45						
2539	2729	358	65						
844	2729	185	70						
1498	2730	140	75						
2076	2748					350	28		
2061	2762	335	66						
2140	2762	250	15						
2556	2762					320	25		
2035	2764			94	90				
2754	2767	170	60						
2432	2769	316	35						
1195	2770	170	70						
2003	2773					136	20		
1571	2773	170	52						
2270	2773							170	70
2576	2774	308	44						
1619	2775			90	80				
2495	2776	140	20						
934	2776			250	90				
1789	2776	162	30						
2786	2778			134	65				
2531	2779					315	2		

Location		bedding		fractures		fold axes		axial planar fracture	
easting	northing	strike	dip	strike	dip	trend	plunge	strike	dip
756	2780	185	75						
1647	2781	160	43						
994	2782	190	80						
2776	2783			185	75				
2310	2783			265	82				
1967	2784			288	85				
2034	2788			62	60				
2959	2789	235	30						
872	2790	165	70						
2873	2793			90	90				
2804	2795			82	80				
2000	2800			356	85				
2280	2800					345	30		
2540	2801			246	85				
1973	2803			60	90				
2261	2804	280	25						
2070	2806			32	90				
2612	2807	302	47						
1287	2809	178	60						
2499	2809					310	10		
2361	2811	332	58						
2547	2811			284	85				
1947	2812	255	28						
708	2813	2	70						
1668	2813			95	90				
2733	2815	164	50						
2230	2815	298	45						
2704	2816	345	70						
2772	2816	322	50						
2512	2816							338	90
2049	2816	322	65						
2668	2817	160	28						
1156	2819	332	55						
2098	2819	342	48						
1732	2820	172	45						
2148	2821					340	8		
2334	2822	174	40						
1697	2822	170	40						
2192	2823	280	35						
2855	2825	165	70						
2478	2825			320	85				
1091	2827								
2309	2829	210	30						
2032	2830					320	20		
2984	2830					215	4		
2283	2831					315	5		
1995	2835	328	45						
2013	2842			135	38				
2498	2847			220	85				
2464	2852	210	20						
1951	2853			282	85				
2348	2860					324	22		
2254	2869	320	35						
2006	2871			158	90				
2661	2871					320	21		
2513	2876	290	20						
2113	2879	280	15						
2898	2879	320	70						
2604	2880	335	68						
2500	2880							140	65
2500	2880			235	85				
2500	2880			240	90				
2029	2882			94	68				
2479	2883	210	15						
962	2883			164	74				
2732	2885	148	26						

Location		bedding		fractures		fold axes		axial planar fracture	
easting	northing	strike	dip	strike	dip	trend	plunge	strike	dip
2583	2885	175	60						
743	2887	200	90						
2086	2888			350	64				
2436	2888	215	30						
2284	2889	155	52						
2515	2896			95	85				
800	2900	202	60						
1700	2900	167	45						
2315	2900	185	50						
2517	2906					350	10		
2539	2908	326	65						
2633	2908	337	45						
1935	2909	320	24						
2218	2911	325	40						
2856	2911	330	65						
2764	2911	200	30						
950	2913	8	56						
2506	2914							344	90
2240	2914					350	8		
913	2916	185	90						
2449	2918					325	10		
2564	2919	325	60						
2735	2919					330	25		
2008	2920	316	42						
2681	2920	290	35						
722	2920	30	80						
2175	2921	315	30						
2290	2921					340	15		
2653	2921	315	65						
2138	2921	184	25						
2414	2921	195	30						
1132	2925	185	85						
790	2925	185	71						
860	2925								
1050	2925	360	80						
2042	2926	356	45						
2120	2928			320	70				
1168	2929	172	70						
1214	2929	180	82						
1253	2929	165	65						
895	2930					198	17		
2096	2934					50	10		
2020	2940								
2074	2943	300	20						
2000	2950	295	25						
1053	2960			170	90				
2010	2960					340	12		
845	2960	222	70						
872	2973	290	78						
2160	2980	316	33						
2170	2980					350	22		
2195	2980	162	35						
2220	2980	160	59						
2245	2980	160	48						
889	2982	130	65						
824	2984			90	20				
2743	2985	204	45						
2842	2985	170	25						
837	2986			295	74				
2661	2990	235	25						
1727	3000	170	30						
2700	3000	326	65						
2000	3005					320	26		
2886	3009	274	30						
1698	3019					350	10		
2050	3020	395	36						

Location	bedding		fractures	fold axes	axial planar fracture	
	easting	northing	strike	dip	strike	dip
2090	3020	340	40			
2100	3020				325	20
2150	3020	298	72			
2320	3020	163	83			
2450	3020	329	56			
2490	3020	158	62			
1680	3025	172	50			
590	3025	167	90			
680	3025	355	74			
760	3025	167	67			
940	3025	120	90			
1055	3025	324	66			
1110	3025	175	68			
1985	3025	295	20			
2280	3025	155	80			
2768	3028	282	25			
1089	3028	140	90			
1145	3030	165	73			
1165	3030	165	73			
1190	3030	170	72			
1210	3030	170	72			
1225	3030			200	54	
1245	3030	163	64			
1260	3030	185	66			
1320	3030	182	77			
1360	3030	185	76			
1385	3030			294	84	
2813	3031	148	50			
2258	3032	345	25			
1404	3038	176	75			
1956	3061	310	54			
1547	3063					
1615	3068	165	65			
2345	3073	160	70			
1110	3075	172	85			
1130	3075				175	50
1230	3075				175	50
2787	3076	178	50			
2173	3077			44	90	
2148	3078	218	16			
2723	3081	172	30			
2000	3100	325	63			
2270	3100	330	72			
2654	3110				325	22
2666	3111	328	30			
2121	3112				330	20
2086	3113	320	50			
2429	3115	200	30			
2767	3115	315	28			
2736	3116	325	45			
1948	3117	280	25			
633	3121	0	85			
660	3123	105	65			
700	3130	152	75			
960	3130			275	75	
1010	3130			90	90	
1040	3130	5	81			
1090	3130	175	90			
1110	3130			261	78	
1140	3130			267	79	
1185	3130	158	69			
1210	3130	164	60			
1275	3130	152	79			
1300	3130	134	59			
1320	3130	157	68			
1355	3130	164	68			

Location		bedding		fractures		fold axes		axial planar fracture	
easting	northing	strike	dip	strike	dip	trend	plunge	strike	dip
1370	3130	162	75						
1395	3130	165	66						
1430	3130	160	67						
1450	3130	165	70						
1460	3130	147	70						
1485	3130	157	74						
675	3140			65	80				
1405	3142	165	67						
1157	3168								
2761	3169	195	20						
653	3174					158	30		
2260	3175	195	15						
2156	3175	168	45						
2931	3177	165	70						
2513	3179	330	36						
1121	3179	160	90						
1394	3180	152	70						
2590	3181	305	45						
1305	3183	160	74						
2681	3184					188	10		
2805	3186			95	80				
1484	3195	148	75						
650	3200					153	30		
2072	3207	336	40						
2426	3209	340	55						
2961	3211	330	60						
2701	3218	180	45						
1558	3219	158	45						
667	3220	0	40						
622	3221	0	55						
1178	3222	160	80						
2120	3225	320	65						
2786	3227	178	30						
1268	3227	156	80						
1221	3228	145	70						
607	3228					135	50		
2090	3244	330	60						
2538	3270					324	30		
2798	3271	307	20						
2882	3273	145	50						
2620	3275	335	60						
2256	3276					2	20		
1431	3280	147	65						
1555	3288	160	75						
1317	3288	158	70						
1220	3290	155	60						
1397	3291	150	45						
1165	3292	155	45						
2210	3300	330	60						
2561	3305	230	40						
2790	3311			55	90				
2756	3314	352	85						
2792	3321			265	80				
2542	3324			70	65				
2310	3325	300	35						
2512	3327	150	82						
2525	3329					356	22		
2771	3337					350	8		
2819	3356	318	70						
2120	3360	200	25						
2500	3380	200	65						
635	3381	165	90						
1310	3381	150	85						
1549	3381	155	70						
1450	3400	140	65						
1824	3403	170	23						

Location		bedding		fractures		fold axes		axial planar fracture	
easting	northing	strike	dip	strike	dip	trend	plunge	strike	dip
1992	3412	198	60						
2902	3417	184	75						
2720	3418	190	45						
2556	3422	330	60						
2340	3425	320	60						
2410	3425	140	50						
1219	3427	155	90						
2154	3431	325	62						
2660	3432	330	60						
2510	3450	340	20						
2793	3459	155	60						
2815	3470	160	65						
1564	3473	170	22						
692	3479			194	35				
2270	3489	280	40						
1989	3491	178	40						
2369	3492	164	35						
2009	3492								
2287	3495								
2540	3506			45	85				
2976	3507	260	40						
2735	3507	230	45						
2520	3509	160	30						
1627	3509	164	55						
2851	3510	20	35						
2927	3512	310	90						
2798	3513	310	60						
961	3514	352	50						
2239	3515	292	73						
2892	3515	340	60						
1233	3518	153	75						
1006	3520	350	70						
1342	3521	144	70						
2599	3522	165	55						
2024	3523	290	25						
2526	3524			304	80				
2387	3533	275	35						
2580	3538			130	80				
2555	3549			75	70				
2539	3554	175	65						
2403	3561	250	20						
2516	3562	40	45						
2452	3573	200	30						
2022	3578	177	45						

Appendix C

Garnet Compositions - Sacrificio Deposit

Weight Percent Oxides in Garnets as determined by Electron Microprobe Analysis

(Operating conditions and standards used given in Table 2, Paper 2)

Sample	SiO2	TiO2	Al2O3	Cr2O3	Fe2O3	MnO	MgO	CaO	Na2O	Total
40-1	34.7736	0.0070	1.5605	0.0325	28.3538	0.1241	0.1814	33.4106	0.0227	98.4662
40-2	35.3119	0.0002	3.4962	0.0002	25.6616	0.1596	0.1710	33.7407	0.0098	98.5512
40-3	35.2213	0.0002	2.8431	0.0002	26.4915	0.1395	0.0972	33.8671	0.0165	98.6766
40-4	35.8311	0.0951	4.8533	0.0062	24.1092	0.1416	0.0798	34.3312	0.0003	99.4478
40-5	36.0337	0.1025	5.8836	0.0002	22.7514	0.1585	0.0855	34.4521	0.0135	99.4810
40-6	35.3507	0.0002	1.6229	0.0041	28.6781	0.1208	0.0677	33.7117	0.0180	99.5742
40-7	35.7547	0.0002	6.4077	0.0165	22.0731	0.1370	0.0823	34.9413	0.0192	99.4320
40-8	36.0094	0.0005	6.7883	0.0641	21.4541	0.0318	0.0994	34.4349	0.0051	98.8876
40-9	34.8242	0.0002	1.5647	0.0002	28.0072	0.1076	0.1606	33.7521	0.0003	98.4171
40-10	35.3387	0.0043	3.1256	0.0002	26.2422	0.1442	0.1160	33.3756	0.0003	98.3471
40-11	35.5625	0.0851	4.8002	0.0002	24.2110	0.1983	0.0942	34.3776	0.0003	99.3294
40-12	35.8234	0.1036	5.5907	0.0002	22.8374	0.2187	0.0776	34.4899	0.0341	99.1756
40-13	35.1393	0.0002	1.6475	0.0002	28.5461	0.0877	0.0770	34.0407	0.0047	99.5434
40-14	35.7994	0.0582	6.3823	0.0002	21.6648	0.1572	0.1634	34.3898	0.0306	98.6459
40-15	35.9611	0.0411	6.5048	0.0434	21.7990	0.0585	0.0898	34.6848	0.0280	99.2105
40-16	34.9802	0.0100	1.6232	0.0002	27.8950	0.1573	0.2023	33.5650	0.0120	98.4452
40-17	35.1817	0.0002	3.4748	0.0225	25.9209	0.1013	0.1942	34.0347	0.0124	98.9427
40-18	35.7931	0.1660	5.3065	0.0144	23.4932	0.2435	0.0869	34.1370	0.0003	99.2409
40-19	35.1220	0.0006	1.5800	0.0081	28.5442	0.0745	0.0546	34.0402	0.0087	99.4329
40-20	35.8714	0.0002	5.0838	0.0002	24.0547	0.0850	0.0841	34.3762	0.0045	99.5601
40-21	36.1215	0.0412	6.5285	0.0062	22.0315	0.0150	0.0906	34.3286	0.0045	99.1676
40-22	35.1834	0.0002	1.9389	0.0002	27.7060	0.1375	0.1692	33.6548	0.0007	98.7909
40-23	35.2933	0.0039	3.4584	0.0002	25.6142	0.1944	0.1551	34.1460	0.0517	98.9172
40-24	35.7476	0.1970	4.7393	0.0390	24.2665	0.1766	0.1030	34.2450	0.0003	99.5143
40-25	35.9262	0.0631	6.3703	0.0062	22.5011	0.0918	0.0780	35.0370	0.0003	100.0740
40-26	35.9403	0.0473	5.4189	0.0002	23.4996	0.2017	0.0982	34.4877	0.0103	99.7042
40-27	34.8685	0.0054	1.5190	0.0041	28.5293	0.1258	0.2189	33.6596	0.0003	98.9309
40-28	34.9542	0.0020	1.2263	0.0002	28.6885	0.0744	0.1633	33.3682	0.0247	98.5018
40-29	34.7189	0.0074	1.8736	0.0002	27.8998	0.1591	0.1792	33.8346	0.0007	98.6735
40-30	35.5534	0.0002	3.6754	0.0002	25.4084	0.1746	0.1361	33.9143	0.0026	98.8652
40-31	35.7492	0.1138	5.6582	0.0144	23.2008	0.2336	0.0708	34.7138	0.0148	99.7694
40-32	35.8164	0.0156	5.6603	0.0227	22.8419	0.0951	0.1077	34.3257	0.0003	98.8857
40-33	36.0128	0.0056	6.8559	0.0002	21.5055	0.0937	0.0962	35.3054	0.0159	99.8912
40-34	34.8104	0.0061	0.8514	0.0041	29.1569	0.1389	0.3086	33.3493	0.0040	98.6297
40-35	34.5440	0.0002	0.6803	0.0304	28.8100	0.2198	0.3113	33.7246	0.0020	99.3226
40-36	35.0959	0.0002	1.2408	0.0264	28.7309	0.1126	0.1431	33.8901	0.0100	99.2500
40-37	35.2275	0.0178	3.0518	0.0002	26.5546	0.1228	0.1207	34.0120	0.0003	99.1077
40-38	35.7878	0.1569	4.8560	0.0002	24.0107	0.1450	0.1113	34.1417	0.0003	99.2099
40-39	35.9316	0.0439	6.6625	0.0083	21.8489	0.0518	0.0782	35.0899	0.0204	99.7355
41-1	35.7780	0.0287	3.9697	0.0184	25.5596	0.1229	0.0784	33.7728	0.0003	99.3288
41-2	35.0886	0.0002	2.1996	0.0002	27.7823	0.0613	0.0869	33.5076	0.0199	98.7466
41-3	35.1014	0.0347	2.0366	0.0002	27.5004	0.0265	0.1092	33.5912	0.0192	98.4194
41-4	35.6139	0.0449	4.1084	0.0287	24.8647	0.0799	0.0989	34.3335	0.0039	99.1768
41-5	35.9863	0.0256	5.8105	0.0002	23.1474	0.1385	0.0783	34.2362	0.0090	99.4320
41-6	35.0948	0.0068	1.4702	0.0325	28.5275	0.1043	0.1381	33.8822	0.0033	99.2597
41-7	35.6989	0.0333	4.1821	0.0002	24.7996	0.1197	0.0819	34.1342	0.0003	99.0502
41-8	34.7472	0.0125	2.3552	0.0041	27.2086	0.0613	0.1457	33.8981	0.0003	98.4330
41-9	35.4629	0.0002	4.4145	0.0002	24.5899	0.1315	0.0925	34.2881	0.0003	98.9801
41-10	35.5667	0.0082	5.8084	0.0002	22.7431	0.1751	0.0760	34.1503	0.0154	98.5434
41-11	35.0100	0.0044	2.3770	0.0002	27.1903	0.0978	0.1059	33.4901	0.0337	98.3094
41-12	35.1866	0.0367	4.7441	0.0002	24.4509	0.0983	0.0950	34.4078	0.0003	99.0199
41-13	35.0342	0.0462	4.4402	0.0002	25.1997	0.0865	0.0714	34.2705	0.0111	99.1600
41-14	35.9072	0.0002	6.8425	0.0166	21.3095	0.1054	0.0744	34.7351	0.0003	98.9912
41-15	35.3232	0.0033	3.0849	0.0002	26.5694	0.0764	0.0904	33.7860	0.0003	98.9341
41-16	35.8283	0.0764	6.1227	0.0002	22.3213	0.1554	0.0621	34.7632	0.0003	99.3299
41-17	34.9605	0.0115	2.1649	0.0041	27.7815	0.0977	0.1178	33.4987	0.0146	98.6513
41-18	35.2391	0.0002	3.8827	0.0002	25.5096	0.1197	0.0808	34.2896	0.0052	99.1271
41-19	34.2537	0.0002	0.0142	0.0283	29.5339	0.1834	0.1407	33.4177	0.0067	97.5788
41-20	35.9103	0.1449	6.9527	0.0002	21.1755	0.2208	0.0719	34.6678	0.0003	99.1444
41-21	35.0722	0.0002	3.4671	0.0002	26.1594	0.0432	0.0876	34.0502	0.0013	98.8814
41-22	35.6183	0.0002	4.7686	0.0002	23.8783	0.0400	0.0988	34.2017	0.0045	98.6106

Weight Percent Oxides in Garnets as determined by Electron Microprobe Analysis (cont.)

(Operating conditions and standards used given in Table 2, Paper 2)

Sample	SiO2	TiO2	Al2O3	Cr2O3	Fe2O3	MnO	MgO	CaO	Na2O	Total
41-23	36.1473	0.0003	6.8110	0.0002	21.3777	0.1221	0.0546	34.5150	0.0025	99.0307
41-24	35.4546	0.0002	3.6599	0.0205	25.6238	0.1064	0.0897	34.3512	0.0003	99.3066
41-25	35.7442	0.0331	4.6448	0.0002	24.3145	0.1149	0.0561	34.0972	0.0389	99.0439
41-26	35.4872	0.0149	4.3081	0.0002	25.1602	0.0848	0.0772	34.3282	0.0007	99.4625
41-27	34.9349	0.0002	1.7012	0.0305	28.4883	0.0944	0.0737	33.7658	0.0067	99.0957
41-28	35.7597	0.0168	4.9212	0.0002	24.3110	0.1133	0.0619	34.4281	0.0013	99.6135
41-29	34.7471	0.0195	0.7809	0.0385	29.1985	0.0943	0.1469	33.2232	0.0003	98.2492
41-30	35.4701	0.0761	4.3231	0.0471	24.7602	0.1630	0.1002	34.2193	0.0003	99.1594
41-31	34.8219	0.0002	0.1275	0.0081	30.3582	0.1173	0.1163	33.4546	0.0169	99.0210
41-32	35.2567	0.0357	3.7130	0.0002	25.3132	0.1381	0.0778	34.3096	0.0003	98.8446
41-33	35.7666	0.0139	5.0246	0.0103	23.5069	0.2118	0.1243	33.9631	0.0129	98.6344
41-34	34.7882	0.0002	1.4068	0.0002	28.3026	0.1391	0.0790	33.9026	0.0003	98.6190
41-35	35.4262	0.0202	3.8461	0.0002	25.2364	0.0732	0.1459	34.2533	0.0003	99.0018
41-36	35.6906	0.0310	5.3061	0.0002	23.6520	0.1668	0.0840	34.7466	0.0003	99.6776
41-37	35.0043	0.0071	1.1477	0.0325	29.0853	0.0414	0.1402	33.9014	0.0003	99.3602
41-38	35.6505	0.0002	5.5959	0.0002	23.3291	0.2002	0.0930	34.4417	0.0103	99.3211
41-39	34.9669	0.0002	0.4484	0.0002	30.3523	0.0908	0.1187	33.8936	0.0003	99.8714
41-40	35.7406	0.0602	5.3390	0.0021	23.5787	0.1017	0.0814	34.7258	0.0003	99.6298
41-41	35.4877	0.0327	3.3774	0.0002	25.5919	0.0981	0.0868	33.9007	0.0003	98.5758
41-42	34.8633	0.0002	1.4440	0.0183	28.9427	0.1622	0.0630	33.5282	0.0003	99.0222
47-1	36.0176	0.2651	7.5295	0.0002	20.5921	0.1567	0.1319	34.2479	0.0132	98.9542
47-2	35.6986	0.0248	4.7929	0.0265	24.3238	0.1276	0.1018	32.8522	0.0006	97.9488
47-3	35.9263	0.2925	7.1844	0.0002	21.0992	0.1700	0.1384	33.6079	0.0038	98.4227
47-4	36.2708	0.2312	8.8007	0.0002	18.7605	0.1120	0.1080	33.9582	0.0255	98.2671
47-5	35.6246	0.0055	4.0513	0.0002	25.3722	0.1176	0.1038	33.6497	0.0150	98.9399
47-6	35.7449	0.0284	4.1190	0.0002	24.7516	0.2834	0.0502	33.0798	0.0260	98.0835
47-7	36.1674	0.2775	7.1210	0.0186	20.8848	0.1183	0.1389	34.1050	0.0233	98.8548
47-8	36.0327	0.1145	6.8477	0.0144	21.3273	0.1149	0.1025	33.7448	0.0003	98.2991
47-9	36.0216	0.0943	6.0450	0.0002	22.3642	0.0915	0.1197	33.7077	0.0178	98.4620
47-10	36.0458	0.1066	6.2009	0.0226	22.2286	0.1198	0.0940	33.4775	0.0197	98.3155
47-11	36.1996	0.2104	6.8903	0.0002	21.3181	0.1716	0.0900	33.7299	0.0165	98.6266
47-12	36.1726	0.2749	7.4966	0.0392	20.9233	0.0817	0.1127	33.7848	0.0003	98.8861
48-1	35.8353	0.0624	5.3496	0.0348	22.8281	0.1612	0.3190	32.6331	0.0122	97.2357
48-2	35.2822	0.0209	3.4383	0.0002	25.3343	0.1457	0.2668	32.9485	0.0163	97.4532
48-3	36.3397	0.0977	6.4335	0.0021	21.8626	0.1465	0.2171	33.7749	0.0140	98.8881
48-4	35.1391	0.0138	1.4988	0.0002	28.3058	0.0891	0.0838	32.7219	0.0146	97.8671
48-5	34.6729	0.0002	0.8039	0.0002	28.3505	0.1088	0.1628	32.6273	0.0093	96.7359
48-6	35.7562	0.0522	3.4646	0.0082	25.3811	0.0795	0.1050	33.6264	0.0003	98.4735
48-7	35.4360	0.0576	3.0272	0.0061	26.4104	0.1009	0.1211	32.6414	0.0003	97.8010
48-8	35.8686	0.0508	4.5231	0.0002	24.0124	0.1842	0.2842	33.0548	0.0003	97.9786
48-9	35.8795	0.1790	6.1512	0.0288	21.7818	0.1614	0.1777	33.2026	0.0003	97.5623
48-10	34.8965	0.0002	1.5776	0.0243	27.4677	0.0924	0.1549	32.8879	0.0318	97.1333
48-11	35.4925	0.1392	5.7302	0.0205	21.7920	0.1763	0.2523	33.2755	0.0003	96.8788
48-12	35.6279	0.0783	3.9496	0.0102	24.6690	0.1575	0.2157	33.2718	0.0045	97.9845
48-13	35.9195	0.0619	5.9074	0.0002	21.8399	0.1548	0.2446	33.1373	0.0223	97.2879
48-14	35.9113	0.0155	4.8457	0.0470	24.0855	0.1559	0.1415	33.2671	0.0155	98.4850
48-15	35.8167	0.0246	5.5752	0.0021	22.8854	0.1562	0.1611	33.6526	0.0352	98.3091

Mole Percent Cations in Garnet Unit Formula

(calculation based on 8 oxygen atoms)

Sample	Si (T)	Al (T)	Sum_T	Al (VI)	total Al	Fe3 (A)	Ti (A)	Cr (A)	Sum_A	Mg (B)	Mn (B)	Ca (B)	Na (B)	Sum_B
40-1	2.953	0.047	3.000	0.109	0.156	1.812	0.000	0.002	1.924	0.023	0.009	3.040	0.004	3.076
40-2	2.964	0.036	3.000	0.310	0.346	1.621	0.000	0.000	1.931	0.021	0.011	3.035	0.002	3.069
40-3	2.963	0.037	3.000	0.245	0.282	1.677	0.000	0.000	1.922	0.012	0.010	3.053	0.003	3.078
40-4	2.962	0.038	3.000	0.434	0.472	1.500	0.006	0.000	1.940	0.010	0.010	3.040	0.000	3.060
40-5	2.961	0.039	3.000	0.530	0.569	1.407	0.006	0.000	1.943	0.010	0.011	3.033	0.002	3.057
40-6	2.971	0.029	3.000	0.131	0.160	1.813	0.000	0.000	1.945	0.008	0.009	3.035	0.003	3.055
40-7	2.930	0.070	3.000	0.548	0.618	1.361	0.000	0.001	1.910	0.010	0.010	3.067	0.003	3.090
40-8	2.961	0.039	3.000	0.619	0.658	1.328	0.000	0.004	1.951	0.012	0.002	3.034	0.001	3.049
40-9	2.956	0.044	3.000	0.113	0.157	1.789	0.000	0.000	1.902	0.020	0.008	3.070	0.000	3.098
40-10	2.981	0.019	3.000	0.292	0.311	1.666	0.000	0.000	1.958	0.015	0.010	3.017	0.000	3.042
40-11	2.944	0.056	3.000	0.412	0.468	1.508	0.005	0.000	1.925	0.012	0.014	3.049	0.000	3.075
40-12	2.955	0.045	3.000	0.498	0.543	1.417	0.006	0.000	1.922	0.010	0.015	3.048	0.005	3.078
40-13	2.952	0.048	3.000	0.115	0.163	1.805	0.000	0.000	1.919	0.010	0.006	3.064	0.001	3.081
40-14	2.954	0.046	3.000	0.574	0.620	1.345	0.004	0.000	1.923	0.020	0.011	3.041	0.005	3.077
40-15	2.951	0.049	3.000	0.580	0.629	1.346	0.003	0.003	1.931	0.011	0.004	3.049	0.004	3.069
40-16	2.967	0.033	3.000	0.129	0.162	1.781	0.001	0.000	1.911	0.026	0.011	3.051	0.002	3.089
40-17	2.942	0.058	3.000	0.284	0.342	1.631	0.000	0.001	1.917	0.024	0.007	3.050	0.002	3.083
40-18	2.959	0.041	3.000	0.476	0.517	1.462	0.010	0.001	1.948	0.011	0.017	3.024	0.000	3.052
40-19	2.954	0.046	3.000	0.111	0.157	1.807	0.000	0.001	1.918	0.007	0.005	3.068	0.001	3.082
40-20	2.959	0.041	3.000	0.452	0.493	1.493	0.000	0.000	1.945	0.010	0.006	3.038	0.001	3.055
40-21	2.968	0.032	3.000	0.600	0.632	1.362	0.003	0.000	1.965	0.011	0.001	3.022	0.001	3.035
40-22	2.971	0.029	3.000	0.164	0.193	1.760	0.000	0.000	1.924	0.021	0.010	3.045	0.000	3.076
40-23	2.950	0.050	3.000	0.290	0.340	1.611	0.000	0.000	1.901	0.019	0.014	3.057	0.008	3.099
40-24	2.955	0.045	3.000	0.417	0.462	1.510	0.012	0.003	1.941	0.013	0.012	3.033	0.000	3.059
40-25	2.928	0.072	3.000	0.540	0.612	1.380	0.004	0.000	1.924	0.009	0.006	3.060	0.000	3.076
40-26	2.954	0.046	3.000	0.479	0.525	1.454	0.003	0.000	1.935	0.012	0.014	3.037	0.002	3.065
40-27	2.948	0.052	3.000	0.099	0.151	1.815	0.000	0.000	1.915	0.028	0.009	3.049	0.000	3.085
40-28	2.972	0.028	3.000	0.095	0.123	1.835	0.000	0.000	1.930	0.021	0.005	3.040	0.004	3.070
40-29	2.937	0.063	3.000	0.123	0.186	1.776	0.000	0.000	1.900	0.023	0.011	3.066	0.000	3.100
40-30	2.972	0.028	3.000	0.334	0.362	1.598	0.000	0.000	1.933	0.017	0.012	3.038	0.000	3.067
40-31	2.933	0.067	3.000	0.480	0.547	1.433	0.007	0.001	1.921	0.009	0.016	3.052	0.002	3.079
40-32	2.962	0.038	3.000	0.514	0.552	1.422	0.001	0.001	1.938	0.013	0.007	3.042	0.000	3.062
40-33	2.929	0.071	3.000	0.586	0.657	1.316	0.000	0.000	1.903	0.012	0.006	3.077	0.003	3.097
40-34	2.960	0.040	3.000	0.045	0.085	1.866	0.000	0.000	1.912	0.039	0.010	3.038	0.001	3.088
40-35	2.922	0.068	2.989	0.000	0.068	1.897	0.000	0.002	1.899	0.039	0.016	3.056	0.000	3.111
40-36	2.961	0.039	3.000	0.084	0.123	1.824	0.000	0.002	1.909	0.018	0.008	3.063	0.002	3.091
40-37	2.950	0.050	3.000	0.251	0.301	1.673	0.001	0.000	1.925	0.015	0.009	3.051	0.000	3.075
40-38	2.965	0.035	3.000	0.439	0.474	1.497	0.010	0.000	1.945	0.014	0.010	3.031	0.000	3.055
40-39	2.932	0.068	3.000	0.572	0.640	1.341	0.003	0.001	1.916	0.010	0.004	3.067	0.003	3.084
41-1	2.977	0.023	3.000	0.367	0.390	1.601	0.002	0.001	1.970	0.010	0.009	3.011	0.000	3.030
41-2	2.964	0.036	3.000	0.183	0.219	1.766	0.000	0.000	1.949	0.011	0.004	3.033	0.003	3.051
41-3	2.974	0.026	3.000	0.177	0.203	1.753	0.002	0.000	1.932	0.014	0.002	3.049	0.003	3.068
41-4	2.961	0.039	3.000	0.363	0.402	1.556	0.003	0.002	1.923	0.012	0.006	3.058	0.001	3.077
41-5	2.962	0.038	3.000	0.525	0.563	1.434	0.002	0.000	1.960	0.010	0.010	3.019	0.001	3.040
41-6	2.958	0.042	3.000	0.104	0.146	1.809	0.000	0.002	1.915	0.017	0.007	3.059	0.001	3.085
41-7	2.972	0.028	3.000	0.382	0.410	1.553	0.002	0.000	1.937	0.010	0.008	3.044	0.000	3.063
41-8	2.939	0.061	3.000	0.173	0.234	1.732	0.001	0.000	1.906	0.018	0.004	3.071	0.000	3.094
41-9	2.951	0.049	3.000	0.383	0.432	1.540	0.000	0.000	1.923	0.011	0.009	3.057	0.000	3.077
41-10	2.951	0.049	3.000	0.519	0.568	1.420	0.001	0.000	1.940	0.009	0.012	3.036	0.002	3.060
41-11	2.965	0.035	3.000	0.202	0.237	1.733	0.000	0.000	1.935	0.013	0.007	3.039	0.006	3.065
41-12	2.923	0.077	3.000	0.388	0.465	1.529	0.002	0.000	1.918	0.012	0.007	3.063	0.000	3.082
41-13	2.914	0.086	3.000	0.349	0.435	1.577	0.003	0.000	1.929	0.009	0.006	3.054	0.002	3.071
41-14	2.948	0.052	3.000	0.610	0.662	1.317	0.000	0.001	1.928	0.009	0.007	3.056	0.000	3.072
41-15	2.964	0.036	3.000	0.268	0.304	1.677	0.000	0.000	1.946	0.011	0.005	3.037	0.000	3.054
41-16	2.944	0.056	3.000	0.536	0.592	1.380	0.005	0.000	1.921	0.008	0.011	3.060	0.000	3.079
41-17	2.956	0.044	3.000	0.172	0.216	1.768	0.001	0.000	1.941	0.015	0.007	3.035	0.002	3.059
41-18	2.937	0.063	3.000	0.318	0.381	1.600	0.000	0.000	1.918	0.010	0.008	3.062	0.001	3.082
41-19	2.956	0.001	2.958	0.000	0.001	1.918	0.000	0.002	1.920	0.018	0.013	3.090	0.001	3.123
41-20	2.944	0.056	3.000	0.615	0.671	1.306	0.009	0.000	1.931	0.009	0.015	3.045	0.000	3.069
41-21	2.938	0.062	3.000	0.280	0.342	1.649	0.000	0.000	1.929	0.011	0.003	3.056	0.000	3.071
41-22	2.967	0.033	3.000	0.435	0.468	1.497	0.000	0.000	1.932	0.012	0.003	3.053	0.001	3.068

Mole Percent Cations in Garnet Unit Formula (cont.)

(calculation based on 8 oxygen atoms)

Sample	Si (T)	Al (T)	Sum_T	Al (VI)	total Al	Fe3 (A)	Ti (A)	Cr (A)	Sum_A	Mg (B)	Mn (B)	Ca (B)	Na (B)	Sum_B
41-23	2.968	0.032	3.000	0.627	0.659	1.321	0.000	0.000	1.948	0.007	0.008	3.037	0.000	3.052
41-24	2.952	0.048	3.000	0.311	0.359	1.605	0.000	0.001	1.917	0.011	0.008	3.064	0.000	3.083
41-25	2.969	0.031	3.000	0.423	0.454	1.520	0.002	0.000	1.945	0.007	0.008	3.034	0.006	3.055
41-26	2.943	0.057	3.000	0.364	0.421	1.570	0.001	0.000	1.934	0.010	0.006	3.050	0.000	3.066
41-27	2.949	0.051	3.000	0.118	0.169	1.809	0.000	0.002	1.929	0.009	0.007	3.054	0.001	3.071
41-28	2.951	0.049	3.000	0.429	0.478	1.510	0.001	0.000	1.940	0.008	0.008	3.044	0.000	3.060
41-29	2.970	0.030	3.000	0.049	0.079	1.878	0.001	0.003	1.931	0.019	0.007	3.043	0.000	3.069
41-30	2.948	0.052	3.000	0.372	0.424	1.549	0.005	0.003	1.928	0.012	0.011	3.048	0.000	3.072
41-31	2.964	0.013	2.977	0.000	0.013	1.945	0.000	0.001	1.945	0.015	0.008	3.051	0.003	3.077
41-32	2.947	0.053	3.000	0.313	0.366	1.592	0.002	0.000	1.907	0.010	0.010	3.073	0.000	3.093
41-33	2.975	0.025	3.000	0.468	0.493	1.471	0.001	0.001	1.941	0.015	0.015	3.027	0.002	3.059
41-34	2.951	0.049	3.000	0.092	0.141	1.807	0.000	0.000	1.899	0.010	0.010	3.081	0.000	3.101
41-35	2.954	0.046	3.000	0.332	0.378	1.584	0.001	0.000	1.916	0.018	0.005	3.060	0.000	3.084
41-36	2.936	0.064	3.000	0.450	0.514	1.464	0.002	0.000	1.916	0.010	0.012	3.062	0.000	3.084
41-37	2.953	0.047	3.000	0.067	0.114	1.846	0.000	0.002	1.915	0.018	0.003	3.064	0.000	3.085
41-38	2.939	0.061	3.000	0.483	0.544	1.447	0.000	0.000	1.930	0.011	0.014	3.043	0.002	3.070
41-39	2.948	0.045	2.992	0.000	0.045	1.925	0.000	0.000	1.925	0.015	0.006	3.061	0.000	3.083
41-40	2.941	0.059	3.000	0.458	0.517	1.460	0.004	0.000	1.922	0.010	0.007	3.061	0.000	3.078
41-41	2.980	0.020	3.000	0.314	0.334	1.617	0.002	0.000	1.933	0.011	0.007	3.050	0.000	3.067
41-42	2.951	0.049	3.000	0.095	0.144	1.844	0.000	0.001	1.940	0.008	0.012	3.041	0.000	3.060
47-1	2.951	0.049	3.000	0.678	0.727	1.270	0.016	0.000	1.964	0.016	0.011	3.007	0.002	3.036
47-2	3.002	0.000	3.002	0.475	0.475	1.516	0.002	0.002	1.994	0.013	0.009	2.960	0.000	3.004
47-3	2.968	0.032	3.000	0.666	0.698	1.311	0.018	0.000	1.996	0.017	0.012	2.974	0.001	3.004
47-4	2.973	0.027	3.000	0.822	0.849	1.157	0.014	0.000	1.993	0.013	0.008	2.982	0.004	3.007
47-5	2.974	0.026	3.000	0.372	0.398	1.594	0.000	0.000	1.967	0.013	0.008	3.010	0.002	3.033
47-6	3.008	0.000	3.008	0.408	0.408	1.568	0.002	0.000	1.978	0.006	0.020	2.983	0.004	3.014
47-7	2.971	0.029	3.000	0.660	0.689	1.291	0.017	0.001	1.969	0.017	0.008	3.002	0.004	3.031
47-8	2.983	0.017	3.000	0.650	0.667	1.328	0.007	0.001	1.987	0.013	0.008	2.993	0.000	3.013
47-9	2.988	0.012	3.000	0.578	0.590	1.396	0.006	0.000	1.980	0.015	0.006	2.996	0.003	3.020
47-10	2.994	0.006	3.000	0.600	0.606	1.389	0.007	0.001	1.998	0.012	0.008	2.979	0.003	3.002
47-11	2.987	0.013	3.000	0.656	0.669	1.324	0.013	0.000	1.993	0.011	0.012	2.982	0.003	3.007
47-12	2.970	0.030	3.000	0.695	0.725	1.293	0.017	0.003	2.008	0.014	0.006	2.973	0.000	2.992
48-1	3.018	0.000	3.018	0.531	0.531	1.423	0.004	0.002	1.960	0.040	0.011	2.945	0.002	3.022
48-2	2.994	0.006	3.000	0.338	0.344	1.618	0.001	0.000	1.957	0.034	0.010	2.996	0.003	3.043
48-3	2.994	0.006	3.000	0.618	0.624	1.355	0.006	0.000	1.980	0.027	0.010	2.981	0.002	3.020
48-4	3.006	0.000	3.006	0.151	0.151	1.822	0.001	0.000	1.974	0.011	0.006	3.000	0.002	3.019
48-5	3.006	0.000	3.006	0.082	0.082	1.850	0.000	0.000	1.932	0.021	0.008	3.031	0.002	3.062
48-6	3.004	0.000	3.004	0.343	0.343	1.604	0.003	0.001	1.951	0.013	0.006	3.026	0.000	3.045
48-7	3.011	0.000	3.011	0.303	0.303	1.667	0.004	0.000	1.974	0.015	0.007	2.971	0.000	3.015
48-8	3.011	0.000	3.011	0.447	0.447	1.517	0.003	0.000	1.967	0.036	0.013	2.973	0.000	3.022
48-9	3.001	0.000	3.001	0.606	0.606	1.366	0.011	0.002	1.985	0.022	0.011	2.975	0.000	3.014
48-10	3.000	0.000	3.000	0.160	0.160	1.777	0.000	0.002	1.938	0.020	0.007	3.029	0.005	3.061
48-11	2.991	0.009	3.000	0.559	0.568	1.382	0.009	0.001	1.951	0.032	0.013	3.004	0.000	3.049
48-12	3.000	0.000	3.000	0.391	0.391	1.563	0.005	0.001	1.960	0.027	0.011	3.001	0.001	3.040
48-13	3.012	0.000	3.012	0.583	0.583	1.378	0.004	0.000	1.965	0.031	0.011	2.977	0.004	3.022
48-14	2.999	0.001	3.000	0.475	0.476	1.513	0.001	0.003	1.993	0.018	0.011	2.976	0.003	3.007
48-15	2.981	0.019	3.000	0.527	0.546	1.433	0.002	0.000	1.962	0.020	0.011	3.001	0.006	3.038

Garnet Compositions Expressed as Percentage of End-Members

(Method of calculation after Rickwood et al., 1968)

Sample	Almadine	Andradite	Grossular	Pyrope	Spessartine	Uvarovite
40-1	0.00	92.03	6.78	0.78	0.30	0.11
40-2	0.00	82.41	16.48	0.73	0.39	0.00
40-3	0.00	85.61	13.64	0.42	0.34	0.00
40-4	0.00	76.01	23.30	0.33	0.34	0.02
40-5	0.00	71.27	28.01	0.35	0.37	0.00
40-6	0.00	91.84	7.57	0.29	0.29	0.01
40-7	0.00	69.68	29.60	0.34	0.33	0.06
40-8	0.00	67.25	32.06	0.41	0.08	0.21
40-9	0.00	91.95	7.09	0.70	0.27	0.00
40-10	0.00	84.27	14.89	0.49	0.35	0.00
40-11	0.00	76.84	22.29	0.40	0.47	0.00
40-12	0.00	72.28	26.88	0.32	0.52	0.00
40-13	0.00	91.71	7.75	0.33	0.21	0.00
40-14	0.00	68.42	30.52	0.68	0.37	0.00
40-15	0.00	68.42	30.93	0.37	0.14	0.14
40-16	0.00	91.65	7.09	0.88	0.39	0.00
40-17	0.00	83.16	15.70	0.82	0.24	0.08
40-18	0.00	74.09	24.93	0.36	0.58	0.05
40-19	0.00	92.00	7.57	0.23	0.18	0.03
40-20	0.00	75.69	23.76	0.35	0.20	0.00
40-21	0.00	68.84	30.73	0.37	0.04	0.02
40-22	0.00	90.12	8.82	0.73	0.34	0.00
40-23	0.00	82.54	16.33	0.66	0.47	0.00
40-24	0.00	76.62	22.40	0.43	0.42	0.13
40-25	0.00	70.69	28.75	0.32	0.22	0.02
40-26	0.00	73.80	25.32	0.41	0.48	0.00
40-27	0.00	92.35	6.39	0.94	0.31	0.01
40-28	0.00	93.72	5.39	0.71	0.18	0.00
40-29	0.00	90.70	8.14	0.77	0.39	0.00
40-30	0.00	81.53	17.48	0.58	0.42	0.00
40-31	0.00	73.25	25.85	0.30	0.55	0.05
40-32	0.00	71.98	27.27	0.45	0.23	0.08
40-33	0.00	67.40	31.98	0.40	0.22	0.00
40-34	0.00	95.61	2.70	1.34	0.34	0.01
40-35	0.00	97.40	0.61	1.34	0.54	0.10
40-36	0.00	93.58	5.44	0.62	0.28	0.09
40-37	0.00	85.08	14.11	0.51	0.30	0.00
40-38	0.00	75.94	23.25	0.47	0.34	0.00
40-39	0.00	68.63	30.89	0.32	0.12	0.03
41-1	0.00	80.64	18.69	0.33	0.29	0.06
41-2	0.00	89.37	10.11	0.37	0.15	0.00
41-3	0.00	89.60	9.86	0.47	0.07	0.00
41-4	0.00	79.36	19.93	0.42	0.19	0.10
41-5	0.00	72.60	26.75	0.32	0.33	0.00
41-6	0.00	92.43	6.62	0.59	0.25	0.11
41-7	0.00	79.10	20.27	0.35	0.29	0.00
41-8	0.00	88.38	10.83	0.63	0.15	0.01
41-9	0.00	78.27	21.03	0.39	0.31	0.00
41-10	0.00	72.18	27.09	0.32	0.42	0.00
41-11	0.00	87.95	11.36	0.45	0.24	0.00
41-12	0.00	78.43	20.93	0.40	0.24	0.00
41-13	0.00	81.19	18.30	0.30	0.21	0.00
41-14	0.00	66.99	32.40	0.31	0.25	0.06
41-15	0.00	84.90	14.54	0.38	0.18	0.00
41-16	0.00	70.32	29.05	0.26	0.37	0.00
41-17	0.00	89.69	9.55	0.50	0.24	0.01
41-18	0.00	81.71	17.66	0.34	0.29	0.00
41-19	0.00	99.82	0.00	0.08	0.00	0.10
41-20	0.00	66.56	32.62	0.30	0.52	0.00
41-21	0.00	84.19	15.34	0.37	0.10	0.00
41-22	0.00	76.17	23.32	0.42	0.10	0.00

Garnet Compositions Expressed as Percentage of End-Members (cont.)

(Method of calculation after Rickwood et al., 1968)

Sample	Almadine	Andradite	Grossular	Pyrope	Spessartine	Uvarovite
41-23	0.00	66.75	32.74	0.23	0.29	0.00
41-24	0.00	81.66	17.64	0.38	0.25	0.07
41-25	0.00	76.97	22.53	0.24	0.27	0.00
41-26	0.00	80.03	19.45	0.32	0.20	0.00
41-27	0.00	92.04	7.31	0.31	0.23	0.10
41-28	0.00	76.74	22.74	0.26	0.27	0.00
41-29	0.00	95.85	3.15	0.64	0.23	0.13
41-30	0.00	78.79	20.24	0.42	0.39	0.16
41-31	0.00	99.32	0.00	0.50	0.15	0.03
41-32	0.00	81.31	18.02	0.33	0.33	0.00
41-33	0.00	74.89	24.05	0.52	0.51	0.03
41-34	0.00	92.78	6.54	0.34	0.34	0.00
41-35	0.00	80.73	18.48	0.62	0.18	0.00
41-36	0.00	74.80	24.45	0.35	0.40	0.00
41-37	0.00	94.07	5.12	0.60	0.10	0.11
41-38	0.00	73.86	25.27	0.39	0.48	0.00
41-39	0.00	97.98	1.30	0.51	0.22	0.00
41-40	0.00	74.46	24.95	0.34	0.24	0.01
41-41	0.00	82.87	16.52	0.37	0.24	0.00
41-42	0.00	93.70	5.57	0.27	0.39	0.06
47-1	0.00	64.53	34.55	0.55	0.37	0.00
47-2	0.26	76.07	22.85	0.43	0.30	0.09
47-3	0.00	66.29	32.74	0.57	0.40	0.00
47-4	0.00	58.38	40.91	0.44	0.26	0.00
47-5	0.00	80.39	18.90	0.43	0.28	0.00
47-6	0.00	79.32	19.79	0.21	0.68	0.00
47-7	0.00	65.18	33.91	0.57	0.28	0.06
47-8	0.00	66.81	32.45	0.42	0.27	0.05
47-9	0.00	70.25	29.04	0.50	0.22	0.00
47-10	0.00	69.61	29.65	0.39	0.28	0.07
47-11	0.00	66.47	32.76	0.37	0.40	0.00
47-12	0.00	65.29	33.93	0.46	0.19	0.13
48-1	0.00	72.74	25.39	1.37	0.39	0.12
48-2	0.00	82.47	16.03	1.15	0.36	0.00
48-3	0.00	68.44	30.31	0.90	0.34	0.01
48-4	0.00	92.34	7.08	0.36	0.22	0.00
48-5	0.00	95.75	3.25	0.73	0.28	0.00
48-6	0.00	82.36	16.97	0.45	0.19	0.03
48-7	0.00	84.60	14.62	0.52	0.25	0.02
48-8	0.00	77.21	21.13	1.21	0.44	0.00
48-9	0.00	69.19	29.59	0.75	0.39	0.10
48-10	0.00	91.67	7.33	0.68	0.23	0.09
48-11	0.00	70.78	27.64	1.08	0.43	0.07
48-12	0.00	79.92	18.74	0.92	0.38	0.04
48-13	0.00	70.24	28.35	1.04	0.37	0.00
48-14	0.00	75.92	22.97	0.59	0.37	0.16
48-15	0.00	72.37	26.58	0.67	0.37	0.01

Appendix D

Pyroxene Compositions - Sacrificio Deposit

Weight Percent Oxides in Pyroxenes as determined by Electron Microprobe Analysis

(operating conditions and standards used are given in Table 5, Chapter 3)

Sample	SiO2	TiO2	Al2O3	FeO	Cr2O3	MnO	MgO	CaO	Na2O	Total
47-1	53.3016	0.0002	0.0330	5.8241	0.0002	0.6694	14.5958	25.0947	0.0307	99.5497
47-2	53.9416	0.0183	0.0448	4.2246	0.0086	0.6285	15.4422	25.3486	0.0206	99.6778
47-3	53.2785	0.0348	0.0299	5.9481	0.0193	0.7668	14.3404	25.0795	0.0418	99.5391
47-4	53.8792	0.0002	0.0894	4.8629	0.0387	0.3936	15.4633	25.5405	0.0022	100.2700
47-5	53.0738	0.0002	0.0290	5.6330	0.0064	0.6340	14.5848	25.2934	0.0159	99.2705
47-6	53.2419	0.0002	0.0749	5.6808	0.0150	0.4274	14.8838	25.2453	0.0290	99.5983
47-7	53.1100	0.0140	0.1148	5.6811	0.0300	0.3094	14.7748	25.2861	0.0230	99.3432
47-8	53.1918	0.0284	0.1435	6.0449	0.0002	0.3091	14.6491	25.2819	0.0214	99.6703
47-9	53.2378	0.0002	0.0837	5.6403	0.0002	0.4308	14.8220	25.2607	0.0088	99.4845
47-10	53.2762	0.0342	0.0971	5.1759	0.0002	0.3798	15.0117	25.1807	0.0234	99.1792
47-11	52.9620	0.0002	0.0868	5.5415	0.0150	0.3779	14.8502	25.1643	0.0170	99.0149
47-12	53.3055	0.0002	0.0846	5.8434	0.0321	0.4170	14.6527	25.1053	0.0192	99.4600
47-13	52.5911	0.0134	0.1455	7.0029	0.0107	0.3377	13.8889	25.2319	0.0216	99.2437
47-14	53.1103	0.0002	0.1096	6.2578	0.0278	0.3569	14.2530	25.0379	0.0003	99.1538
47-15	53.0219	0.0002	0.0889	5.5859	0.0002	0.4069	14.8477	25.4208	0.0038	99.3763
47-16	53.9362	0.0005	0.0867	3.2063	0.0002	0.5785	16.2640	25.6687	0.0003	99.7414
47-17	53.0591	0.0002	0.0553	5.4111	0.0086	0.6667	14.7512	25.0426	0.0120	99.0068
47-18	52.5692	0.0207	0.0880	9.3443	0.0002	0.6435	12.0537	24.5368	0.0374	99.2938
47-19	54.0330	0.0002	0.1171	2.8147	0.0259	0.2681	16.5580	25.6336	0.0160	99.4666
47-20	53.4598	0.0002	0.0956	5.7251	0.0300	0.3863	14.7820	25.1827	0.0003	99.6620
48-1	54.4284	0.0002	0.0540	2.1520	0.0238	0.5864	17.0562	25.6469	0.0074	99.9553
48-2	54.0797	0.0108	0.0329	2.3680	0.0002	0.5275	16.7565	25.7927	0.0016	99.5699
48-3	54.5098	0.0002	0.0339	2.1714	0.0065	0.5108	17.0480	25.7138	0.0127	100.0071
48-4	54.4142	0.0108	0.0803	3.4484	0.0108	0.6362	16.3681	25.7154	0.0011	100.6853
48-5	54.4812	0.0002	0.1013	2.4916	0.0130	0.5260	16.7994	25.7930	0.0085	100.2142
48-6	54.1275	0.0002	0.1116	3.1201	0.0002	0.6094	16.3066	25.8524	0.0145	100.1425
48-7	54.3025	0.0131	0.2347	2.4949	0.0002	0.5875	16.7186	25.6028	0.0096	99.9639
48-8	54.3966	0.0002	0.0442	2.4008	0.0108	0.5824	16.9619	25.9024	0.0003	100.2996
48-9	53.6743	0.0052	0.5036	3.1608	0.0280	0.5747	16.1029	25.8820	0.0016	99.9331
48-10	54.3735	0.0218	0.0399	2.1383	0.0002	0.3336	17.0311	25.9217	0.0042	99.8643
48-11	52.7880	0.0002	0.0815	8.5351	0.0002	0.5949	12.7015	24.6450	0.0860	99.4324
48-12	54.4167	0.0071	0.0915	2.1820	0.0195	0.6238	16.9810	25.9630	0.0228	100.3074
48-13	54.6066	0.0046	0.0433	2.9122	0.0002	0.6011	16.4945	25.8280	0.0003	100.4908
48-14	54.3180	0.0002	0.0988	2.4622	0.0692	0.5960	16.9170	25.9737	0.0112	100.4463
48-15	55.0449	0.0091	0.0356	1.8406	0.0002	0.4421	17.0903	25.7104	0.0159	100.1891
48-16	54.3153	0.0002	0.0418	2.5848	0.0238	0.6014	16.7873	25.7604	0.0293	100.1443
48-17	54.2512	0.0002	0.0857	2.7148	0.0002	0.7832	16.5644	25.6679	0.0203	100.0879
48-18	54.3215	0.0120	0.0584	2.9963	0.0497	0.5255	16.8177	25.7457	0.0003	100.5271
48-19	54.0442	0.0206	0.1808	3.6344	0.0237	0.7733	16.1137	25.3451	0.0178	100.1536
48-20	54.1896	0.0318	0.0308	2.2522	0.0455	0.6326	16.7701	25.6776	0.0064	99.6366
48-21	54.5451	0.0139	0.0747	2.3852	0.0151	0.6116	16.9172	25.9293	0.0106	100.5027
48-22	54.4254	0.0002	0.0476	2.3261	0.0433	0.5261	16.9299	25.8305	0.0207	100.1498
48-23	54.3381	0.0176	0.1316	2.4471	0.0195	0.6239	16.4059	25.5046	0.0607	99.5490
48-24	52.8571	0.0147	0.0394	7.2949	0.0002	0.7599	13.3633	24.5143	0.0980	98.9418
48-25	54.7162	0.0002	0.0238	2.2566	0.0650	0.5004	16.9945	25.7472	0.0106	100.3145
48-26	52.6171	0.0125	0.0278	8.9695	0.0002	0.6932	12.5154	25.1526	0.0362	100.0245
48-27	52.7581	0.0002	0.0421	7.8549	0.0002	0.7030	13.0359	24.4270	0.0302	98.8516
48-28	52.8864	0.0002	0.0003	8.4046	0.0340	0.6446	12.8282	24.8000	0.0259	99.6242
48-29	52.9502	0.0086	0.0128	7.3998	0.0490	0.6831	13.4660	25.0379	0.0658	99.6732
48-30	53.1058	0.0021	0.0150	7.8601	0.0002	0.7643	13.3655	25.2623	0.0257	100.4010
48-31	53.3489	0.0002	0.0317	6.8287	0.0149	0.7776	13.7453	25.1997	0.0305	99.9775
48-32	52.7684	0.0002	0.0559	8.7819	0.0002	0.6968	12.5076	24.9701	0.0468	99.8279
48-33	53.5984	0.0103	0.0317	6.5246	0.0235	0.6433	13.9856	25.3953	0.0498	100.2625
48-34	53.3330	0.0002	0.0125	6.6144	0.0171	0.6603	14.1097	25.2617	0.0332	100.0421
48-35	53.2492	0.0023	0.0104	7.1058	0.0213	0.6784	13.6068	25.1655	0.0178	99.8575
48-36	52.7177	0.0002	0.0165	7.6250	0.0002	0.7867	13.3818	25.1236	0.0592	99.7109
48-37	53.0710	0.0002	0.0113	8.0275	0.0002	0.7828	13.0769	25.0964	0.0454	100.1117

Mole Percent Cations in Pyroxene Unit Formula

(calculation based on 6 oxygen atoms and 4 cations)

Sample	Si (T)	Al (T)	Fe3 (T)	Al (M1)	Ti (M1)	Fe3 (M1)	Fe2 (M1)	Fe t (M1)	Cr (M1)	Mg (M1)	Mn (M2)	Ca (M2)	Na (M2)
47-1	1.984	0.001	0.015	0.000	0.000	0.019	0.148	0.167	0.000	0.810	0.021	1.001	0.002
47-2	1.992	0.002	0.006	0.000	0.001	0.008	0.117	0.125	0.000	0.850	0.020	1.003	0.001
47-3	1.986	0.001	0.013	0.000	0.001	0.015	0.158	0.173	0.001	0.797	0.024	1.002	0.003
47-4	1.980	0.004	0.016	0.000	0.000	0.019	0.115	0.134	0.001	0.847	0.012	1.006	0.000
47-5	1.980	0.001	0.019	0.000	0.000	0.021	0.136	0.157	0.000	0.811	0.020	1.011	0.001
47-6	1.977	0.003	0.020	0.000	0.000	0.025	0.131	0.156	0.000	0.824	0.013	1.004	0.002
47-7	1.977	0.005	0.018	0.000	0.000	0.023	0.136	0.159	0.001	0.820	0.010	1.009	0.002
47-8	1.976	0.006	0.018	0.000	0.001	0.024	0.146	0.170	0.000	0.811	0.010	1.006	0.002
47-9	1.979	0.004	0.017	0.000	0.000	0.021	0.137	0.158	0.000	0.821	0.014	1.006	0.001
47-10	1.983	0.004	0.013	0.000	0.001	0.017	0.131	0.148	0.000	0.833	0.012	1.004	0.002
47-11	1.977	0.004	0.019	0.000	0.000	0.024	0.130	0.154	0.000	0.826	0.012	1.006	0.001
47-12	1.984	0.004	0.012	0.000	0.000	0.016	0.154	0.170	0.001	0.813	0.013	1.001	0.001
47-13	1.971	0.006	0.022	0.000	0.000	0.029	0.168	0.197	0.000	0.776	0.011	1.013	0.002
47-14	1.988	0.005	0.007	0.000	0.000	0.011	0.177	0.188	0.001	0.795	0.011	1.004	0.000
47-15	1.973	0.004	0.024	0.000	0.000	0.028	0.122	0.150	0.000	0.823	0.013	1.013	0.000
47-16	1.980	0.004	0.016	0.000	0.000	0.020	0.062	0.082	0.000	0.890	0.018	1.010	0.000
47-17	1.982	0.002	0.015	0.000	0.000	0.018	0.135	0.153	0.000	0.822	0.021	1.002	0.001
47-18	1.995	0.004	0.001	0.000	0.001	0.006	0.290	0.296	0.000	0.682	0.021	0.998	0.003
47-19	1.984	0.005	0.011	0.000	0.000	0.017	0.059	0.076	0.001	0.906	0.008	1.008	0.001
47-20	1.985	0.004	0.011	0.000	0.000	0.014	0.153	0.167	0.001	0.818	0.012	1.002	0.000
48-1	1.984	0.002	0.014	0.000	0.000	0.016	0.036	0.052	0.001	0.927	0.018	1.002	0.001
48-2	1.981	0.001	0.017	0.000	0.000	0.018	0.037	0.055	0.000	0.915	0.016	1.013	0.000
48-3	1.986	0.001	0.013	0.000	0.000	0.015	0.039	0.054	0.000	0.926	0.016	1.004	0.001
48-4	1.980	0.003	0.016	0.000	0.000	0.019	0.070	0.089	0.000	0.888	0.020	1.003	0.000
48-5	1.984	0.004	0.012	0.000	0.000	0.016	0.048	0.064	0.000	0.912	0.016	1.006	0.001
48-6	1.979	0.005	0.017	0.000	0.000	0.022	0.057	0.079	0.000	0.889	0.019	1.013	0.001
48-7	1.983	0.010	0.007	0.000	0.000	0.017	0.052	0.069	0.000	0.910	0.018	1.002	0.001
48-8	1.978	0.002	0.020	0.000	0.000	0.022	0.031	0.053	0.000	0.920	0.018	1.009	0.000
48-9	1.967	0.022	0.012	0.000	0.000	0.032	0.053	0.085	0.001	0.880	0.018	1.016	0.000
48-10	1.983	0.002	0.015	0.000	0.001	0.016	0.034	0.050	0.000	0.926	0.010	1.013	0.000
48-11	1.991	0.004	0.005	0.000	0.000	0.015	0.249	0.264	0.000	0.714	0.019	0.996	0.006
48-12	1.977	0.004	0.019	0.000	0.000	0.023	0.024	0.047	0.001	0.920	0.019	1.011	0.002
48-13	1.988	0.002	0.010	0.000	0.000	0.012	0.067	0.079	0.000	0.895	0.019	1.007	0.000
48-14	1.973	0.004	0.023	0.000	0.000	0.026	0.026	0.052	0.002	0.916	0.018	1.011	0.001
48-15	2.000	0.000	0.000	0.002	0.000	0.000	0.056	0.056	0.000	0.926	0.014	1.001	0.001
48-16	1.980	0.002	0.018	0.000	0.000	0.022	0.039	0.061	0.001	0.912	0.019	1.006	0.002
48-17	1.981	0.004	0.015	0.000	0.000	0.020	0.048	0.068	0.000	0.902	0.024	1.004	0.001
48-18	1.975	0.002	0.023	0.000	0.000	0.023	0.045	0.068	0.001	0.911	0.016	1.003	0.000
48-19	1.980	0.008	0.013	0.000	0.001	0.020	0.079	0.099	0.001	0.880	0.024	0.995	0.001
48-20	1.984	0.001	0.014	0.000	0.001	0.013	0.042	0.055	0.001	0.916	0.020	1.007	0.000
48-21	1.980	0.003	0.017	0.000	0.000	0.020	0.036	0.056	0.000	0.915	0.019	1.008	0.001
48-22	1.982	0.002	0.016	0.000	0.000	0.019	0.036	0.055	0.001	0.919	0.016	1.008	0.001
48-23	1.994	0.006	0.000	0.000	0.000	0.009	0.066	0.075	0.001	0.898	0.019	1.003	0.004
48-24	1.994	0.002	0.004	0.000	0.000	0.012	0.213	0.225	0.000	0.752	0.024	0.991	0.007
48-25	1.989	0.001	0.010	0.000	0.000	0.010	0.048	0.058	0.002	0.921	0.015	1.003	0.001
48-26	1.978	0.001	0.021	0.000	0.000	0.024	0.237	0.261	0.000	0.701	0.022	1.013	0.003
48-27	1.998	0.002	0.000	0.000	0.000	0.004	0.244	0.248	0.000	0.736	0.023	0.991	0.002
48-28	1.991	0.000	0.009	0.000	0.000	0.010	0.246	0.256	0.001	0.720	0.021	1.000	0.002
48-29	1.983	0.001	0.016	0.000	0.000	0.020	0.196	0.216	0.001	0.752	0.022	1.005	0.005
48-30	1.978	0.001	0.021	0.000	0.000	0.024	0.200	0.224	0.000	0.742	0.024	1.008	0.002
48-31	1.988	0.001	0.010	0.000	0.000	0.013	0.189	0.202	0.000	0.764	0.025	1.006	0.002
48-32	1.986	0.002	0.011	0.000	0.000	0.017	0.248	0.265	0.000	0.702	0.022	1.007	0.003
48-33	1.988	0.001	0.010	0.000	0.000	0.014	0.178	0.192	0.001	0.773	0.020	1.009	0.004
48-34	1.982	0.001	0.017	0.000	0.000	0.020	0.169	0.189	0.001	0.782	0.021	1.006	0.002
48-35	1.989	0.000	0.010	0.000	0.000	0.011	0.200	0.211	0.001	0.758	0.021	1.007	0.001
48-36	1.975	0.001	0.024	0.000	0.000	0.029	0.186	0.215	0.000	0.747	0.025	1.009	0.004
48-37	1.985	0.000	0.014	0.000	0.000	0.018	0.219	0.237	0.000	0.729	0.025	1.006	0.003

Pyroxene Compositions Expressed as Percentage of End-Members

(method of calculation after Deer et al., 1992; Q, J, WO, EN, and FS as defined by Morimoto, 1989)

Sample	diopside	hedenbergite	johannsenite	Q	J	WO	EN	FS
47-1	81.162	16.733	2.104	1.958	0.004	49.714	40.232	10.054
47-2	85.427	12.563	2.010	1.970	0.003	50.067	42.438	7.494
47-3	80.181	17.404	2.414	1.957	0.006	49.878	39.683	10.439
47-4	85.297	13.494	1.208	1.968	0.000	49.920	42.053	8.027
47-5	82.085	15.891	2.024	1.957	0.002	50.101	40.197	9.702
47-6	82.981	15.710	1.309	1.959	0.004	49.767	40.825	9.407
47-7	82.912	16.077	1.011	1.964	0.003	50.049	40.690	9.261
47-8	81.837	17.154	1.009	1.964	0.003	49.937	40.260	9.802
47-9	82.679	15.911	1.410	1.964	0.001	49.896	40.736	9.369
47-10	83.887	14.904	1.208	1.969	0.003	49.954	41.436	8.610
47-11	83.266	15.524	1.210	1.962	0.002	49.879	40.956	9.166
47-12	81.627	17.068	1.305	1.968	0.003	49.828	40.465	9.707
47-13	78.862	20.020	1.118	1.958	0.003	50.173	38.427	11.400
47-14	79.980	18.913	1.107	1.976	0.000	50.040	39.634	10.326
47-15	83.469	15.213	1.318	1.959	0.001	50.079	40.698	9.223
47-16	89.899	8.283	1.818	1.962	0.000	50.077	44.148	5.775
47-17	82.530	15.361	2.108	1.959	0.002	49.769	40.790	9.441
47-18	68.268	29.630	2.102	1.970	0.006	49.962	34.150	15.887
47-19	91.515	7.677	0.808	1.973	0.002	50.182	45.102	4.716
47-20	82.046	16.750	1.204	1.973	0.000	49.843	40.708	9.449
48-1	92.979	5.216	1.805	1.965	0.001	49.778	46.062	4.160
48-2	92.799	5.578	1.623	1.965	0.000	50.207	45.384	4.410
48-3	92.972	5.422	1.606	1.968	0.002	49.898	46.030	4.073
48-4	89.067	8.927	2.006	1.961	0.000	49.755	44.064	6.181
48-5	91.935	6.452	1.613	1.967	0.001	50.056	45.363	4.581
48-6	90.071	8.004	1.925	1.958	0.002	50.239	44.092	5.669
48-7	91.274	6.921	1.805	1.964	0.001	49.931	45.366	4.704
48-8	92.836	5.348	1.816	1.960	0.000	49.969	45.528	4.503
48-9	89.522	8.647	1.831	1.949	0.000	50.542	43.753	5.705
48-10	93.915	5.071	1.014	1.973	0.001	50.283	45.968	3.749
48-11	71.615	26.479	1.906	1.960	0.013	49.838	35.739	14.423
48-12	93.306	4.767	1.927	1.955	0.003	50.135	45.624	4.241
48-13	90.131	7.956	1.913	1.970	0.000	50.126	44.541	5.334
48-14	92.901	5.274	1.826	1.953	0.002	50.041	45.349	4.610
48-15	92.972	5.622	1.406	1.983	0.002	50.141	46.375	3.483
48-16	91.935	6.149	1.915	1.957	0.004	49.913	45.257	4.830
48-17	90.744	6.841	2.414	1.954	0.003	49.885	44.793	5.322
48-18	91.558	6.834	1.608	1.959	0.000	49.606	45.087	5.307
48-19	87.737	9.870	2.393	1.954	0.003	49.489	43.778	6.733
48-20	92.432	5.550	2.018	1.965	0.001	50.084	45.512	4.404
48-21	92.424	5.657	1.919	1.960	0.001	50.044	45.430	4.526
48-22	92.828	5.556	1.616	1.962	0.003	50.042	45.635	4.323
48-23	90.524	7.560	1.915	1.967	0.009	50.270	44.993	4.737
48-24	75.125	22.478	2.398	1.956	0.014	49.621	37.637	12.742
48-25	92.656	5.835	1.509	1.972	0.001	49.946	45.870	4.184
48-26	71.240	26.524	2.236	1.951	0.005	50.189	34.747	15.063
48-27	73.088	24.628	2.284	1.971	0.004	49.596	36.827	13.577
48-28	72.217	25.677	2.106	1.967	0.004	49.881	35.900	14.220
48-29	75.960	21.818	2.222	1.952	0.010	49.986	37.405	12.609
48-30	74.949	22.626	2.424	1.950	0.004	49.927	36.753	13.319
48-31	77.094	20.383	2.523	1.960	0.004	50.129	38.045	11.826
48-32	70.981	26.795	2.224	1.957	0.007	50.162	34.961	14.877
48-33	78.477	19.492	2.030	1.961	0.007	50.332	38.567	11.101
48-34	78.831	19.052	2.117	1.957	0.005	49.945	38.815	11.240
48-35	76.566	21.313	2.121	1.965	0.003	50.150	37.728	12.122
48-36	75.684	21.783	2.533	1.942	0.009	49.931	37.004	13.064
48-37	73.562	23.915	2.523	1.954	0.007	50.017	36.262	13.721

Note: Q = Ca + Mg + Fe²⁺

J = 2Na

WO = Ca₂Si₂O₆

EN = Mg₂Si₂O₆

FS = Fe₂Si₂O₆

Appendix E

Fluid Inclusion Microthermometric Data – Sacrificio Deposit

SACRIFICIO FLUID INCLUSION DATA

Notes: 1. L:V:S ratios by visual estimation at room temperature (25° C)

2. Freezing data accurate to within plus or minus 0.2° C

3. Heating data accurate to within plus or minus 3.0° C

4. Salinities calculated using the MacFlincor program and the equations of state of Bodnar and Vityk (1995)

5. sx = sulphide minerals; cb = carbonate solid

Sample	Mineralization Style	ratio (L:V:S)	solid	Te (deg C)	Tm (deg C)	salinity (wt % NaCl eq.)	Th (deg C)
SAC98-3-260.6(A)	asp-qz vein	80:20			-5.0	7.82	
SAC98-3-260.6(A)	asp-qz vein	70:30		-38.0	-7.0	10.48	
SAC98-3-260.6(A)	asp-qz vein	80:20		-38.3	-5.2	8.10	303.4
SAC98-3-260.6(A)	asp-qz vein	80:20		-38.3	-5.2	8.10	304.8
SAC98-3-260.6(A)	asp-qz vein	80:20		-38.3	-5.2	8.10	302.9
SAC98-3-260.6(A)	asp-qz vein	80:20		-38.3	-5.2	8.10	302.7
SAC98-3-260.6(A)	asp-qz vein	75:25		-39.1	-3.8	6.08	307.2
SAC98-3-260.6(A)	asp-qz vein						278.1
COL-99-4-316A (D)	asp-qz vein	70:30		-27.6	-10.3	14.26	360.2
COL-99-4-316A (D)	asp-qz vein	80:20:<1	sx?	-32.1	-10.2	14.16	354.2
COL-99-4-316A (D)	asp-qz vein	60:40		-30.6	-14.4	18.12	352.8
COL-99-4-316A (D)	asp-qz vein	75:25:<1	sx?	-26.9	-13.2	17.07	367.1
COL-99-4-316A (D)	asp-qz vein	70:30:<1	sx?	-32.6	-16.4	19.74	335.9
COL-99-4-316A (D)	asp-qz vein						347.2
COL-99-4-316A (D)	asp-qz vein						351.9
COL-99-4-316A (D)	asp-qz vein						363.8
COL-99-4-316A (D)	asp-qz vein						383.4
SAC-98-4-62.2 (A)	disseminated	60:40		-20.0			382.2
SAC-98-4-62.2 (A)	disseminated						377.7
SAC-98-4-62.2 (A)	disseminated				-9.9	13.84	367.8
SAC-98-4-62.2 (A)	disseminated						376.5
SAC-98-4-62.2 (A)	disseminated						367.7
SAC-98-4-62.2 (A)	disseminated						363.6
SAC-98-4-62.2 (A)	disseminated						365.4
SAC-98-4-62.2 (A)	disseminated						373.3
SAC-98-4-62.2 (A)	disseminated						369.3
SAC-98-4-62.2 (A)	disseminated						362.5
SAC-98-4-62.2 (A)	disseminated						375.5
SAC-98-4-62.2 (C)	disseminated	62:35:3	unidentified	-36.0	-3.5	5.62	313.0
SAC-98-4-62.2 (C)	disseminated	70:30		-41.5	-4.1	6.52	313.9
SAC-98-4-62.2 (C)	disseminated	65:35		-24.8	-3.4	5.47	369.9
SAC-98-4-62.2 (C)	disseminated						281.7
SAC-98-4-62.2 (C)	disseminated						363.3
SAC-98-4-62.2 (C)	disseminated						370.5
SAC-98-4-62.2 (C)	disseminated						386.3
KP-SAC-99-53 (E)	disseminated	69:30:1	cb	-27.7	-2.9	4.70	258.8
KP-SAC-99-53 (E)	disseminated	70:30		-26.3	-2.8	4.70	258.2
KP-SAC-99-53 (E)	disseminated	70:30		-33.0	-2.6	3.92	313.7
KP-SAC-99-53 (E)	disseminated	70:30		-33.0	-2.4	4.23	312.1
KP-SAC-99-53 (E)	disseminated	65:30:5	unidentified	-27.0	-2.3	3.76	308.7
KP-SAC-99-53 (E)	disseminated	80:20		-25.6	-2.7	4.39	250.8
KP-SAC-99-53 (E)	disseminated						282.1
KP-SAC-99-53 (E)	disseminated						282.8
KP-SAC-99-53 (E)	disseminated						313.0
KP-SAC-99-53 (E)	disseminated						312.7
KP-SAC-99-53 (E)	disseminated						271.2
KP-SAC-99-53 (E)	disseminated						302.6
KP-SAC-99-53 (E)	disseminated						291.9
KP-SAC-99-53 (E)	disseminated						295.2
KP-SAC-99-53 (E)	disseminated						310.8
KP-SAC-99-53 (F)	disseminated	79:20:1	cb	-27.5	-2.4	3.92	361.6
KP-SAC-99-53 (F)	disseminated	75:25		-25.9	-2.3	3.76	343.3
KP-SAC-99-53 (F)	disseminated	74:25:1	cb?	-26.5	-2.2	3.60	362.6
KP-SAC-99-53 (F)	disseminated	74:25:1	cb?	-27.6	-2.3	3.76	342.7
KP-SAC-99-53 (F)	disseminated	82:15:3	cb	-33.4	-2.5	4.07	
KP-SAC-99-53 (F)	disseminated	68:30:2	cb	-30.0	-2.3	3.76	365.1
KP-SAC-99-53 (F)	disseminated						363.6
KP-SAC-99-53 (F)	disseminated						374.9
KP-SAC-99-53 (F)	disseminated						352.5
KP-SAC-99-53 (F)	disseminated						361.9
KP-SAC-99-53 (A)	disseminated	85:15		-30.4	-2.8	4.55	
KP-SAC-99-53 (A)	disseminated	85:15		-29.6	-2.9	4.70	

SACRIFICIO FLUID INCLUSION DATA (cont.)							
Sample	Mineralization Style	ratio (L:V:S)	solid	Te (deg C)	Tm (deg C)	salinity (wt % NaCl eq.)	Th (deg C)
KP-SAC-99-53 (A)	disseminated	85:15		-29.0	-2.7	4.39	
KP-SAC-99-53 (A)	disseminated	75:25		-30.1	-2.7	4.39	
KP-SAC-99-53 (A)	disseminated	85:15		-31.9	-2.8	4.55	293.8
KP-SAC-99-53 (A)	disseminated	90:10		-30.1	-2.7	4.39	
KP-SAC-99-53 (A)	disseminated						
KP-SAC-99-40 (A)	disseminated	85:15		-28.3	-3.8	6.08	
KP-SAC-99-40 (A)	disseminated						
KP-SAC-99-40 (A)	disseminated						
SAC-98-3-185.8 (A)	disseminated	50:50		-24.9	-3.5	5.62	355.6
SAC-98-3-185.8 (A)	disseminated	65:35		-30.1	-2.4	3.92	306.6
SAC-98-3-185.8 (A)	disseminated	90:10		-27.9	-0.8	1.32	
SAC-98-3-185.8 (A)	disseminated	70:30		-26.8	-2.4	3.92	319.9
SAC-98-3-185.8 (A)	disseminated						330.6
SAC-98-3-185.8 (A)	disseminated						353.1
SAC-98-3-185.8 (A)	disseminated						317.3
SAC-98-3-185.8 (A)	disseminated						299.1
SAC-98-3-185.8 (A)	disseminated						306.5
SAC-98-3-185.8 (A)	disseminated						349.9
SAC-98-3-185.8 (A)	disseminated						306.1
SAC-98-3-185.8 (A)	disseminated						317.0
SAC-98-3-185.8 (A)	disseminated						361.8
SAC-98-3-185.8 (A)	disseminated						286.5
SAC-98-3-185.8 (A)	disseminated						284.7
SAC98-3-185.9(B)	disseminated	90:10		-38.0	-5.1	7.96	
SAC98-3-185.9(B)	disseminated	70:30		-31.6	-5.1	7.96	359.2
SAC98-3-185.9(B)	disseminated	70:30					362.1
SAC98-3-185.9(B)	disseminated						357.0
SAC98-3-185.9(B)	disseminated						356.8
SAC98-3-185.9(B)	disseminated						357.2
SAC98-3-185.9(B)	disseminated						388.5
SAC98-3-185.9(B)	disseminated						387.8
SAC98-3-185.9(B)	disseminated						372.6
SAC-98-3-100A (A)	manto	90:10		-33.4	-4.6	7.25	279.5
SAC-98-3-100A (A)	manto	90:10					291.4
SAC-98-3-100A (A)	manto						262.8
SAC-98-3-100A (A)	manto						257.7
SAC-98-3-100A (A)	manto						267.4
SAC-98-3-100A (A)	manto						274.1
SAC-98-3-100A (A)	manto						279.2
SAC-98-3-100A (A)	manto						305.6
SAC-98-3-209A (B)	manto	60:40		-32.0	-3.8	6.08	277.2
SAC-98-3-209A (B)	manto	85:15		-34.4	-3.9	6.23	
SAC-98-3-209A (B)	manto	85:15		-34.4	-3.7	5.93	
SAC-98-3-209A (B)	manto	75:25		-37.1	-5.4	8.38	283.4
SAC-98-3-209A (B)	manto						280.9
SAC-98-3-209A (B)	manto						282.3
SAC-98-3-209A (B)	manto						288.2
SAC-98-3-209A (B)	manto						276.9
SAC-98-3-209A (B)	manto						283.8
SAC-98-3-209A (B)	manto						288.9
SAC-98-3-209A (B)	manto						291.8
SAC-98-3-100A (B)	manto	90:10		-36.0	-4.0	6.37	273.7
SAC-98-3-100A (B)	manto	80:20		-28.1	-4.6	7.25	290.8
SAC-98-3-100A (B)	manto	85:15					266.7
SAC-98-3-100A (B)	manto	90:10		-33.0	-3.7	5.93	247.0
SAC-98-3-100A (B)	manto	88:10:2	unidentified				212.0
SAC-98-3-100A (B)	manto	85:15			-2.6	4.23	204.6
SAC-98-3-100A (B)	manto	70:30					253.2
SAC-98-3-100A (B)	manto						293.9
SAC-98-3-100A (B)	manto						277.8
SAC-98-3-100A (B)	manto						228.5
SAC-98-3-100A (B)	manto						286.2
SAC-98-3-100A (B)	manto						256.6
SAC-98-3-100A (B)	manto						287.6
SAC-98-3-100A (B)	manto						296.3
SAC-98-3-100A (B)	manto						295.1

SACRIFICIO FLUID INCLUSION DATA (cont.)							
Sample	Mineralization Style	ratio (L:V:S)	solid	Te (deg C)	Tm (deg C)	salinity (wt % NaCl eq.)	Th (deg C)
SAC-98-3-209A (C)	manto	80:20		-26.6	-3.6	5.78	272.1
SAC-98-3-209A (C)	manto	70:30		-28.5	-3.5	5.62	266.1
SAC-98-3-209A (C)	manto	65:35		-28.0	-3.8	6.08	270.5
SAC-98-3-209A (C)	manto	60:40		-29.0	-4.8	7.54	275.4
SAC-98-3-209A (C)	manto	90:10		-26.0			
SAC-98-3-209A (C)	manto	80:20		-24.0	-4.0	6.37	271.8
SAC-98-3-209A (C)	manto						245.2
SAC-98-3-209A (C)	manto						278.0
SAC-98-3-209A (C)	manto						240.5
SAC-98-3-209A (C)	manto						224.2
SAC-98-3-209A (C)	manto						240.9
SAC-98-3-209A (C)	manto						241.4
SAC-98-3-209A (C)	manto						285.3
SAC-98-3-209A (C)	manto						205.8
SAC-98-3-209A (C)	manto						281.6
SAC-98-3-209A (C)	manto						281.3
SAC-98-3-209A (C)	manto						279.0
SAC-98-3-209A (C)	manto						276.1
ROS-99-102A (A)	manto	80:20		-38.0	-3.8	6.08	290.8
ROS-99-102A (A)	manto	75:25		-47.0	-3.1	5.47	292.4
ROS-99-102A (A)	manto	90:10		-46.0	-3.4	5.01	209.6
ROS-99-102A (A)	manto	80:20		-44.0	-4.5	7.11	292.2
ROS-99-102A (A)	manto						205.0
ROS-99-102A (A)	manto						209.4
ROS-99-102A (A)	manto						289.8
ROS-99-102A (A)	manto						288.6
ROS-99-102A (A)	manto						292.2
ROS-99-102A (A)	manto						208.4
SAC-98-3-103A (B)	manto	90:10		-26.8	-3.7	5.93	256.0
SAC-98-3-103A (B)	manto	90:10		-33.2	-4.3	6.82	275.2
SAC-98-3-103A (B)	manto	95:5			-0.7	1.16	
SAC-98-3-103A (B)	manto	90:10		-32.8	-0.3	0.50	
SAC-98-3-103A (B)	manto						267.1
SAC-98-3-103A (B)	manto						276.1
SAC-98-3-103A (B)	manto						215.8
SAC-98-3-103A (B)	manto						254.7
SAC-98-3-103A (B)	manto						263.7
SAC-98-3-103A (B)	manto						271.0
SAC-98-3-103A (B)	manto						273.2
SAC-98-3-103A (B)	manto						234.5
SAC-98-3-103A (A)	manto	95:5		-19.7	-1.4	2.31	
SAC-98-3-103A (A)	manto	95:5			-0.9	1.49	
SAC-98-3-103A (A)	manto	95:5			-1.6	2.63	
SAC-98-3-103A (A)	manto	95:5		-28.4	-1.6	2.63	
SAC-98-3-103A (A)	manto	95:5		-28.4	-1.4	2.31	
SAC-98-3-103A (A)	manto						262.0
SAC-98-3-103A (A)	manto						286.5
SAC-98-3-103A (A)	manto						272.4
SAC-98-3-103A (A)	manto						271.8
Total numbers				11.0	12.0	12.0	15.0
disseminated				29.0	29.00	29.00	64.0
manto				24.0	27.00	27.00	74.0
Total Inclusions				64.0	68.00	68.00	153.00
Minimum				-39.1	-16.4	6.1	278.1
disseminated				-41.5	-9.9	1.3	250.8
manto				-47.0	-5.4	0.5	204.6
Total Inclusions				-47.0	-16.4	0.5	204.6
Maximum				-26.9	-5.0	19.7	383.4
disseminated				-20.0	-0.8	13.8	388.5
manto				-19.7	-0.3	8.4	305.6
Total Inclusions				-19.7	-0.3	19.7	388.5

Note: Te = eutectic temperature
Tm = final ice melting temperature
Th = total homogenization temperature

Appendix F

General Geology, Structure, and Alteration Map – Sacrificio Deposit